REPUBLIC OF TURKEY
YILDIZ TECHNICAL UNIVERSITY
GRADUATE SCHOOL OF NATURAL AND APPLIED SCIENCES

3-D AUTOMATIC SEGMENTATION AND MODELLING OF CARTILAGE COMPARTMENTS IN HIGH-FIELD MAGNETIC RESONANCE IMAGES OF THE KNEE JOINT

CEYDA NUR ÖZTÜRK

PhD. THESIS
DEPARTMENT OF COMPUTER ENGINEERING
PROGRAM OF COMPUTER ENGINEERING

ADVISER
ASSOC. PROF. DR. SONGÜL ALBAYRAK

İSTANBUL, 2016

REPUBLIC OF TURKEY

YILDIZ TECHNICAL UNIVERSITY

GRADUATE SCHOOL OF NATURAL AND APPLIED SCIENCES

3-D AUTOMATIC SEGMENTATION AND MODELLING OF CARTILAGE COMPARTMENTS IN HIGH-FIELD MAGNETIC RESONANCE IMAGES OF THE KNEE JOINT

A thesis submitted by Ceyda Nur ÖZTÜRK in partial fulfillment of the requirements for the degree of **DOCTOR OF PHILOSOPHY** is approved by the committee on 19.09.2016 in Department of Computer Engineering, Computer Engineering Program.

Thesis Adviser

Assoc. Prof. Dr. Songül ALBAYRAK

Yıldız Technical University

Approved By the Examining Committee

Assoc. Prof. Dr. Songül ALBAYRAK

Yıldız Technical University

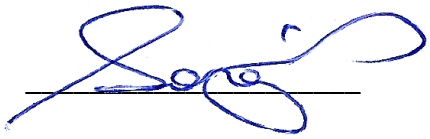

Assoc. Prof. Dr. Mine Elif KARSLIGİL

Yıldız Technical University

Assoc. Prof. Dr. Mustafa KAMAŞAK

İstanbul Technical University

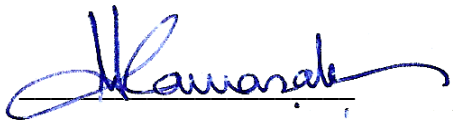

Prof. Dr. Nizamettin AYDIN

Yıldız Technical University

Prof. Dr. Çiğdem EROĞLU ERDEM

Marmara University

ACKNOWLEDGEMENTS

I sincerely thank my adviser Assoc. Prof. Dr. Songül ALBAYRAK for her contributions to and great support for our research. She has considerably been sympathetic towards and patient with me. Her motivations added to my strength to cross the every single threshold in this period.

I am also grateful to Assoc. Prof. Dr. Mustafa KAMAŞAK and Assoc. Prof. Dr. Elif KARSLIGİL on the thesis supervising committee because of their suggestions and comments, which were critical for us to direct our studies; the jury members Prof. Dr. Çiğdem EROĞLU ERDEM for sparing her valuable time to review my thesis in detail and Prof. Dr. Nizamettin AYDIN for his positive opinions to bring the course of our research to a different dimension.

Furthermore, the doctors in Radiology Department of Haseki Hospital aided in answering the questions in our minds on the medical side. Without the data sets the Osteoarthritis Initiative Coordinating Center at the University of California provided, the implementations would not be feasible. I acknowledge the grant awarded under BİDEB 2211 National Graduate Scholarship Programme of TÜBİTAK.

The last but not least, I am deeply indebted to my family, relatives, and friends, who did never left me alone with their guidance and prayers in the background. The words are inadequate to make one last sentence for some of them not among us today.

November, 2016

Ceyda Nur ÖZTÜRK

TABLE OF CONTENTS

Page

LIST OF SYMBOLS

$\mathbf{A}$	the set of voxels in automatic segmentation of an object
$\mathbf{B}$	the set of voxels in reference segmentation of an object
$\mathbf{A}^b$	the set of boundary voxels in $\mathbf{A}$
$\mathbf{B}^b$	the set of boundary voxels in $\mathbf{B}$
$N_{\mathbf{A}}{}^b$	the number of boundary voxels in $\mathbf{A}^b$
$N_{\mathbf{B}}{}^b$	the number of boundary voxels in $\mathbf{B}^b$
$d_i^{\boldsymbol{AB}}$	minimal distance between a voxel in $\mathbf{A}^b$ and the voxel set $\mathbf{B}^b$
$d_j^{\boldsymbol{BA}}$	minimal distance between a voxel in $\mathbf{B}^b$ and the voxel set $\mathbf{A}^b$
r	Pearson's correlation coefficient (PCC)
w_0	Larmor frequency
B_0	external magnetic field
γ	a constant of gyro-magnetic ratio
$\boldsymbol{I}$	an MR image
σ_i	a scale of the physical world in mm especially used for computation of $\boldsymbol{G}^{\sigma_i}$
$\boldsymbol{c}$	coordinate vector of a voxel in $\boldsymbol{I}$
c_y	y coordinate of a voxel
c_z	z coordinate of a voxel
c_x	x coordinate of a voxel
$\boldsymbol{I}$	a volumetric image
$\boldsymbol{I}^{\sigma_i}$	Gaussian smoothed MR image $\boldsymbol{I}$ at scale σ_i
$\boldsymbol{I}_x^{\sigma_i}$	first-order derivative of MR image $\boldsymbol{I}$ at scale σ_i along x axis
$\boldsymbol{I}_y^{\sigma_i}$	first-order derivative of MR image $\boldsymbol{I}$ at scale σ_i along y axis
$\boldsymbol{I}_z^{\sigma_i}$	first-order derivative of MR image $\boldsymbol{I}$ at scale σ_i along z axis
$\boldsymbol{I}_{xx}^{\sigma_i}$	second-order derivative of MR image $\boldsymbol{I}$ at scale σ_i along x axis
$\boldsymbol{I}_{xy}^{\sigma_i}$	second-order derivative of MR image $\boldsymbol{I}$ at scale σ_i along x and y axes
$\boldsymbol{I}_{xz}^{\sigma_i}$	second-order derivative of MR image $\boldsymbol{I}$ at scale σ_i along x and z axes
$\boldsymbol{I}_{yy}^{\sigma_i}$	second-order derivative of MR image $\boldsymbol{I}$ at scale σ_i along y axis
$\boldsymbol{I}_{yz}^{\sigma_i}$	second-order derivative of MR image $\boldsymbol{I}$ at scale σ_i along y and z axes
$\boldsymbol{I}_{zz}^{\sigma_i}$	second-order derivative of MR image $\boldsymbol{I}$ at scale σ_i along z axis
$\boldsymbol{I}_{xxx}^{\sigma_i}$	third-order derivative of MR image $\boldsymbol{I}$ at scale σ_i along x axis
$\boldsymbol{I}_{yyy}^{\sigma_i}$	third-order derivative of MR image $\boldsymbol{I}$ at scale σ_i along y axis
$\boldsymbol{I}_{zzz}^{\sigma_i}$	third-order derivative of MR image $\boldsymbol{I}$ at scale σ_i along z axis
$\boldsymbol{H}^{\sigma_i}$	Hessian matrix based on second-order derivatives of $\boldsymbol{I}$ at scale σ_i
$\boldsymbol{ST}^{\sigma_o,\sigma_i}$	structure tensor matrix based on first-order derivatives of $\boldsymbol{I}$ at scale σ_i

σ_z	digital standard deviation of a filter along z axis
σ_y	digital standard deviation of a filter along y axis
σ_x	digital standard deviation of a filter along x axis
r_z	spatial resolution of $\boldsymbol{I}$ along z axis in mm
r_y	spatial resolution of $\boldsymbol{I}$ along y axis in mm
r_x	spatial resolution of $\boldsymbol{I}$ along x axis in mm
$\boldsymbol{G}^{\sigma_i}$	multi-variate Gaussian filter computed with respect to σ_i
$\boldsymbol{G}^{\sigma_o}$	multi-variate Gaussian filter computed with respect to σ_o
$\boldsymbol{\Sigma}$	covariance matrix of elements in a multi-variate Gaussian filter
$\boldsymbol{\mu}$	mean value vector of elements in a multi-variate Gaussian filter
$\boldsymbol{v}$	coordinate vector of a filter or window element
v_z	z coordinate of a filter element
v_y	y coordinate of a filter element
v_x	x coordinate of a filter element
σ_o	a scale of the physical world in mm especially used for computation of $\boldsymbol{G}^{\sigma_o}$
t_c	threshold for classification of a voxel in the cartilage class
n	number of samples in a training data set
d	number of dimensions of the samples in a training data set
ϵ	relative error bound from the exact k neighbours of a voxel
k	number of nearest neighbours of a voxel
$c_{d,\epsilon}$	a constant that depends on d and ϵ in approximate k-NN algorithm
s_z	size of a filter or window in z axis
s_y	size of a filter or window in y axis
s_x	size of a filter or window in x axis
s_σ	size of a window in scale dimension
C^{σ_i}	cornerness image at scale σ_i
$\boldsymbol{W}$	a multi-rectangular window
$\boldsymbol{M}$	auto-correlation matrix
$\boldsymbol{M^c}$	$3x3$ auto-correlation matrix comprised for a coordinate $\boldsymbol{c}$
$\boldsymbol{k_H}$	a constant coefficient k_H used for measurement of cornerness value
$t_H^{\sigma_i}$	threshold over cornerness values to determine strong corners
$\boldsymbol{r}_C$	narrowing ratio of the range of cornerness values
σ_w	scale of the elements in a window $\boldsymbol{W}$
t_d	threshold over cornerness value differences to select locally maximal corners
t	identifier of a target atlas
r	identifier of the reference atlas
$\boldsymbol{V}_t$	volume of a target atlas
$\boldsymbol{V}_r$	volume of the reference atlas
$\boldsymbol{F}_t$	faces of the mesh that represents the surface of $\boldsymbol{V}_t$
$\boldsymbol{F}_r$	faces of the mesh that represents the surface of $\boldsymbol{V}_r$
$\boldsymbol{P}_t$	points set of the mesh that represents the surface of $\boldsymbol{V}_t$
$\boldsymbol{P}_r$	points set of the mesh that represents the surface of $\boldsymbol{V}_r$
$\boldsymbol{P}_{t_L}$	points set of the mesh that represents the surface of $\boldsymbol{V}_t$ at fine scale
$\boldsymbol{P}_{r_L}$	points set of the mesh that represents the surface of $\boldsymbol{V}_r$ at fine scale
$\boldsymbol{P}_{t'}$	registered points set of $\boldsymbol{P}_t$ to $\boldsymbol{P}_r$
$\boldsymbol{P}_{r'}$	registered points set of $\boldsymbol{P}_r$ to $\boldsymbol{P}_t$
N_A	number of atlases for a compartment of interest

N_t	number of points in $\boldsymbol{P}_t$
N_r	number of points in $\boldsymbol{P}_r$
$\boldsymbol{P}_y$	set of reference shape points that are correspondents of those in $\boldsymbol{P}_t$
$\boldsymbol{p}_t^j$	a point in $\boldsymbol{P}_t$
$\boldsymbol{p}_r^k$	a point in $\boldsymbol{P}_r$
$\boldsymbol{p}_y^j$	a point in $\boldsymbol{P}_r$ as correspondent of the point $\boldsymbol{p}_t^j$
$\boldsymbol{E}$	total error between the points in $\boldsymbol{P_y}$ and the transformed points in $\boldsymbol{P}_t$
e_j	error between the point $\boldsymbol{p}_y^j$ and the transformed $\boldsymbol{p}_t^j$
$\boldsymbol{t}$	optimal translation vector to align $\boldsymbol{P}_t$ to $\boldsymbol{P}_y$
$\boldsymbol{t}'$	optimal translation vector to align centred points in $\boldsymbol{P}_t$ to centred points in $\boldsymbol{P}_y$
s	optimal scale to align $\boldsymbol{P}_t$ to $\boldsymbol{P}_y$
$\boldsymbol{R}$	optimal rotation matrix to align $\boldsymbol{P}_t$ to $\boldsymbol{P}_y$
$\boldsymbol{\mu}_t$	mean coordinate of the points in $\boldsymbol{P}_t$
s_t	mean length of the points in $\boldsymbol{P}_t$
$\boldsymbol{\mu}_y$	mean coordinate of the points in $\boldsymbol{P}_y$
$\boldsymbol{p'}_t^j$	a centred point in $\boldsymbol{P}_t$ by $\boldsymbol{\mu}_t$
$\boldsymbol{p'}_y^j$	a centred point in $\boldsymbol{P_y}$ by $\boldsymbol{\mu}_y$
θ	angle between the centred points in $\boldsymbol{P}_y$ and rotated centred points in $\boldsymbol{P}_t$
$\overline{\boldsymbol{P'}}_t^j$	skew-symmetric matrix based on pure imaginary quaternion of $\boldsymbol{p'}_t^j$
$\boldsymbol{P'}_y^j$	skew-symmetric matrix based on pure imaginary quaternion of $\boldsymbol{p'}_y^j$
$p'_t^{j_x}$	x coordinate of $\boldsymbol{p'}_t^j$
$p'_y^{j_y}$	y coordinate of $\boldsymbol{p'}_y^j$
$\boldsymbol{f}_n$	logarithm of the point difference norms
$\boldsymbol{f}_a$	normalized angle between z-y coordinates of the point differences
$\boldsymbol{f}_x$	unit x direction of the point differences
$\boldsymbol{q}$	a quaternion as a complex number or a vector (may represent $\boldsymbol{R}$)
$\boldsymbol{Q}$	an orthogonal $4x4$ matrix that represents quaternion $\boldsymbol{q}$
$\overline{\boldsymbol{Q}}$	$\boldsymbol{Q}$ with its $3x3$ lower left portion is transposed
$\boldsymbol{q}'$	rotated quaternion $\boldsymbol{q}$

LIST OF ABBREVIATIONS

3-D	3-Dimensional
AAM	Active Appearance Models
AC	Articular Cartilage
APA	After Position Alignment
ASSD	Average Symmetric Surface Distance
BCI	Bone-Cartilage Interface
BPA	Before Position Alignment
CCBR	Center for Clinical and Basic Research
CPD	Coherent Point Drift
CPU	Central Processing Unit
DESS	Double Echo in the Steady State
FB	Femoral Bone
FC	Femoral Cartilage
FLASH	Fast low-angle shot
FS	Fat-Suppressed
GHz	Giga Hertz
GRE	Gradient Echo
IW	Intermediate-Weighted
JSN	Joint Space Narrowing
kg	kilogram
KLG	Kellgren Lawrence Grade
LFC	Lateral Femoral Cartilage
LM	Lateral Meniscus
LOOCV	Leave One Out Cross Validation
LTC	Lateral Tibial Cartilage
MDL	Minimum Description Length
MFC	Medial Femoral Cartilage
m	meter
min	Minute
ml	Millilitre
MM	Medial Meniscus
mm	Millimetre
MR	Magnetic Resonance
MRF	Markov Random Field
MRI	Magnetic Resonance Imaging
MSSD	Maximum Symmetric Surface Distance

MSER	Maximally Stable Extremal Regions
MTC	Medial Tibial Cartilage
NCC	Normalized Cross Correlation
OA	Osteoarthritis
OAI	Osteoarthritis Initiative
PB	Patellar Bone
PC	Patellar Cartilage
PCC	Pearson's correlation coefficient
PLS	Pfizer Longitudinal Study
RAM	Random Access Memory
RF	Radio Frequency
ROI	Region of Interest
s	Second
SE	Spin-Echo
SIFT	Scale Invariant Feature Transform
SKI10	Segmentation of Knee Images 2010
SNR	Signal to Noise Ratio
SPGR	Spoiled Gradient Echo
SSM	Statistical Shape Models
SVM	Support Vector Machine
T	Tesla
TB	Tibial Bone
TC	Tibial Cartilage
VC	Vicinity-Correlated
VD	Volume Difference
VOE	Volume Overlap Error
VOI	Volume of Interest
WE	Water-Excitation

LIST OF FIGURES

Page

LIST OF TABLES

Page

ABSTRACT

3-D AUTOMATIC SEGMENTATION AND MODELLING OF CARTILAGE COMPARTMENTS IN HIGH-FIELD MAGNETIC RESONANCE IMAGES OF THE KNEE JOINT

Ceyda Nur ÖZTÜRK

Department of Computer Engineering

PhD. Thesis

Adviser: Assoc. Prof. Dr. Songül ALBAYRAK

Magnetic resonance (MR) images enable morphological and quantitative assessment of cartilaginous anatomic structures through their manual or automatic segmentations. Because structural changes in the joint compartments, especially deterioration of cartilaginous tissues, indicate strong correlation with a disorder so-named as osteoarthritis, quantification and visualization of the cartilage can establish evidence or progression of this disorder as well as effectiveness of therapeutic or surgical practices. In this thesis, fully-automatic segmentation and modelling of the whole femoral cartilage (FC), tibial cartilage (TC), and patellar cartilage (PC) compartments in MR images of the knee joint was mainly aimed avoiding segmentation methods specialized for the anatomical structures of interest and considering systems with limited resources in particular. The secondary purpose of the thesis was to investigate if detection of the image features such as edges or interest points directly in three-dimensional (3-D) volumes, rather than in two-dimensional (2-D) slices as usual, brings about some advantages or not for volumetric images.

In the first study presented in this thesis, all cartilaginous compartments in the knee joint were automatically segmented in high-field MR images obtained from Osteoarthritis Initiative using a voxel-classification-driven region-growing algorithm with sample-expand method. Computational complexity of the classification was

alleviated via subsampling of the background voxels in the training MR images and selecting a small subset of significant features by taking into consideration systems with limited memory and processing power. Different subsampling techniques, which involve uniform, Gaussian, vicinity-correlated (VC) sparse, and VC dense subsampling, were used to generate four training models. The segmentation system was experimented using 10 training and 23 testing MR images, and the effects of different training models on segmentation accuracies were investigated. Experimental results showed that the highest mean Dice similarity coefficient (DSC) values for all compartments were obtained when the training models of novel VC sparse subsampling technique were used. Mean DSC values optimized with this technique were 82.6%, 83.1%, and 72.6% for FC, TC, and PC, respectively. This study did not require finding a volume of interest, segmenting a bone, or determining bone-cartilage interface prior to segmentation of a cartilage compartment unlike most of the related studies in the literature. Therefore, computational complexity of such a prior operation was reduced in the system. Also, despite processing MR images with single modality for only osteoarthritic participants, the system obtained accuracies similar to those of the related works. About 30-min processing time was promising for segmenting all compartments in all slices of an MR image on a resource-limited platform.

Moreover, a novel hybrid segmentation method was proposed to primarily deal with the oversegmentation problems of the former system. This method combined the results of voxel classification-based segmentation with results of active appearance model (AAM) segmentation of the cartilage compartments through an information fusion procedure. Experimental results for only FC compartment using the same sets of training and testing MR images indicated that AAM segmentation could approximately determine the appearance information of the compartments in most of the testing MR images. However, failure in some of the MR images prevented implementation the information fusion module as intended. Simply intersecting the segmentation results of the tissue classification and appearance modelling modules for information fusion, the hybrid segmentation method could not outperform the former voxel classification-based segmentation method with its highest mean DSC value of 73.78% for FC.

With regard to the secondary purpose, standard Marr-Hildreth edge detection and Harris corner detection methods were extended to run in 3-D volumetric images. The results of the standard methods, which were applied in 2-D slices of the volumetric images, were qualitatively compared with results of the 3-D methods. As a result, in knee MR images, 3-D Marr-Hildreth method prominently detected the principal bone and cartilage edges found by the standard 2-D Marr-Hildreth method gaining additional sensitivity to gradient changes along the slices. In volumetric images of FC, the proposed 3-D Harris corner detection method determined well-localized and more distinct interest points at salient positions close to the surface boundaries.

Keywords: Image segmentation, three-dimensional modelling, high-field MR images, knee joint, articular cartilage, osteoarthritis, voxel classification, region-growing, subsampling, Marr-Hildreth edge detection, Harris corner detection, correspondence finding, active appearance model, hybrid segmentation

ÖZET

DİZ EKLEMİNİN YÜKSEK ALAN MANYETİK REZONANS GÖRÜNTÜLERİNDE KIKIRDAK BÖLGELERİNİ 3-B OTOMATİK BÖLÜTLEME VE MODELLEME

Ceyda Nur ÖZTÜRK

Bilgisayar Mühendisliği Anabilim Dalı

Doktora Tezi

Tez Danışmanı: Doç. Dr. Songül ALBAYRAK

Manyetik rezonans (MR) görüntüleri kıkırdaksı anatomik yapıların elle veya otomatik bölütlenmeleri yoluyla şekilsel ve nicel değerlendirilmesine olanak tanır. Diz bölgelerindeki yapısal değişimler, özellikle kıkırdaksı dokuların bozulması, osteoartrit olarak adlandırılan bir hastalıkla sıkı ilişkili olduğundan kıkırdağın ölçümlenmesi veya görsellenmesi terapötik veya cerrahi uygulamaların etkinliğinin yanında bu hastalığın bulgu veya ilerlemesini saptayabilir. Bu tezde diz eklemi MR görüntülerindeki bütün femura ait kıkırdak (FK), tibiaya ait kıkırdak (TK), ve patellaya ait kıkırdak (PK) bölgelerinin anatomik ilgi bölgeleri için özelleşmiş yaklaşımlardan kaçınarak ve bilhassa sınırlı kaynakları olan sistemler düşünülerek tamamen otomatik bölütlenmesi ve modellenmesi temelde amaçlanmıştır. Hacimsel görüntüler için kenar ve ilgi noktaları gibi görüntü özelliklerinin genelde olduğu gibi iki boyutlu (2-B) kesitler yerine direkt üç boyutlu (3-B) hacimlerde tespitinin bazı faydalar sağlayıp sağlamayacağının araştırılması tezdeki ikincil amaç olarak belirlenmiştir.

Tezde sunulan ilk çalışmada diz eklemindeki tüm kıkırdaksı bölgeler Osteoartrit Girişimi'nden elde edilen yüksek alan MR görüntülerinde örnekle-yay yöntemiyle voksel sınıflandırmaya dayalı bir bölge büyütme algoritması kullanılarak otomatik bir şekilde bölütlenmiştir. Kısıtlı hafızası ve işlemci gücü olan sistemler göz önüne alınarak sınıflandırmanın hesabi karmaşıklığı eğitim MR görüntülerindeki arka plan voksellerinin alt örneklenmesi ve küçük bir önemli özellik alt kümesi seçilmesiyle azaltılmıştır. Düzgün, Gauss, çevre ilişkili (Çİ) seyrek ve Çİ sık alt örneklemeyi içeren farklı alt örnekleme teknikleri kullanılarak dört eğitim modeli oluşturulmuştur. Bölütleme

sistemi 10 eğitim 23 test MR görüntüsü kullanılarak denenmiş ve farklı eğitim modellerinin bölütleme başarıları üzerine etkisi araştırılmıştır. Deneysel sonuçlar göstermiştir ki tüm bölgeler için en yüksek ortalama Dice benzerlik katsayısı (DBK) değerleri özgün Çİ seyrek alt örnekleme tekniğinin eğitim modelleri kullanıldığında elde edilmiştir. Bu teknikle eniyilenen ortalama DBK değerleri FK, TK ve PK için sırasıyla %82,6, %83,1 ve %72,6 olarak bulunmuştur. Literatürdeki ilgili çalışmaların çoğundan farklı olarak, bu çalışma bir kıkırdak bölgesinin bölütlenmesinden önce bir ilgi hacmi bulma, bir kemik bölütleme veya kemik kıkırdak arayüzü belirlemeyi gerektirmemiştir. Dolayısıyla sistemde böylesi bir ön işlemin hesapsal karmaşıklığı giderilmiştir. Ayrıca sadece osteoartritli katılımcılar için tek türde MR görüntüsünün işlenmesine rağmen sistemin elde ettiği başarılar ilgili çalışmalarınkine benzerdir. Kısıtlı kaynaklı bir ortamda bir MR görüntüsünün tüm kesitlerinde tüm bölgelerin bölütlenmesi için takribi 30 dakikalık işleme süresi gelecek için ümit vericidir.

Ayrıca çoğunlukla önceki sistemin aşırı bölütleme problemlerinin üstesinden gelmek için özgün bir hibrit bölütleme yöntemi önerilmiştir. Bu yöntem kıkırdak bölgelerinin voksel sınıflandırma tabanlı bölütleme sonuçlarını aktif görünüm modeli (AGM) bölütleme sonuçlarıyla bir bilgi kaynaştırma yordamı aracılığıyla birleştirmiştir. Aynı eğitim ve test MR görüntü kümeleri kullanıldığında deney sonuçları sadece FK bölgesi için göstermiştir ki AGM bölütleme test MR görüntülerinin çoğunluğunda bölgelerin görünüm bilgisini yaklaşık olarak belirleyebilmiştir. Bununla beraber, bazı MR görüntülerindeki başarısızlık bilgi kaynaştırma biriminin planlandığı gibi uygulanmasını önlemiştir. Bilgi kaynaştırma için sadece doku sınıflandırma ve görünüm modelleme birimlerinin sonuçları kesiştirildiğinde hibrit bölütleme yöntemi FK için %73.78'lik en yüksek ortalama DBK değeriyle önceki voksel sınıflandırma tabanlı bölütleme yönteminden daha üstün olamamıştır.

İkincil amaçla ilgili olarak, standart Marr-Hildreth kenar tespit ve Harris köşe tespit yöntemleri hacimsel 3-B görüntülerde çalışmak üzere genişletilmiştir. Hacimsel görüntülerin 2-B kesitlerine uygulanan standart yöntemlerin sonuçları 3-B yöntemlerin sonuçlarıyla nitel olarak karşılaştırılmıştır. Sonuçta 3-B Marr-Hildreth yöntemi diz MR görüntülerinde kesit yönündeki eğim değişimlerine ek hassasiyet kazanarak 2-B Marr-Hildreth yönteminin bulduğu ana kemik ve kıkırdak kenarlarını belirgin bir biçimde tespit etmiştir. Hacimsel FK görüntülerinde önerilen 3-B Harris köşe tanıma yöntemi yüzey sınırlarına yakın çıkıntılı kısımlarda iyi konumlandırılmış ve daha bağımsız ilgi noktaları belirlemiştir.

Anahtar Kelimeler: Görüntü bölütleme, üç boyutlu modelleme, yüksek alan MR görüntüleri, diz eklemi, eklem kıkırdak, osteoartrit, voksel sınıflandırma, bölge büyütme, alt örnekleme, Marr-Hildreth kenar tanıma, Harris köşe tanıma, denklik bulma, aktif görünüm modeli, hibrit bölütleme

CHAPTER 1

INTRODUCTION

Automated segmentation and three-dimensional (3-D) modelling of anatomical structures in medical images has attracted significant interest from researchers since the invention of volumetric medical imaging modalities, such as computed tomography (CT) and magnetic resonance (MR) imaging. These technologies have paved the way for possibilities of quantitative and visual analyses that can benefit clinical diagnoses and treatments, surgical interventions, pharmaceutical research, and educational activities [1], [2], [3].

One such particular anatomical region of interest has been the knee joint for researchers. The knee joints are generally affected by a degenerative disorder named as osteoarthritis, which results in pain and movement disability in the joints due to deterioration of cartilage. The fact that in developed countries all of the people below the age of 60 are affected by and about 12% of the people above 60 symptomatically have osteoarthritis has increased the need for the methods that can be useful in diagnosis and the treatment of this disorder. Osteoarthritis is diagnosed and followed up by the expert radiologists depending proportionally on their expertise in knee MR images. When the need arises, the radiologists manually segment the compartments of interest for analysis. However, during manual segmentation both occurrences of intra-observer or inter-observer variations and long durations of the segmentation process led to design of fully automatic segmentation systems to aid in early diagnosis and treatment processes of osteoarthritis.

This chapter particularly reviews the fully automatic cartilage segmentation studies in the literature, and introduces the purposes and hypotheses of the studies presented in the thesis. In Chapter 2 the anatomy of a normal knee joint and some disorders due to traumatic and pathological syndromes in the knee joint are briefly described. The causes, symptoms, diagnosis, and treatment of osteoarthritis are clarified especially. Furthermore, the systems for semi-quantitative grading of this disorder in radiography and MR imaging are mentioned. Chapter 3 sheds light on the physics of the MR imaging by explaining the components of a typical MR scanner. Also it examines MR images in terms of their quality to represent the cartilage compartments.

In the first automatic segmentation study presented in Chapter 4, the whole femoral, tibial, and patellar cartilage compartments in the knee joint were segmented in high-field MR images obtained from Osteoarthritis Initiative (OAI) using a voxel-classification-driven region-growing algorithm with sample-expand method. One-versus-all voxel classifiers were constructed for tissue classification depending on the local image and voxel position features of each cartilage compartment in the MR images. Computational complexity of the classification was alleviated via subsampling of the background voxels in the training MR images and selecting a small subset of significant features by taking into consideration systems with limited memory and processing power. Therefore, different subsampling techniques, which involve uniform, Gaussian, vicinity-correlated (VC) sparse, and VC dense subsampling, were used to generate four training models. The automatic segmentation results obtained when the designed segmentation system was experimented with 10 training and 23 testing MR image data sets are evaluated.

Chapter 5 is about how Marr-Hildreth edge detection and Harris corner detection methods, which are mostly applied in two dimensional (2-D) images, can be extended to run in three-dimensional (3-D) volumetric images. The experiments involved applications of 3-D Marr-Hildreth method, 2-D Marr-Hildreth method that worked in slices, and the accelerated 3-D Marr-Hildreth method that reduced computational complexity in the knee MR images of OAI. Moreover, 3-D Harris corner detection method, 3-D Laplacian of Gaussian (LoG) filtering-based interest point detection method, and 2-D versions of these methods were run in volumetric images of femoral

cartilage model. The results of both the edge detection methods and interest point detection methods are qualitatively compared among themselves.

In Chapter 6, a hybrid segmentation method was proposed for delineation of the cartilage compartments in knee MR images based on both the voxel classification-based segmentation presented in Chapter 4 and active appearance model (AAM) segmentation. Therefore, the hybrid method enables fusion of probabilities obtained through the voxel classification-based segmentation and shape-texture information derived from AAM segmentation. The appearance model for each compartment was constructed with the same set of MR images used for training the former voxel classification-based segmentation system. Before the appearance model construction, dense set of correspondences were determined on the surfaces of cartilage atlases in training MR images through an iterative shape-context-based non-rigid registration approach. The error analyses of the former system and accuracies of AAM and hybrid segmentations in the same testing MR images are provided in the experimental results. Whether the hybrid system could improve the overall segmentation accuracies or not is discussed, in particular.

Chapter 7 is a discussion of the accuracies and performance of the voxel classification-based segmentation system described in Chapter 4 with respect to the related studies reviewed in Subsection 1.1.3. In addition to this, it concludes the studies presented throughout the thesis pointing out some future works possible.

Appendix A presents general information about the OAI data sets, and reveals demographics of the participants for a subset of OAI MR image data sets used in our studies. Appendix B gives mathematical basics and formulations for some of the algorithms that were useful in the appearance modelling procedure of the hybrid segmentation method described in Chapter 6.

1.1 Literature Review

Segmentation is a fundamental problem of computer vision to delineate the objects of interest in the images, and primarily affects the accuracy and precision of higher level operations for analyses of these objects. Although segmentation problem has been prevalently studied so far, it has not been flexibly handled overall. Because, the

developed segmentation methods mostly had approaches specialized for the objects to be segmented or required a kind of user-interaction that breaks the automaticity of the system [2].

Thresholding and region growing algorithms, classification and clustering techniques, watershed algorithm, statistical shape models (SSM)s, deformable models, graph-based algorithms, and atlas registration approaches are generally among the methods frequently applied in medical image segmentation [1], [4], [5], [6]. Different methods can be optimal depending on the anatomical structure of interest to be segmented. However, two or more of these methods are usually combined to improve the accuracies of the segmentation systems. Being independent of the method applied, totally automating the segmentation system including its initialization phase is an issue of concern to the researchers. Additionally, ability of the system to segment in 3-D paves the way for quantification and modelling of volumetric anatomical structures.

3-D cartilage segmentation problem is challenging due to increased computational complexity when processing high dimensional MR images, non-trivial separability of the cartilage tissue intensities and the intensities of other tissues, fairly thin morphology of the cartilage tissue, and degeneration of the cartilage in time due to osteoarthritis. SSMs [7] can achieve segmentation of some anatomical structures by modelling shape or texture variances between participants. However, despite the fact that the cartilage compartments have approximate shapes, solving the segmentation problem of cartilage in MR images purely via shape-based methods such as SSMs or registration of cartilage atlases is not possible when the pathological cases are considered. Therefore, as the bones in knee MR images are generally segmented with SSMs, cartilaginous structures are segmented with manual [8] or manifold shape-independent methods [9], [10], [11], [12]. Deformable models [13], graph-based methods [14], or classification-based approaches, all of which accomplish segmentation depending on intensity-related or derivative-related local image features, play an effective role in cartilage segmentation problem [9], [15], [16].

The coverage of this subsection is as follows. A number of knee MR image data sets mentioned to be used by the automatic cartilage segmentation studies in the literature are summarized in Subsection 1.1.1. Subsection 1.1.2 describes some of the

prevalently used validation measures to evaluate the accuracy of an automatic segmentation result. Studies in the literature, which realized fully-automatic segmentation of cartilage in MR images of the knee joint without any interaction during the testing phase, are reviewed in Subsection 1.1.3. For each study, the data processed, segmentation methods applied, experimental results obtained, and some critical evaluations are mainly presented. Subsection 1.1.4 includes a brief literature review of some 3-D edge and interest point detection studies, which are particularly related to Marr-Hildreth edge and Harris corner detection methods, since Chapter 5 focuses on extension of these methods into third dimension.

1.1.1 Knee MR Image Data Sets

Private data sets were preferred mostly by some earlier cartilage segmentation studies [8], [9], [15], [17], [18]. Segmentation of the Knee Images 2010 (SKI10) is a challenge for segmentation of cartilage pertaining to surgery planning in knee MR image data sets that focuses on only volumes of interest (VOIs) at the central load-bearing parts of cartilage. The data sets of SKI10 as well as the results of the studies that attended this challenge [10], [12], [19], [20] are available through the link of http://www.ski10.org/. Osteoarthritis Initiative (OAI) database, which is also obtained and used for the studies presented in this thesis, was used by many other works [11], [16], [20], [21], [22], [23], and publicly accessible at http://www.oai.ucsf.edu/. More detailed information on OAI database can be found in Appendix 0. The knee MR image database of Pfizer Longitudinal Study (PLS) was noted to be utilized by Shan et al. [10], [24], [25], and the database of Center for Clinical and Basic Research (CCBR) was processed by Dam et al. [12]. But both of PLS and CCBR databases seem to be not provided for public-use.

1.1.2 Validation Measures

Automatic segmentations can be evaluated using a number of validation measures [10], [26], [27] with respect to the reference segmentations, which are generally performed by the domain experts or trained segmenters manually using pointing software or semi-manually with the running of point correction algorithms. These reference segmentations are accepted as ground truth segmentations, but they are

always prone to inter-segmenter and intra-segmenter variability. Consequently, measuring the segmenter variability is also a focused issue in most of the studies for supporting the reliability of the system accuracy and precision.

Dice similarity coefficient (DSC) is a commonly used measure for validation, and is an important indicator of segmentation accuracy. Because, it is maximized in the case of a good compromise of sensitivity and specificity, which are true classification ratios of cartilage and background classes. If the sets of voxels in automatic segmentation and reference segmentation of an object are denoted by **A** and **B**, respectively, DSC, sensitivity, and specificity values can be computed according to the equations (1.1), (1.2), and (1.3). When the volumes of **A** and **B** are exactly the same, DSC measure reaches to its highest value of 1. If the volume of **A** is larger than **B**, which is the case of higher sensitivity and lower specificity, or the volume of **A** is smaller than **B**, which is the case of lower sensitivity and higher specificity, DSC measure decreases in value.

$$DSC(\boldsymbol{A},\boldsymbol{B}) = \frac{2\,|\boldsymbol{A} \cap \boldsymbol{B}|}{|\boldsymbol{A}| + |\boldsymbol{B}|} \tag{1.1}$$

$$Sensitivity(\boldsymbol{A},\boldsymbol{B}) = \frac{|\boldsymbol{A} \cap \boldsymbol{B}|}{|\boldsymbol{B}|} \tag{1.2}$$

$$Specificity(\boldsymbol{A},\boldsymbol{B}) = \frac{|\boldsymbol{A^c} \cap \boldsymbol{B^c}|}{|\boldsymbol{B^c}|} \tag{1.3}$$

Volume overlap error (VOE) in (1.4) is also a frequently preferred measure in the literature to indicate the error in overlapping volumes of **A** and **B**. Volume difference (VD) in (1.5) gives how much volume estimate of **A** differs from that of **B** with respect to the volume estimate of **B**, and yields zero value if these estimates are equal. However, the latter misleadingly results in low difference values if **A** and **B** both with similar volume estimates are at totally different locations, since it does not consider overlap of these volumes in the equation.

$$VOE(\boldsymbol{A},\boldsymbol{B}) = 100\left(1 - \frac{|\boldsymbol{A} \cap \boldsymbol{B}|}{|\boldsymbol{A} \cup \boldsymbol{B}|}\right) \tag{1.4}$$

$$VD(\boldsymbol{A},\boldsymbol{B}) = 100\frac{|\boldsymbol{A}| - |\boldsymbol{B}|}{|\boldsymbol{B}|} \tag{1.5}$$

Average symmetric surface distance (ASSD) and maximum symmetric surface distance (MSSD) are some of other measures that can be alternatively used to validate the automatic segmentations depending on only the boundary voxels of automatic and reference segmentations. Therefore, they can be convenient for contour-based segmentations, in particular. If the boundary voxel sets of **A** and **B** are denoted as $\mathbf{A}^b$ and $\mathbf{B}^b$, and the number of these boundary voxels as $N_{\mathbf{A}}{}^b$ and $N_{\mathbf{B}}{}^b$, ASSD is calculated as in (1.6) by averaging the sum of minimal distances between every voxel in $\mathbf{A}^b$ and the voxel set $\mathbf{B}^b$ ($d_i^{\boldsymbol{AB}}$) as well as the sum of symmetrically determined minimal distances with reversal of the set order ($d_j^{\boldsymbol{BA}}$). MSSD, which is also known as Haussdorf distance, finds the maximum value among these minimum distances $d_i^{\boldsymbol{AB}}$ and $d_j^{\boldsymbol{BA}}$ of the voxel pairs, which are computed between the sets $\mathbf{A}^b$ and $\mathbf{B}^b$ as formulated in (1.7). For a perfect segmentation result both ASSD and MSSD measures are zero.

$$ASSD(\boldsymbol{A},\boldsymbol{B}) = \frac{1}{N_{\boldsymbol{A}^b} + N_{\boldsymbol{B}^b}}\left(\sum_{i=1}^{N_{\boldsymbol{A}^b}} d_i^{\boldsymbol{AB}} + \sum_{j=1}^{N_{\boldsymbol{B}^b}} d_j^{\boldsymbol{BA}}\right) \tag{1.6}$$

$$MSSD(\boldsymbol{A},\boldsymbol{B}) = max\left(ma\,x\left(d_i^{\boldsymbol{AB}}\right), max\left(d_j^{\boldsymbol{BA}}\right)\right), \quad i=\{1,\ldots,N_{\boldsymbol{A}^b}\},\ j=\{1,\ldots,N_{\boldsymbol{B}^b}\} \tag{1.7}$$

Pearson's correlation coefficient (PCC) denoted with r is useful in validation of quantitative variables computed over the segmented anatomical object of interest with respect to the measures of reference segmentation. It basically describes how the two variables are linearly correlated. PCC equation in (1.8) is a ratio of the covariance of the computed variables and the product of their standard deviations, where x symbolizes the computed variable to be validated against y.

$$r = \frac{\sum_{i=1}^{n}(x_i - \bar{x})(y_i - \bar{y})}{\sqrt{\sum_{i=1}^{n}(x_i - \bar{x})^2}\sqrt{\sum_{i=1}^{n}(y_i - \bar{y})^2}} \tag{1.8}$$

1.1.3 Fully-Automatic Cartilage Segmentation

In some of the automatic cartilage segmentation studies, segmentation of the knee bones and determination of the parts of the bone surfaces that interact with the cartilage, which are so-called the bone-cartilage interface (BCI), were required in preprocessing stage to facilitate the reliable segmentation of the cartilage compartments [9], [16], [22]. Similarly, some other studies also required segmentation of the bones prior to cartilage segmentation, but did not focus on BCI determination [10], [11], [17], [20], [21], [23]. Unlike most of other works in the literature, few studies depended on the use of multi-modal MR images of the participants, which decreases the overlap between tissue intensity distributions, so structures such as bones, muscles, or cartilage can be well separated [17], [18], [28]. However, since the scanning of multiple MR images at a time for a patient is an uncommon clinical practice, such approaches may not be convenient for automatic segmentation of articular cartilage.

Table 1.1 summarizes the details about the fully automatic cartilage segmentation studies in the literature, and enables a comparative analysis in between them. An exceptional study also presented in the table is the one by Williams et al. [8], who segmented the cartilage compartments manually, but this study is important in terms of quantitative measures of the cartilage compartments and how these measures can be computed.

Folkesson et al. [15] segmented only the medial articular cartilage between the femur and tibia in 114 sagittal low-field Turbo 3-D T1 MR images of healthy and osteoarthritic populations using a region-growing algorithm based on the approximate k-nearest neighbours (k-NN). Around 40 significant features of voxels were selected among position, blurred intensities, the first, second, and third derivatives, and eigenvalues and eigenvectors of the Hessian and structure tensor matrices for the binary classifiers [29]. Then, randomly sampled central voxels in a test MR image were used as seed points for region growing if and only if they were classified as cartilage according to their approximate k-nearest neighbours among all voxel samples of 25 training MR images. The seeds were iteratively grown by merging with their 26-connected neighbours in the cartilage class. The average DSC measures between the automatic

and manual segmentations of the MFC and MTC were 77 ± 8% and 81 ± 6%, respectively, with 1% increase after the enhancement of position alignment. Statistically significant differences were detected with unpaired t-tests between the cartilage estimates of the healthy and osteoarthritic populations, and the greatest differences were obtained for the medial tibial cartilage. Although this segmentation algorithm is successful in handling the degenerative nature of the cartilage tissue with its voxel-based approach, it had a number of drawbacks. First of all, inclusion of all background voxels in training MR images to the training models results in an infeasible segmentation problem especially for high-field MR images with a great deal of voxels, and systems with limited memory or processing power. Second, over-segmented structures on the surfaces of the segmented cartilage compartments may occur due to misclassification of other nearby tissues as cartilage. In addition, because the greatest component grown as a result of region growing method was selected as the segmentation result, the algorithm cannot yield robust segmentation results in case a cartilage compartment is detected as more than one component due to severe deteriorations of the cartilage, or in case a false positive large component was mistakenly grown.

Even though Folkesson et al. [15] mentioned that their segmentation system lasted about 10 min on a standard desktop computer, Dam and Loog [30] pointed out the inefficient classification procedure of the study by Folkesson et al., and proposed sample-expand and sample-surround algorithms to solve the problem of classifying all voxels in an MR image for a segmentation task. They noted that the original algorithm by Folkesson et al. classified each voxel in a testing MR image twice by combining two binary classifiers which used around 500,000 training voxels for background, 120,000 for TC, or 300,000 for FC. Segmentation of an object of interest was realized through classification of the full object volume for the sample-expand algorithm, and classification of only the object surface for the sample-surround algorithm. The original algorithm and the two algorithms all yielded the same segmentation accuracies of 77% for MFC and 82% for MTC. On the other hand, 2.5-hour segmentation duration of the original algorithm was decreased to approximately 16 min with the proposed algorithms.

Yin et al. [16] identified initial volumes of interest for each bone and its associated cartilage using AdaBoost classifiers based on 3-D Haar features. The bone surfaces in volumes of interest were determined by graph searching of mean bone surface meshes of the three bones based on trained random forest classifiers, and BCIs on bone surfaces were extracted through AdaBoost classification of some geometrical and local appearance-based features. Then, they simultaneously segmented the bone and corresponding cartilage surfaces of the femur, tibia, and patella in 60 sagittal 3-D DESS MR images of the knee joint obtained from OAI with a graph-based approach oriented by random forest classifiers. Their method satisfied some constraints established on the non-intersection of different surfaces and different objects. As a result, DSC measures obtained were 84 ± 4%, 80 ± 4%, and 80 ± 4% for the FC, TC, and PC tissues, respectively. No statistical significance was found between the surface positioning errors of all bone and cartilage segmentations of the asymptomatic and osteoarthritic groups. Validation was performed partially using some of the slices in both train and test data sets due to a large labour intensity of 3-D manual segmentations. Consequently, their accuracies were not probably provided for the whole 3-D cartilage compartments.

Fripp et al. [9] compared performances of four different approaches: affine registration with a block-matching strategy, non-rigid registration via free-form deformation, tissue classification, and their hybrid deformable model (HDM), in 20 FS SPGR MR images of healthy volunteers for delineating the articular cartilage tissues of the knee joint. The tissue classification approach was inspired by the work of Folkesson et al., but modified to work in a localized region close to the bone-cartilage interface (BCI) extracted beforehand through segmentation of the bones by 3-D active shape models. Voxels were classified with support vector machine classifiers using a slightly different set of features and scale parameters. The HDM method referenced the same BCI to refine the cartilage segmentation through a 3-D deformable model depending on localization, patient specific tissue estimation, and a model of the thickness variation. Experiments showed that the best performing approaches were the tissue classifier and HDM. The two methods had no statistical difference in between their average DSC measures of FC, TC, and PC, which were 86 ± 4%, 81 ± 5%, and 82 ± 10%

for the former and 85 ± 8%, 83 ± 8%, and 83 ± 13% for the latter, respectively. Because deterioration of cartilage can affect the segmentation accuracies negatively [12], the higher DSC values obtained in this study than the DSC values of the other works can be attributed to the conduct of this study in MR images of only healthy participants.

Vincent et al. [21] developed an active appearance model (AAM)-based method for segmenting the bones and cartilage of the knee. The AAM model was built using 80 3-D DESS MR images of OAI data set, and the high-quality model correspondences were determined with minimum description length (MDL) groupwise image registration method. To build the model, first, manual segmentations of the anatomical structures were converted to surfaces. Then, MDL groupwise image registration method was applied to signed distance images derived from these surfaces. The outputs of this procedure were a reference mean image and a set of deformations to map mean image to each example image. Output reference mean image could be segmented using the zero-valued isosurface. Later, the mean surface was deformed for each example so that the deformed surface lied close to the segmented surface of the example to propagate the correspondence points. Cartilage correspondences were obtained depending on the intersection of normals to the bone correspondence points normally covered by cartilage with inside and outside of the cartilage structures. For femoral cartilage 37249 and for tibial cartilage 20459 correspondence points were determined. The model was matched to new images with multiple initial estimates at a grid of starting points, which were typically 30 mm apart on all directions. A hierarchical modelling scheme that involved a single model of femur and tibia, and individual models of femur, tibia, FC, and TC was used to enhance the segmentation results. Testing of the models was performed on SKI10 data set without additional tuning of the models. The average DSC values of their method were 86 ± 6% for FC and 86 ± 5% for TC as indicated by Shan et al. [10].

Lee et al. [22] segmented the knee bones using constrained branch-and-min-cut method to find the minimum energy on a Markov random field (MRF) based on bone shape priors, and determined BCI voxels via classification of voxels on bone surfaces with binary classifiers of position and local appearance. Then, for cartilage segmentation a set of reference patches from training set that correspond to each

local patch centred on sampled BCI voxels of the testing MR image were identified using normalized cross correlation. The reference patches enabled computation of regional probabilities for each voxel according to local shape and appearance information, and boundary probabilities for neighbouring voxel pairs depending on the regional probabilities. MRF optimization of local patch labels was accomplished by graph-cut technique using the regional and boundary probabilities. Final labelling of the voxels was realized with combination of the patch segmentations in a global graph-cut scheme. Three experiments were conducted in MR images of 17 participants at progression group of OAI data sets, which were validated against partial manual segmentations of two radiologists. Average DSC values obtained for the experiment, which involved LOOCV on 10 MR images, were 82 ± 3% for FC, 81 ± 3% for TC, and 82 ± 4% for PC with respect to the manual segmentations of the first radiologist. The experiment, which trained the system with 2-year follow-up scan of one of 9 participants, and tested with baseline scan of the same participant, showed that relevance of training and testing MR images results in better segmentation performance. Their approach was assessed to have tailored representations for objects of interest due to its ability to model local appearance and shape characteristics flexibly. Nevertheless, their experimental results with relatively limited data sets were not significantly different from those of other proposed methods.

Unlike most of other works in the literature, automatic segmentation system of Zhang et al. [17] handled four MR image sequences of the participants, which included T1-w FS SPGR, T2/T1-w FIESTA, T2/T1-w IDEAL GRE water and fat scans, to obtain multi-modal voxel intensities. In this manner, the overlap between tissue intensity distributions decreased, so structures such as bones, muscles, cartilage etc. could be well separated. Then, some geometrical features and local image structure-related features such as first order derivatives and eigen values of Hessian matrices were computed on multi-modal MR images. The geometrical features depended on the bone segmentations, which were determined by thresholding multi-modal image intensities. These features as well as the multi-modal image intensities were used to find parameters of a combined SVM-DRF classification model. SVM-based voxel classifier had generalized classification ability, and discriminative random field (DRF)

incorporated spatial correlations among neighbouring voxels. Same preprocessing and feature extraction stages were applied on a testing MR image, and then optimal voxel labels were predicted by an inference graphical model with loopy belief propagation depending on the learned classification model and its parameters. Experiments performed with 11 participants using leave one out cross validation (LOOCV) showed that employment of geometrical features in combination with other features in SVM-DRF classifier yielded the best segmentation accuracies for all compartments. With the average DSC values of 86 ± 9% for FC, 88 ± 10% for TC, and 84 ± 7% for PC, this study is seemingly the best among the works in the literature. Although these accuracies may be attributed to the effectiveness of the proposed SVM-DRF classification model, the advantage of collective processing of four MR image sequences is indisputable. However, scanning of four MR image sequences for a participant at a time is unusual for clinical practice. Also, they had a limited data set for only 11 participants with unknown health statuses, which may be another reason of increased accuracies. Furthermore, predictably, parameter tuning in the training phase was noted to be time consuming, even with a 48-core high performance computer, and their 33-minute testing duration for an MR image using such a system is more than the average.

Shan et al. [10], [24] developed a multi-atlas segmentation method with non-local patch-based label fusion, and used this to segment FC and TC compartments on longitudinal 706 T1-weighted SPGR MR scans of 155 participants. Their three-label segmentation method formulated the segmentation as a convex optimization problem which enabled globally optimal solutions for femur-tibia and FC-TC segmentations. For a testing MR image, initially the shape priors of femur and tibia were found with multiple atlases using affine and B-spline registrations. These shape priors and local bone likelihoods computed through a simple model were integrated into three-label formulation for optimal bone segmentation. Similarly, the shape priors for the cartilage regions were determined through affine bone transforms between the average-shape atlas or multiple atlases, and the computed bone segmentations. Local cartilage likelihoods were obtained from probabilistic k-NN or SVM classifications based on reduced set of features in comparison to Folkesson et al. [15]. Finally, the three-label cartilage segmentation energy was optimized after integration of the

cartilage shape priors and local likelihoods. As a result, multi-atlas registration with non-local patch-based label fusion and SVM produced the best mean DSC values of 76 ± 5% and 84 ± 4% for FC and TC, respectively. The reason of lower DSC values for the FC compartment was attributed to evaluation of only the load-bearing regions of this compartment. However, their method required at least 10 hours to segment an MR image with use of 18 atlases, and this duration can be unacceptably long in clinical practice. Also the three-label formulation was not appropriate for the segmentation problems with more than two objects of interest.

In another study by Shan et al. [25], the same three-label segmentation framework was extended by adding a temporal consistency term, which could mitigate image noise effects, and enable segmentation consistency across time points. They evaluated the proposed longitudinal segmentation on registered PLS longitudinal data sets. Comparison of longitudinal segmentation to temporally independent segmentation indicated that longitudinal model did not improve the segmentation results with respect to temporally independent segmentation, but increased temporal consistency of the segmentations was achieved.

Lee et al. [20] developed a segmentation algorithm, which consisted of mainly three procedures; multiple atlas building, locally-weighted voting, and region adjustment. Multiple atlas building involved non-rigid registration of all training MR images to a target image, and selection of the best matching atlases. On a testing MR image, the results of selected atlas registrations were merged by locally-weighted voting algorithm. For region adjustment, seed points inside and outside the bone regions were determined using the statistical information of bone, cartilage, and surrounding regions in the initial segmentation result. Then a graph-cut method depending on these seed points enabled revision of outliers, and inclusion of abnormal bone regions. Experimentation of the approach was on 150 MR images of SKI10 data set using two thirds of the images for the training, and the rest for the testing. The computation time of the proposed method was about 40 minutes, and average DSC values for femoral and tibial cartilage compartments were 72 ± 8% and 72 ± 7%.

In their automated bone and cartilage segmentation system, Wang et al. [11] first of all segmented the bones in the knee joint using statistical shape models based on the

correspondences of coherent point drift (CPD) method, with boundary refinement by random walks algorithm. Then, they computed features that captured spatial relations between the bones and cartilage compartments according to the anatomical landmarks on bone surfaces, and contextual information with intensity differences between the image voxels and their neighbours at random distances. Later, an iterative classification scheme using random forests algorithm with 60 trees at depth of 18 in each pass was run, during which semantic context features based on voxel classification probabilities were exploited after each pass of the classification to enhance performance in the next pass. Finally, a post-processing step refined the segmentations with smoothness constraints through graphics-cut optimization using the probabilities of being the background and the three cartilage tissues. Their experiments were conducted on 176 MR image sequences of OAI data set that belong to two visits of 88 participants at progression group, by splitting the data into equally-sized three subsets for 3-fold cross validation. Results indicated that context-depended features and distances to landmarks were very informative to embed spatial constraints, and 2-pass random forests classification significantly improved the DSC accuracies, which were computed as 85 ± 3% for FC, 84 ±4% for TC, 79 ± 9% for PC. These results obtained for the MR images of osteoarthritic participants were fairly successful in comparison to the results of other works especially for PC compartment. Nonetheless, they made no mention of the possibly high overhead of SSM-based bone segmentations and random forests voxel classification.

Hani et al. [18], [28] tried to solve inhomogeneous intensity and low-contrast issues of proton-based MR images with fusion of sodium and proton MR images. First, sodium-rich regions of sodium MR images were interpolated using cubic spline approach before fusion due to low resolution of these images. Then, histogram equalization was applied on fused MR images with saturation of high signal intensities. After that, connected components were selected, and convexity of region areas was measured for all image slices. Finally, automatic segmentation of AC was determined by edge detection of the objects in the image slices. The automated segmentation of articular cartilage (AC), without compartmental separation such as FC or TC, yielded sensitivity of 80.27%, and specificity of 99.65% on a data set of three 1.5 T sodium and proton MR

images in [18], and sensitivity of 80.21%, and specificity of 99.64% on a data set of four 1.5 T sodium and proton MR images in [28] compared to the manual segmentations. However their data set was fairly limited for the both studies, and since the scanning of sodium and proton MR images at the same time is an uncommon clinical practice, their approach is not a convenient way for automatic segmentation of articular cartilage.

Dam et al. [12] modified the work of Folkesson et al. [15] with the removal of the position alignment stage and introduction of a preprocessing stage of rigid multi-atlas registration instead to eliminate the differences between the training and testing MR images. A test MR image is transformed to the centre of the training MR images using the transformations, which registered the test image to the training MR images, combined with the median transformation computed from the similarity transformations in between the training MR images. Accordingly, rectangular regions of interest for the bones, cartilage compartments, and menisci were determined, and a voxel classification approach analogous to the approach of Folkesson et al. was applied within these interest regions. The problem in the study of Folkesson et al., which was selection of only the greatest component for the segmentation result even if a cartilage compartment was found as more than one component due to severe deterioration, was handled by inclusion of all other components with size greater than 15 % of the size of the greatest component. Validation of the proposed method was performed on 1907 low and high-field MR images of three distinct data sets including the OAI data set. The average DSC values obtained for MFC, LFC, MTC, LTC, PC, MM, and LM on OAI data sets containing 3-D DESS knee MR images of 88 osteoarthritic participants were 81 ± 4%, 84 ± 4%, 81 ± 5%, 87 ± 3%, 74 ± 12%, 76 ± 8%, and 83 ± 5%, respectively, when half of the images were used for the training and the rest for the testing. These results were comparable to the results of other works in the literature especially if the belonging of MR images fully to osteoarthritic participants was taken into consideration. They alleviated the computational complexity by running the voxel classification algorithm in constrained regions of interest, but could not solve the oversegmentation problem at the periphery of the cartilage compartments. They indicated that a solution of this problem was a post-processing step that refines the

segmentation boundaries with either local or global shape information. The use of multi-object shape models or local regularization processes such as graph-cut optimization was exemplified for this purpose.

Table 1.1 The details about some of the studies in the literature on fully-automatic segmentation of cartilage.[1]

Author(s)	Data Set: Train #\Test # [Size] (Resolution)	MR Type(s)\ View(s)	Anatomic Structures of Interest	[Localization], Segmentation Method(s)	Average Measure(s) [Comp. Time, Processing Speed, Memory]
Folkesson et al. [15] (2007)	Private: 25\114 (79 KLG≤1, 35 KLG≥2) [170x170x104 voxels]. (0.7x0.7x0.78 mm^3)	Turbo 3-D T1-w\ sagittal	MFC, MTC	[–], approximate k-NN-based region growing	DSC (MFC, MTC): (77± 8, 81±6)% Se (MFC, MTC): (80.3± 11.6, 86.8± 7.7)%, Sp (MFC, MTC): (99.96±0.01, 99.91±0.03)% [10 min., standard 2.8 GHz desktop, –]
Yin et al. [16] (2010)	OAI: 25+9 (15 incidence, 19 progression) \ 60 (48 incidence, 12 progression) [384x384x160 voxels] (0.37x0.37x0.7 mm^3)	3-D DESS WE\ sagittal	FB, TB, PB, FC, TC, PC	[AdaBoost classification based on 3-D Haar features], s-t graph cut oriented by AdaBoost and RF classifiers	DSC (FC,TC,PC): (84, 80, 80)±4% Se (FC,TC,PC): (80±7, 75±8, 76±8)%, Sp (FC,TC,PC): (100, 100, 100)±0% Unsigned Surface Positioning Error (FC,TC,PC): (0.45±0.12, 0.53±0.11, 0.53±0.14) mm Unsigned Surface Positioning Error (FB,TB,PB): (0.22±0.07, 0.23±0.06, 0.23±0.11) mm [20 min, Intel Core 2 Duo 2.6 GHz, 4GB RAM]
Fripp et al. [9] (2010)	Private: 20 (all healthy)\LOOCV [–] (0.23x0.23x1.5 mm^3) (0.46x0.46x1.5 mm^3)	T1-w FS SPGR\ sagittal	FB, TB, PB, FC, TC, PC	[ASM (for bones)], hybrid deformable model (for cartilage)	DSC (FC,TC,PC): (84.8±7.6, 82.6±8.3, 83.3±13.5)% Se (FC,TC,PC): (83.7±16.2, 82.9±20.7, 82.1±13.5)% Sp (FC,TC,PC): (99.9, 99.9, 100) ±0% [15 min, –, –]

[1] Some abbreviations used in the table: KLG: Kellgren Lawrence Grade, LOOCV: Leave One Out Cross Validation, w: weighted, inc.: incidence, prog.: progression; k-NN: k-Nearest Neighbours, CPD: Coherent Point Drift, MDL: Minimum Description Length, MRF: Markov Random Field, NCC: Normalized Cross Correlation, SSM: Statistical Shape Models, RF: Random Forest, AAM: Active Appearance Model, ASM: Active Shape Model, SVM: Support Vector Machine; MEDIC: Multiecho Data Image Combination, FS: Fat Suppressed, SPGR: Spoiled Gradient Recall, GRE: Gradient Echo, DESS WE: Double Echo in the Steady State Water-Excitation; DSC: Dice Similarity Coefficient, Se: Sensitivity, Sp: Specificity.

Table 1.1 The details about some of the studies in the literature on fully-automatic segmentation of cartilage. (cont'd)

Author(s)	Data Set: Train #\Test # [Size] (Resolution)	MR Type(s)\ View(s)	Anatomic Structures of Interest	[Localization], Segmentation Method(s)	Average Measure(s) [Approximate Comp. Time, Processor, Memory]
Fripp et al. [9] (2010)	Private: 20 (all healthy)\LOOCV [–] (0.23x0.23x1.5 mm^3), (0.46x0.46x1.5 mm^3)	T1-w FS SPGR\ sagittal	FB, TB, PB, FC, TC, PC	[ASM (for bones)], SVM-based region growing (for cartilage)	DSC (FC,TC,PC): (86.2±4, 81.2±5, 81.7±10.5)% Se (FC,TC,PC): (84.4±14.7, 86.7±6.7, 89.5±4)% Sp (FC,TC,PC): (99.7, 99.7, 99.8) ±0.1% [15-30 min, –, –]
Vincent et al. [21] (2010)	OAI: 80\– [384x384x160 voxels] (0.37x0.37x0.7 mm^3) SKI10: –\40 [–](–)	OAI: 3-D DESS WE\ sagittal SKI10: miscellaneous including T1-w and T2-w GRE or SPGR (some with FS)	FB, TB, FC, TC	[–], MDL groupwise registration, hierarchical AAMs	SKI10: VOE (FC, TC): (36.3±5.3, 34.6±7.9)% RMS surface distance (FB, TB): (1.49±0.44, 1.21±0.34) mm SKI10 score(FB, TB, FC, TC): (51±14, 51±14, 47±14, 61±17) [15 min., Intel Core 2 Duo and Core 2 Quad processors (Dell Vostro 420) , –]
Lee et al. [22] (2011)	OAI: Experiment 1: 10 (KLG≥2)\LOOCV Experiment 2: 7 (KLG≥2)\10 (KLG≥2) Experiment 3: 9x(1 (2-year follow-up)\1 (baseline)) [384x384x160 voxels] (0.37x0.37x0.7 mm^3)	3-D DESS WE\ sagittal	FB, TB, PB, FC, TC, PC	[energy optimization on MRF with constrained branch-and-mincut method (for bones), binary voxel classification (for BCI)] identification of reference patches with NCC, MRF optimization of local patch labels with graph-cut using regional and boundary probabilities, combination of patch segmentations with graph-cut	Experiment 1: DSC (FB): (95.2, 96.4, 95.4)% DSC (FC,TC,PC): (82.5±2.81, 80.8±2.57, 82.1±3.89)% Experiment 2: DSC (FC,TC,PC): (81.6, 80.2, 80.3)% Experiment 3: DSC (FC,TC,PC): (85.8, 83.6, 84.1)% [15-21 min, 2.4GHz core 2 Quad CPU, 2GB RAM]

Table 1.1 The details about some of the studies in the literature on fully-automatic segmentation of cartilage. (cont'd)

Zhang et al. [17] (2013)	Private: 4x11 (unknown health status)\ LOOCV [256x256x– voxels] (0.625x0. 625x1.5 mm^3)	T1-w FS SPGR, T2/T1-w FIESTA, T2/T1-w IDEAL GRE (water), T2/T1-w IDEAL GRE (fat)\ all sagittal	FB, TB, PB, FC, TC, PC	[multi-modal image thresholding, connected component labeling, distance transform (for bones)]; combined SVM-DRF classifier, graphical model with loopy belief propagation inference (for cartilage)	DSC (FC,TC,PC): (86.4±8.7, 88.0±10.2, 84.1±7.4)% Se (FC,TC,PC): (82.6±10.8, 86.0±12.2, 81.9±11.0)% Sp (FC,TC,PC): (99.6±0.2, 99.5±0.4, 99.7±0.2) % [33 min, 48-core high performance computer, –]
Hani et al.[18] (2013)	Private: –\ 3 proton and 3 sodium MR images [–x–x48] (0.47x0.51x1.5 mm^3) (proton) [–x–x12] (2.81x2.81x8 mm^3) (sodium)	3-D MEDIC\ sagittal (proton) 3-D GRE\ sagittal (sodium)	AC (FC+TC)	[fusion of proton and interpolated sodium MR images], histogram equalization, connected component selection, convexity measurement of region area, edge detection	Se (AC): 80.27% Sp (AC): 99.65% [–, –, –]
Shan et al. [10] (2014)	PLS: 18\ 706 (53% KLG≤1, 47% KLG≥2) [–].(0.31x0.31x1.0 mm^3) SKI10: 15/50 [–] (–)	PLS : T1-w 3-D SPGR\ coronal SKI10: miscellaneous including T1-w and T2-w GRE or SPGR (some with FS)	FB, TB, FC, TC	[affine and B-spline multi-atlas registration and three-label segmentation of bones], k-NN/SVM probabilistic classification, average-shape atlas or multi-atlas segmentation of spatial prior, three-label cartilage segmentation	PLS : DSC (FB, TB): (97±1.1, 96.7±1.2)% DSC (FC, TC): (76±4.8, 84.1±3.7)% [at least 10 hours] SKI10: DSC (FC, TC): (85.6±5.7, 85.9±4.7)% [–, –, –]
Lee et al. [20] (2014)	SKI10: 100/50 [–] (–)	miscellaneous including T1-w and T2-w GRE or SPGR (some with FS)	FC, TC	[–], multi-atlas non-rigid registration merged by locally-weighted voting, graph-cut-based method driven by statistical data	DSC(FC, TC): (71.7 ± 8.0, 72.4 ± 6.9)% [40 min, –, –]

Table 1.1 The details about some of the studies in the literature on fully-automatic segmentation of cartilage. (cont'd)

Wang et al. [11] (2014)	OAI: 176 (iMorphics: 2% KLG=1, 98% KLG≥2)\3-fold cross validation [384x384x160 voxels] (0.37x0.37x0.7 mm^3)	3-D DESS WE\ sagittal	FB, TB, PB, FC, TC, PC	[CPD-based SSM, random walks algorithm for segmentation of the bones], iterative random forests classification including contextual and distance-related features, graph-cut optimization	DSC (FB,TB,PB): (94.86±1.85, 95.96±1.64, 94.31±2.15)% DSC (FC,TC,PC): (84.96±3.3, 83.74±4, 79.16±8.88)% [–, –, –]
Dam et al. [12] (2015)	CCBR: 30 (80% KLG≤1, 20% KLG≥2)\ 110 (70% KLG≤1, 30% KLG≥2) [–] (0.7x0.7x0.8 mm^3) OAI: 44 (iMorphics: 2% KLG=1, 98% KLG≥2)\44 (iMorphics: 2% KLG=1, 98% KLG≥2) + 150 (VirtualScopics: 14% KLG≤1, 86% KLG≥2) + 1436 (Chondrometrics: 26% KLG≤1, 74% KLG≥2) [384x384x160 voxels] (0.37x0.37x0.7 mm^3) SKI10: 60\90 [] (-)	CCBR: Turbo 3-D T1-w\ sagittal OAI: 3-D DESS WE\ sagittal SKI10: miscellaneous including T1-w and T2-w GRE or SPGR (some with FS)	LFC, MFC, LTC, MTC, PC, LM, MM	[rigid multi-atlas registration], k-NN based region growing	CCBR: DSC(MFC, MTC): (80.4±5.9, 83.9±4.8)% [–, –, –] OAI (iMorphics): DSC (LFC, MFC, LTC, MTC, PC): (84.2±4.3, 81.4±4.4, 86.6±3.4, 81.2±5.5, 73.9±11.6)% DSC (LM, MM): (83±5.5, 76±8.3)% [–, –, –] SKI10: DSC on training set (FB+TB): 97% DSC on training set (FC+TC): [64,73] % (84.2±4.3, 81.4±4.4, 86.6±3.4, 81.2±5.5)% VOE (FC, TC): (25.9, 25.7)% RMS surface distance (FB, TB): (1.4, 1.0) mm SKI10 score(FB, TB, FC, TC): (63.2, 61.8, 65.4, 66.7) [–, –, –]
Williams et al. [8] (2010)	19 (all healthy)\ 31 (all osteoarthritic) [–] (0.62x0.62x1.6 mm^3)	T1-w GRE (for cartilage)\ sagittal T2-w (for bones)\ sagittal	FB, TB, PB, FC, TC, PC	[MDL-based SSM for correspondence, AAM (for bones)]; manual (for cartilage)	–, for each MDL SSM: [34 days, single 2.8 GHz Intel Xeon, –]]

1.1.4 Edge and Interest Point Detection in Volumetric Images

MR imaging, one of the medical imaging techniques used today, generates 3-D digital data that consists of rows, columns and slices. The fact that image processing algorithms are usually used in two dimensional (2-D) images has made it more common for MR images to be processed in slices. However, while processing a 3-D image, incorporating the data that belong to the third dimension directly into the process can allow the data to be more comprehensively assessed so that more reliable results can be obtained [31]. Moreover, 3-D edge or interest-point detection methods can detect robust features for reconstruction [32], mutual registration [33], correspondence finding [7], segmentation [6], or recognition [34] of anatomic structures in MR images.

Bomans et al. [32] performed 3-D reconstruction of anatomic surfaces in head MR images reasonably using morphological filtering and surface rendering algorithms, which were based on the contours found by 3-D Marr-Hildreth method [35], [36] accelerated with difference of Gaussians (DoG) technique. Pielot et al. [33] produced a reference template for the brain by using the interest points, which were detected in 3-D windows through multiplication of first-order derivatives, in determination of anatomical correspondences within sub-volumes. They took the advantage of these interest points and the template in application of a distance-weighted warping process. Brejl and Sonka [37] designed a new 3-D edge detection method, which could work on anisotropic images, with interpolation of the image intensities in narrow neighbourhoods and calculation of their gradient directions. They showed that their method was superior to the 3-D Canny edge detection algorithm in most of the experiments performed on different data sets.

Laplacian of Gaussian (LoG) filtering-based interest point detection was approximated by DoG operation in scale invariant feature transform (SIFT) algorithm by Lowe [38] to detect interest points at various scales. Scovanner et al. [34] proposed that the identifiers computed by expanding the SIFT algorithm into the third dimension could be more distinguishing in classification problems compared to 2-D SIFT identifiers for 3-D data such as MR images or videos. In their experiments for action recognition in

video images the 3-D SIFT identifiers increased the classification accuracies due to their higher capability of representation.

Harris and Stephens [39] developed Harris corner detection algorithm removing some disadvantages of the interest point detection method of Moravec [40], [41], which is based on the intensity differences between the local windows around the pixels and the shifted forms of these windows in different directions. The developed strategy to detect corners was more effective in terms of detection and repeatability, but had greater computational complexity due to convolution with a Gaussian window [42]. This convolution process was to take into consideration the intensity changes with respect to all directions, rather than only the 8 directions as in the method of Moravec, to assure rotation invariance. However, technically, the method of Harris computed intensity changes for the main directions of z and y alone. Therefore, Schmid et al. [43], who evaluated performances of several interest point detection methods, pointed out that the corners detected by the method of Harris were not completely independent of the direction of intensity changes, so cannot be regarded as rotationally invariant.

Laptev and Lindeberg [44] described a spatio-temporal interest point detector based on Harris corner detection method to identify significant local intensity variations in both space and time. Separate scale parameters were used for the spatial and temporal domains to compensate their independence from each other. The results showed that 3-D spatio-temporal interest points corresponded to important events in video data, and the scale-invariant N-jets descriptors of these events were effective for compact representation and interpretation of video events. Sipiran and Bustos [45] emphasized that interest point detection in 3-D data that is defined as meshes is problematic. Because, computation of derivatives is ambiguous due to arbitrary topology in 3-D meshes. They developed an interest point detector for 3-D meshes depending on Harris operator, and obtained high repeatability values for the detected interest points under several transformations. Yu et al. [46] evaluated performances of several state of the art volumetric 3-D interest point detectors, which included Harris corner detection. Their quantitative analyses showed that, despite being the slowest detector, maximally stable extremal regions (MSER) achieved the best performance

with respect to the proposed combined metric of repeatability and accuracy. However, they concluded that the actual choice of the interest points does not only rely on such metrics, but primarily affected by the purpose of application, which may be object recognition, correspondence finding, or segmentation.

1.2 Purpose of the Thesis

The primary purpose of this thesis was to design a system that can achieve fully automatic segmentation of four cartilage compartments, which are FC, LTC, MTC, and PC, in high-field 3D-DESS sagittal knee MR images of OAI exclusively for the osteoarthritic participants. The system was considered to work in all slices of the MR images to enable 3-D segmentation and visualization of the compartments to aid further analyses. In general, approaches specialized for the cartilage compartments of interest were avoided so that the system can be adaptable for segmentation of other anatomical structures, which may deteriorate in time. The resulting automatic segmentations of the compartments were to be validated against their semi-manually delineated reference segmentations.

First of all, the voxel classification-driven region-growing algorithm [15], [29] was intended for implementation as the segmentation method,, because it is an appropriate approach for the degenerative nature of the cartilage and does not require any operation prior to segmentation of cartilage. The system was especially targeted on platforms with limited resources to be able to conveniently respond without the need for sophisticated machines. For this purpose, one-versus-all classifiers were to be constructed for each cartilage compartment depending on effective training models, which could be generated using a number of subsampling techniques and smaller sets of significant positional and intensity-related local image features. The implemented system was expected to have comparable accuracies and efficiency with respect to the studies in the literature.

Secondly, proposing a novel segmentation approach was the purpose in the light of the studies in the literature on fully automatic cartilage segmentation. Accordingly, a hybrid segmentation method was to be realized to regulate the automatic segmentation results of the former voxel classification-based system with use of high-

level cues such as shape or texture via information fusion. Hence, misclassifications were expected to be corrected leading to an increase in the overall segmentation accuracies. For integration of high-level cues, compartmental appearance models were to be trained using dense set of correspondences on the surfaces of cartilage atlases. Then, AAM segmentation [47], [48] of the cartilage compartments formerly segmented by the voxel classification-based method was to be approximately achieved such that inter-participant transformations of the segmented cartilage compartments could also be enabled for information fusion.

Thirdly, Marr-Hildreth edge detection based on LoG filtering operation, which enables isotropic derivation, and Harris corner detection methods were intended to be extended to work in 3-D volumetric images. The differences of the resulting edges from those detected by the standard Marr-Hildreth method applicable in 2-D slices were to be evaluated using MR images of the knee joint. Moreover, whether the interest points detected with the extended LoG filtering-based or Harris corner detection methods have advantages over the points detected by the slicewise 2-D implementations of these methods was to be assessed in volumetric binary or intensity-based images of FC model.

From a broader perspective, the proposed cartilage segmentation and modelling systems in this thesis pave the way for analyses of cartilage with respect to the progression of osteoarthritis. Thus, they are aimed at supporting decisions of radiologists, orthopaedists, surgeons, pharmacologists, or other researchers for diagnosis or monitoring of osteoarthritis.

1.3 Hypotheses

The cartilaginous compartments of interest in knee MR images can be segmented without finding a VOI, requiring segmentation of the bones or determination of BCI unlike most of the studies in the literature. The voxel classification-driven region-growing algorithm has such a straightforward approach suitable for the degenerative nature of the cartilage. A cartilage segmentation system that depends on this algorithm can be improved in accuracies and performance if a cartilage vicinity-

correlated subsampling technique and a smaller set of significant features are used for the training models.

The oversegmentation problem of the voxel-classification-driven region-growing algorithm [12] and the unreliable segmentation problem of the shape-based approaches for degenerative anatomical structures [8] may be solved by a hybrid cartilage segmentation system. The probabilities of voxel classification-based segmentation may be integrated with the shape and texture information of AAM segmentation in this hybrid system through an information fusion procedure. Although there are different hybrid studies in the literature for cartilage segmentation in knee MR images, the proposed hybrid system is novel overall in terms of the way the segmentation approaches are combined. If the appearance models can accurately synthesize the cartilaginous compartments of interest in the testing MR images, the hybrid system may improve the accuracies of the voxel classification-based segmentation system, and the shape information derived from the model may be useful in determining the approximate loss of compartmental cartilage for the participants.

In addition to these, the standard algorithms for edge or interest point detection, which are applied in 2-D images, can be extended to work in 3-D volumetric images. Then, information along the third dimension is also taken into consideration. Hence, the edge or interest points detected by means of the extended methods may be more significant features to represent the objects of interest in volumetric images.

CHAPTER 2

THE KNEE JOINT

The main anatomical structures in a normal knee joint of the human body are briefly described in Subsection 2.1 of this chapter. In addition, some disorders related to the knee joint are mentioned in Subsection 2.2 with a particular emphasis on the osteoarthritis, which mostly affect the cartilage compartments. The causes, symptoms, and diagnosis and treatment methods of osteoarthritis are explained as well as some semi-quantitative approaches to grade this disease in Subsection 2.2.1.

2.1 Anatomy

Joints are where bones articulate with each other, and based on their anatomical designs they can be categorized as immovable joints, slightly movable joints, and freely movable joints. Freely movable joints in the body are synovial joints (Figure 2.1 (a)). The articulating surfaces of the bones in synovial joints are covered by articular cartilage that reduces the friction between the bones, and absorbs shocks. Synovial cavities, also known as capsules, surround the articulating surfaces of a synovial joint, and within those cavities there exists synovial fluid that provides lubrication and nourishment of the articular cartilage [49].

One of the most important synovial joints in the human body is the knee joint (Figure 2.1 (b)). It is formed by four bones: the femur, tibia, fibula, and patella, and movable due to articulations between the bones of femur and tibia, and the bones of femur and patella. During movement of the joint, wheel-shaped medial and lateral[1] condyles of

[1] Anatomical terms of location. Medial describes the state of being near the centre of the human body. Lateral describes the state of being near the right or left sides of the human body. Anterior and

femur roll on the flat medial and lateral articulating surfaces of the tibial plateau (Figure 2.1 (c)) whilst patella articulates with the patellar surface of the femur. The knee joint with these articulations permits the flexion (forward movement) and extension (backward movement) as well as slight internal and external rotation of the lower leg relative to the thigh.

Main anatomical structures of the knee joint are bones, cartilage compartments, ligaments, menisci, and a joint cavity filled with the synovial fluid as shown in Figure 2.1 (b) and (d). Some other anatomical structures involve bursae, fat pads, tendons and muscles. Most of these structures are connective tissues with specialized cells called chondrocytes embedded in collagen and elastin fibers that break down with age [50].

2.1.1 Bones

The four bones of the joint provide the knee with strength, stability, and flexibility. The outer layer of the bones is a thin, whitish skin layer known as the periosteum full of nerves and blood vessels, which supply oxygen and nutrients to the bone cells (Figure 2.1 (a)). Periosteum is continuous with the ligaments that connect the bone to the surrounding bones and the tendons that connect the muscles to the bone. The layer below is a dense and rigid bone with thousands of tiny holes and passageways for the vessels, which is called the compact bone. It is made up of calcium and minerals, and supports the weight of the body. In the hollow centre of the bone, which is known as medullary or marrow cavity, is the spongy bone marrow surrounded and protected by the compact bone. Bone marrow produces red blood cells, which carry oxygen, white blood cells, which fight infection, or platelets, which help stop bleeding [51].

Femur: The upper leg bone, commonly called the thigh bone, is the longest, heaviest, and strongest bone in the human body. The head of the femur forms the hip joint with the acetabulum of the hip (coxal) bone, while its bottom end forms the knee joint with

---

posterior are the terms used to describe the states of being near the front and back of the human body, respectively. Inferior and superior refer to the states of being below or above a given reference point.

tibia. In the knee joint femur has two round knobs called the medial and lateral condyles.

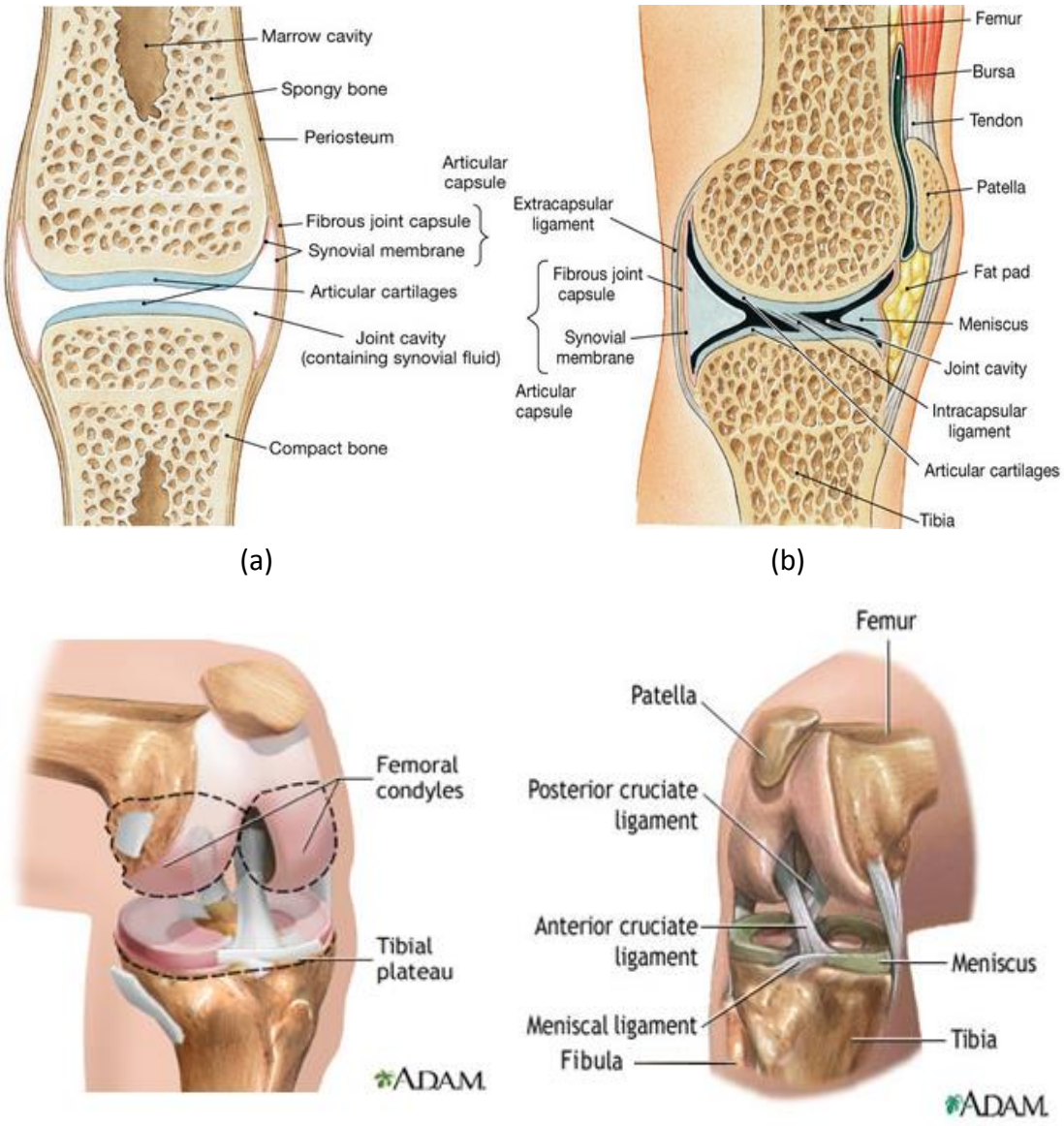

Figure 2.1 Cut section views of (a) a typical synovial joint and (b) a normal knee joint [49]. (c) The femoral condyles and tibial plateau. (d) Main anatomical structures of the knee joint.

Tibia: The larger and stronger of two lower leg bones, commonly called the shin bone, runs from the knee to the ankle medial to the fibula. The head of the tibia is made of two plateaus called the medial and lateral tibial plateaus, which forms the knee joint with the femoral condyles, and at the bottom end it is much narrower to form the ankle joint with the fibula and tarsus (an ankle bone). At the inferior edge of the lateral

plateau the tibia forms the proximal tibiofibular joint with the fibula, and this joint allows the position adjustment of the lower leg.

Fibula: A long and thin bone parallel to the tibia is on the lateral side in the lower leg. It interacts with the tibia both in the tibiofemoral joint at the head and in the ankle joint at the bottom. Fibula functions as a support for the tibia, which bears the weight of the body from the knees to the ankles.

Patella: A flat and triangular bone at the front of the knee joint, which is so-called the kneecap, protects the knee joint by relieving friction between the bones and muscles. As the knee moves, patella glides along the bottom front surface of the femur between the femoral condyles.

2.1.2 Cartilage Compartments

Articular surfaces of the bones are covered by the transparent hyaline articular cartilage, which is a thin, durable, extremely smooth, slightly flexible, and slippery tissue lubricated and nourished by the synovial fluid. Hence, articular cartilage protects the bones as the joint moves by reducing the friction between the bones and allowing the bones to move more easily against each other without pain. In addition, it acts as a shock absorber in cooperation with the joint cavity to resist impacts for the joints.

Since cartilage has almost no blood vessels in contrast to bones, it is kept alive by the surrounding synovial fluid. Whenever the joint is loaded, squeeze of fluid enables removal of waste products out of the cartilage, and with relief of the load, the fluid seeps back in by supplying the cartilage with oxygen and nutrients. Therefore, the frequency of the joint use affects the health of cartilage [52].

Cartilaginous compartments of the knee joint are femoral cartilage (FC) that covers the surface of inferior femur, tibial cartilage (TC) that covers the surface of superior tibia, and patellar cartilage (PC) that covers the surface of posterior patella. TC consists of two components called the lateral tibial cartilage (LTC) and medial tibial cartilage (MTC). When the knee joint is not flexed, LTC, MTC, and most of FC are located in tibiofemoral joint while PC and some of FC are in patellofemoral joint. Figure 2.2 depicts these cartilaginous compartments as a 3-D model.

(a) (b)

Figure 2.2 Cartilaginous compartments of the knee joint as 3-D models with (a) an inferior view and (b) a superior view. Red, green, magenta, and yellow represent FC, LTC, MTC, and PC compartments, respectively.

2.1.3 Joint Cavity

The joint cavity is surrounded by a thick and fibrous joint capsule that wraps around the knee joint. The synovial membrane is inside of this capsule, and a soft tissue called the synovium lines this membrane. The synovium secretes viscous synovial fluid, which fills in the joint cavity covering the surfaces of cartilage compartments. Thus, the synovial fluid aids lubrication of cartilage surfaces, and nourishes chondrocytes while at the same time it allows sliding motion between cartilaginous surfaces. In addition to these, synovial fluid can evenly distribute great pressures caused by the body movements or external forces without wear of the cartilage.

2.1.4 Bursae

In and around of the knee joint there are 13 sacs of connective tissue which are also lined by the synovial membrane and filled with the synovial fluid [49]. These sacs of various sizes are named as bursae, and they function to reduce the friction between bones, tendons, ligaments and soft tissue during the movement. One of the most significant bursae is the prepatellar bursa, which is located in between patella and skin to protect the patella.

2.1.5 Fat Pads

There are also pockets of adipose tissue so-called fat pads around the knee to protect the anatomical structures from external forces along with bursae. For example, the

largest fat pad known as infrapatellar fat pad absorbs shocks, and cushions the patella and ligaments during the movement of the knee joint.

2.1.6 Muscles

Three main muscle groups of the knee are quadriceps femoris with four muscles on the anterior thigh, hamstrings with three muscles on the posterior thigh, and the calf muscles. These muscle groups collaborate with each other in order to align, move, and stabilize the knee joint, so they play an important role in propelling of the body. Specifically, the quadriceps femoris muscles control extension of the leg at the knee and flexion of the thigh at the hip. The hamstrings group conversely contract for the flexion of the leg at the knee and extension of the thigh at the hip. The calf muscles control the flexion of the foot and the toes, so work for balancing the ankle joint and foot in addition to the knee joint.

2.1.7 Tendons

Fibrous and elastic portions of a muscle that connect the muscle to bones are known as tendons. The main function of tendons is to provide support for the joints. For instance, muscles of the thigh are connected to the patella by the quadriceps tendon to aid stabilization of the knee joint.

2.1.8 Menisci

There are two crescent-shaped pads entirely made up of rubbery fibrocartilage in between the articulating surfaces of the medial and the lateral femoral condyles, and the tibial plateau. These pads are called the medial meniscus and the lateral meniscus, respectively.

The menisci prevent direct interaction of the femur and the tibia during activities, and absorb shocks by spreading the compressive forces over a wider area. Therefore, the cartilage compartments are protected from damage. Moreover, they contribute to lubrication of the knee joint compartments and lateral stabilization of the joint.

2.1.9 Ligaments

Tough, fibrous and slightly elastic bands that surround the knee joint capsule are ligaments. They contribute the strength and stability of the knee joint by properly attaching the bones to each other. The major ligaments that support the knee joint are cruciate ligaments, collateral ligaments, patellar ligament, oblique popliteral ligament, and transverse ligament. Those within the articular joint capsule are called intrinsic ligaments, which include cruciate ligaments, and those outside of the capsule are called extrinsic ligaments, which involve collateral and popliteral ligaments.

The two collateral ligaments in the knee joint are medial and lateral collateral ligaments, also known as tibial or fibular collateral ligaments. The medial collateral ligament binds medial side of the femur to the medial side of tibia, as the lateral collateral ligament connects the lateral side of the femur to the lateral head of the fibula. They prevent excessive medial or lateral movements by reinforcing the sides.

The ligaments that cross each other in the centre of the knee are anterior cruciate ligament and the posterior cruciate ligament. The anterior cruciate ligament is located in front of the posterior cruciate ligament. The former obliquely extends from the lateral femoral condyle to the anterior intercondylar section of the tibia, while the latter obliquely extends from the inner surface of the medial femoral condyle to the posterior intercondylar section of the tibia. Anterior and posterior cruciate ligaments enable controlled movement of the tibia when sliding under the femoral condyles by limiting the forward and backward movements of the tibia to some extent as well as its rotation. Thus the knee is stabilized along its anterior and posterior axes.

The patellar ligament aligns the patella with the tibia by extending from inferior side of patella to tibial tuberosity, which is below the tibial plateau on the anterior surface of tibia. This 5 to 8-cm long band of fibrous tissue supports anterior side of the knee joint. In addition to these, the oblique popliteral ligament attaches posterior part of the lateral femoral condyle to the posterior side of the medial tibial condyle to support the back of the knee joint, and the transverse ligament runs from anterior lateral meniscus to the anterior medial meniscus.

2.2 Disorders

Stability and lubrication are two important characteristics of normal knee joint function, which were provided by the anatomical structures of the joint based on their morphological coordination and cooperative actions [52]. Any disorder of the knee joint directly or indirectly lead to malfunction of these characteristics, and such dysfunctional joints cannot totally recover even with artificial joint replacement.

The knee joint disorders can be due to traumatic or pathological syndromes. The traumatic syndromes involve ligamental, meniscal, and cartilaginous injuries and tears, dislocation of the patella known as patellar subluxation, rupture of the tendons, or bone fractures. Figure 2.3 illustrates some of these traumatic syndromes in the knee joint. Among some pathological syndromes in the knee joint are osteoarthritis[1], which is explained in more detail in Subsection 2.2.1, osteochondritis dissecans[2], infectious arthritis[3], chondromalacia patella[4], gout[5], rheumatoid arthritis[6], patellar tendonitis[7], knee bursitis[8], and Baker's cyst[9] [53].

Common causes of traumatic knee joint disorders are accidents or sudden actions while the weight is on a particular joint, which may occur during daily activities or sports in particular [50]. The underlying reasons of many of the pathological syndromes can be articular traumas previously mentioned, overuse of the joint, or gradual wear of the joint tissues with aging. Typical symptoms of these diseases include pain, swelling, crackles, tenderness, locks, giving way, or disability in movements with the damages in or dislocation of the anatomical structures.

---

[1] Degeneration of articular cartilage mainly due to aging and wear

[2] Fracture or separation of a bone segment underneath the articular cartilage due to lack of calcium or blood flow, which is known as common cause of the loose body in the joint cavity

[3] Inflammation of the joint because of infection with bacteria or fungus

[4] Irritation of the cartilage on the posterior surface of the patella due to patellar traumas or overuse

[5] Arthritis due to build-up of acid crystals in the joint

[6] Chronic inflammation of the joints owing to attack of a faulty auto-immune system to the joint tissues

[7] Inflammation of the tendon between the patella and the tibia

[8] Inflammation of bursae caused by overuse of or injuries to the knee joint

[9] A result of fluid accumulation in the posterior knee

Accordingly, the joint cavity can contain fragments of bone, cartilage, or meniscus, which are called the loose body. Moreover, arthritic diseases or injuries may lead to knee effusion, which is increase of fluid over time inside the joint cavity mostly due to inflammation [53], [54].

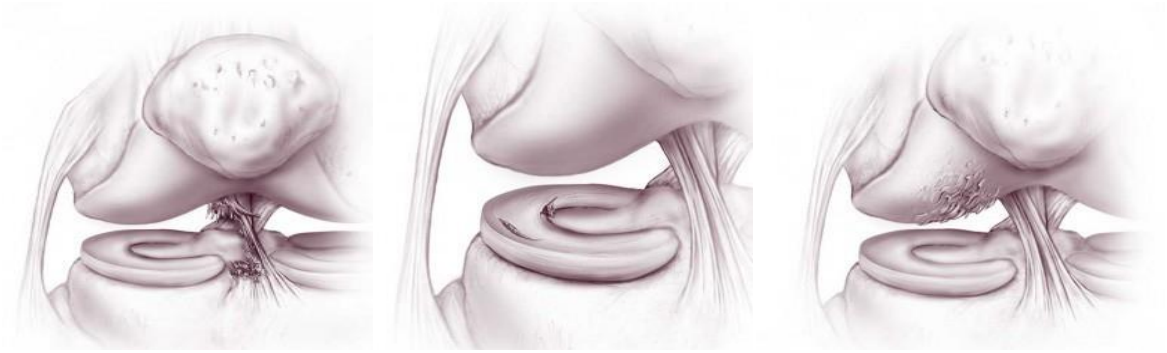

(a) (b) (c)

Figure 2.3 Illustration of some traumatic syndromes in a knee joint: (a) anterior cruciate ligament tear, (b) meniscal tear, and (c) cartilage deterioration [50].

In addition to the knee joint symptoms, some other techniques can aid in diagnosis of the joint disorders. Among these techniques are physical examinations, some tests such as drawer test[1] or valgus stress test[2], X-ray and magnetic resonance imaging techniques, and arthrocentesis[3] or arthroscopy[4] of the knee joint. Once diagnosed, the knee joint disorders can be treated with pain or reconstructive medicines and injections, RICE[5] and physical therapies, or arthroscopic and open surgeries. Arthroscopic surgery enables examination of the knee joint to find wears and tears of the meniscus and cartilage surfaces, detect loose bodies, and diagnose patellar misalignments in addition to treatment of these problems with minor operations. Thus, recoveries are quicker for arthroscopic surgeries than the open ones [54], [55].

[1] A test to examine the stability of the ACL and PCL by pulling and pushing the lower leg while holding the foot steady and the knee bent

[2] A test to examine injuries to MCL and LCL by pushing the lower leg laterally and medially, respectively, while holding the thigh steady

[3] Insertion of a needle into the knee joint space, and aspiration of synovial fluid

[4] A surgical operation with use of an endoscope, which is a flexible tube with camera and surgical tools on its end

[5] A therapy for sprains and injuries, which is combination of resting, ice treatment, compression with bandages, and elevation of the joint close to or above the level of heart

2.2.1 Osteoarthritis

Osteoarthritis is the most common form of arthritis that leads to articular pain, stiffness, and swelling due to significant deterioration or destruction of cartilage or degradation of the synovial cavity filled with synovial fluid. This degenerative joint disease mostly affects the load bearing regions of the thigh, knees, and spine.

In developed countries with large populations of the elderly and obese people, osteoarthritis is highly prevalent and assessed as the main reason of disability. Approximately one third of the people are affected by this disease before they reach middle age, and nearly all of them is affected before the age of 60, but half of these people do not have any symptoms of the disease at all. Only 12% of the people at the age of 60 or above have symptomatic knee osteoarthritis [56].

2.2.1.1 Causes and Symptoms

Deterioration of the cartilage mainly due to aging, excess weight, poor posture, articular overuse, and injuries can cause osteoarthritis. However, fractures of bones, meniscal problems, or ligamental tears can indirectly contribute to cartilage deterioration and, in consequence, osteoarthritic joints. Moreover, heredity and abnormal skeletal phenotypes are among the factors that make a person more prone to have this disorder. Some pathological syndromes such as inflammation or rheumatoid arthritis, diabetes, and hypothyroidism may also pave the way for osteoarthritis [57].

Some of the main symptoms of osteoarthritis are degradation and loss of articular cartilage, structural changes in bone, degeneration and inflammation of synovium, discomfort, pain, swelling, stiffening, grating, and loss of mobility of the affected joints, particularly during and after activity [56], [57]. Most significant cartilage deterioration occurs in central medial regions of tibiofemoral cartilage and posterior femoral cartilage [58], [59]. Once the cartilage softens and begins to deteriorate, in fact all other anatomical structures of the joint get affected. Deterioration process of cartilage can continue until most of this tissue is removed from the bone surfaces [54]. As a result of full-depth articular cartilage damages, local regions where articulated bones rub each other occur on the subchondral bone surfaces normally under cartilage.

Therefore bone spurs, known as osteophytes [60], may be formed in the joint to repair the cartilage damage and provide smoother joint surface. However, this attempt by the joint cannot resolve the problem due to lack of cartilage over the spurred bone surfaces [52]. Although articular cartilage lacks nerves, the frequency and degree of pain in the joint increase with the progression of osteoarthritis due to loose bodies, osteophytes, inflammation of the synovium, and fluid accumulation. In addition to these, in time osteoarthritis may cause skeletal abnormalities such as bowed legs, which is a consequence of the fact that medial side of the joint is affected by osteoarthritis more than the lateral side.

2.2.1.2 Diagnosis and Treatment

Since osteoarthritis progresses gradually, it may be difficult to definitively diagnose this disease in its earlier phases. Diagnosis of osteoarthritis is commonly made by examining the knee joint physically and paying attention to history of the disorder in patient. Arthrocentesis or blood tests can aid for diagnosis. Arthroscopy can be used to directly examine the deteriorated joint compartments such as cartilage and menisci. However, CT and MR images can non-invasively indicate the cartilage lesions, joint space narrowing (JSN) between the bones, osteophytes, and cysts, therefore are very effective to recognize osteoarthritis [57].

The damaged cartilage has a limited ability to repair itself, and if it could, recovery may take months depending on the severity of the damage [52], [54]. According to a longitudinal study on 43 osteoarthritic patients over 1.8 years in average, it was shown that 12% of the lesions prevalent at baseline were not detectable at follow-up, 6% changed to a lower grade, 32% remained the same, and 50% progressed towards higher grades [58]. Whether the disappeared lesions were healed, repaired, or could not be detected on follow-up examinations remained unclear. However, when the damage cannot be naturally repaired and tend to progress, medication and surgical procedures are generally preferred as treatment methods to reduce the symptoms and prevent the progression [61]. Approaches such as bringing in new cells or drilling can repair small cartilage lesions by stimulating the formation of cartilage cells.

Medium to large cartilage lesions can be reconstructed by filling of the defects with autologous tissue or synthetic material [62].

Heat and movement of the joints enable lubrication of cartilage, strengthen the muscles, and restrain pain. Therefore, simple precautions for early treatment can be physical therapies, daily exercises, and thermal baths. Furthermore, walking aids, shock-absorbing shoes or walking ways, braces to reduce the stress on medial knee, and staying fit can protect the joint [57].

When these approaches were not useful for treatment, arthroscopy can be a solution for cleaning loose bodies or stimulating the development of cartilaginous tissue. Bowed legs can be straightened with a procedure called as proximal tibial osteotomy, in which the angles of the legs are re-aligned to reduce the pain and delay progression of the disorder in medial joint. The final treatment solution for osteoarthritis in the knee is replacement with an artificial knee joint. But, this solution is operative only a few decades, so more preferable for the elderly than the young.

2.2.1.3 Semi-Quantitative Grading

Kellgren-Lawrence grading system is used to define the severity of osteoarthritis with one of five grades in radiography. Kellgren-Lawrence grade (KLG) 0 indicates the absence of any radiographic finding regarding osteoarthritis; KLG 1, possible JSN and initial phases of osteophytes (bone spurs around the joint); KLG 2, probable JSN and explicit osteophytes, KLG 3, explicit JSN, multiple osteophytes, sclerosis (tissue stiffening), and probable deformation of bones; and KLG 4, large osteophytes, apparent JSN, extreme sclerosis, and significant deformation of bones [63]. Some other grading systems defined for the same purpose in MRI are whole-organ review MRI scoring system (WORMS), Boston-Leeds osteoarthritis scoring system (BLOKS), and knee osteoarthritis scoring system (KOSS) [62]. These grading systems are more comprehensive, and assess both the cartilage and its surrounding anatomical structures according to some described percentage damage intervals [64], [65].

CHAPTER 3

MAGNETIC RESONANCE IMAGING

Having its roots in 1940's, magnetic resonance imaging (MRI) is today one of the most important techniques in medicine to generate the anatomical images which are useful for diagnosis of many disorders, clinical researches, or operative decision processes. Among the reasons why MRI is widely preferred are its non-invasiveness, high quality in tissue discrimination, and non-hazardous operating based on radio frequency (RF) signals lack of molecule-ionizing energy that may damage the tissues.

Magnetic resonance (MR) scanners, which have magnetization capability higher than 1.5 Teslas (T), are called high-field scanners, while those with magnetization capability lower than 1.5 T are called low field scanners. Even though the latter produces lower quality images, they have reduced costs per scan, for installation and maintenance as well as being highly comfortable without claustrophobic feelings and with minimal noise level [15]. However, the former generates higher quality images which enable better quantification and morphological evaluation of anatomical structures via manual or automated image segmentation techniques. MR machines incorporated with such automated functionalities for certain structures are referred as quantitative MRI [61]. Table 3.1 comparatively summarizes the high-field and low-field scanners.

Table 3.1 Comparison of low-field and high-field scanners.

Low-field Scanners	**High-field Scanners**
Relatively lower quality images	High quality images
Low scanning and maintenance costs	High scanning and maintenance costs
Minimal noise level	High noise level
No reason for claustrophobic feelings	Lead to claustrophobic feelings
Enable morphologic and quantitative evaluation	Enable better morphologic and quantitative evaluation

3.1 Physics of MRI

MRI principally works based on the excitation of the magnetic moment of hydrogen nuclei existent in different tissue molecules such as water and fat in order to produce images [2]. The hydrogen nuclei each spinning around its own axis as a charged particle have a magnetic moment, and since normally their direction of spin is randomly orientated, there is no dominant magnetic field exerting on them. A typical MRI scanner (Figure 3.1) is composed of four components; the primary magnet, gradient coils, RF coils, and a computer system [66]. Each component is briefly explained through the following subsections.

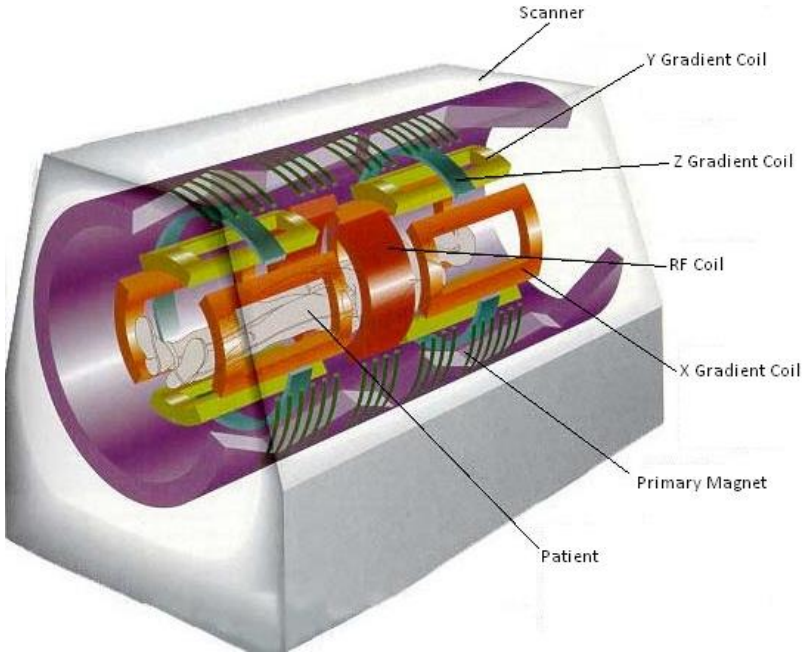

Figure 3.1 A typical MRI scanner [67].

3.1.1 Primary Magnet

The primary magnet transmits a strong external magnetic field to the human body it surrounds, which results in precession of the nuclei in the body around the direction of the field. The nuclei precess either being parallel (spin-up) or anti-parallel (spin-down) to the direction of the magnetic field. Because the nuclei in spin-up state have lower energy compared to the ones in spin-down state, there can be found more nuclei in spin-up state, and this generates a net magnetization along the external field.

All spinning nuclei have arbitrary precession frequencies and phases. The precession frequency $w_0$of a spinning nucleus in an external magnetic field $B_0$is called Larmor frequency, and given by the equation (3.1), where γ is a constant of gyro-magnetic ratio depending on the nucleus type, e.g. γ of hydrogen is $42.6\left(\frac{MHz}{T}\right)$.

$$w_0 = \gamma B_0 \tag{3.1}$$

3.1.2 Gradient Coils

In order to localize slices and to obtain spatial information on each slice, magnetic fields generated by gradient coils are superimposed over the external magnetic field so that the external magnetization in places other than the slice of interest is cancelled. Three oppositely positioned gradient coils are available in MR scanner for sagittal, coronal, and axial (transverse) imaging which are depicted in Figure 3.2.

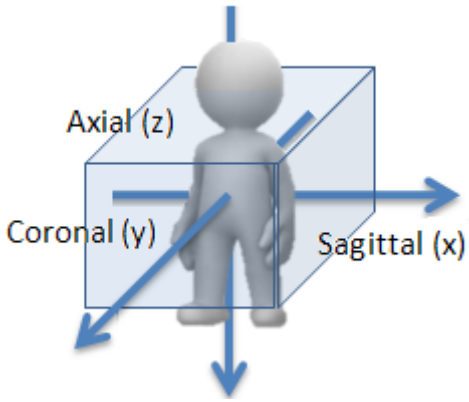

Figure 3.2 Sagittal, coronal, and axial imaging planes.

3.1.3 RF Coils

RF coils transmit RF pulse to form a secondary magnetic field (B_1) over the external magnetic field (B_0), and receive the signals in MRI scanner. When an RF pulse at the same frequency with the Larmor frequency of the nuclei is applied, the system starts absorbing the energy, and this case is called nuclear magnetic resonance. Then, some spin-up nuclei turn into spin-down state, and the precessions of the nuclei are synchronized, in other words the precessions become in-phase. As a result, the in-phase net magnetization is headed towards the transverse plane at perpendicular angles to the direction of the external magnetic field. After termination of the RF

pulse, the nuclei return to their prior magnetization states influenced purely by the external magnetic field. This event known as relaxation decreases magnetization in the transverse plane when increases the magnetization along the external magnetic field. Such varying net magnetic field results in free induction decay during which the receiver RF coils receive the current induced in the transverse plane to generate images. Two relaxation processes are further explained in the following subsections.

T1 Relaxation: As some of the nuclei turn back to spin-up state due to loss of energy, the energy from the RF pulse stored in the spin system is transferred to the surrounding lattice, and the magnetization along the external magnetic field is recovered. This process is longitudinal relaxation, or spin-lattice relaxation. Time needed to recover 63 % of the relaxed magnetization in the direction of the external magnetic field is the decay time T1, and five times T1 indicates when the longitudinal relaxation is almost complete. Because T1 depends on the size and bonding type of the tissue molecules, it has an important function in imaging and contrast of different tissues. For example, small and movable water molecules loosely bonded in liquids have long relaxation times since they are limited in interaction with their surrounds, whereas large fat molecules in dense atomic bonding have short relaxation times.

T2 Relaxation: The decay of magnetization in transverse plane because of de-phasing of the nuclei precessions is transverse relaxation, or spin-spin relaxation. T2 is spin-spin relaxation time constant, and is significantly shorter than the spin-lattice relaxation time T1, because spin-spin interaction is stronger. However, similar to T1, T2 is shorter for bodies with strong bonding of nuclei compared to liquids with loose bonding of nuclei.

Now that inhomogeneity in the magnetic field cause additional de-phasing of spins, in fact T2 is shorter than expected which is then called effective time constant T2*. To reverse the effect of the inhomogeneity, a second RF pulse is applied after a time period of τ. At the echo time after another time period of τ, the spins have recovered and a new signal less in amplitude called spin echo is measured.

3.1.4 Computer System

The received RF signals are processed by a computer system to produce the final MR images to be displayed. After analogue to digital conversion of the signals is performed, the resulting temporary frequency domain images are transformed to the spatial domain images via inverse Fourier transform. Each element of a digitalized spatial domain MR image is called a voxel, which is abbreviation of volume element.

3.2 MRI for the Knee Joint

MR scanners can generate highly detailed images of the knee joint, so most common means to directly visualize the cartilage. It enables detection of cartilage lesions and allows contrast adjustment to highlight different tissue types [62]. Furthermore, MR images are known to be effective in quantifying articular cartilage in the knee when processed through robust image segmentation methods. The reliability of MR imaging in morphological assessment and quantification of cartilage has been proven by a number of segmentation studies validated through the method of water displacement of surgically retrieved tissues using cadaveric joints, amputated joints or patient joints prior to total knee arthroplasty [61]. Therefore, cartilage loss in osteoarthritis can be non-invasively measured from MR images, and this aids in monitoring the effects of surgical or pharmacological treatments.

The measures obtained via automatic segmentation must be scalable for the proper analysis of large number of clinical trials, and sensitive enough to small and localized changes in cartilage thickness for early diagnosis of the osteoarthritis. MR images suitable for cartilage quantification need sufficient signal-to-noise ratio (SNR) and contrast-to-noise ratio to delineate the bone and cartilage surfaces, high spatial resolutions within 0.5-2.5 mm to measure the thickness of cartilage either healthy or worn, and reasonable scanning times to prevent movement artefacts.

3.2.1 Imaging Standards to Highlight Cartilage

Although high-field MR scanners with magnetization capability greater than 1.5 T have better imaging quality than low-field MR scanners, cartilage measures at 3 T had only small differences compared to measures at 1.5 T [68]. Some MR imaging standards

involving fat-suppressed (FS) T1-weighted spoiled gradient echo (SPGR), which is also named as fast low-angle shot (FLASH), or selective water excitation (WE) 3-D double echo in the steady state (DESS) are particularly effective for representing cartilage tissue [62]. However, in a study of National Institute of Health 3-D DESS standard at 3 T had measurements consistent with SPGR standard at 3 T [69]. Furthermore, sagittal MR images can better visualize the articular cartilage in a knee joint without loss of continuity of the compartmental tissue. Figure 3.3 shows slices of some OAI MR image data sets in various standards and imaging views.

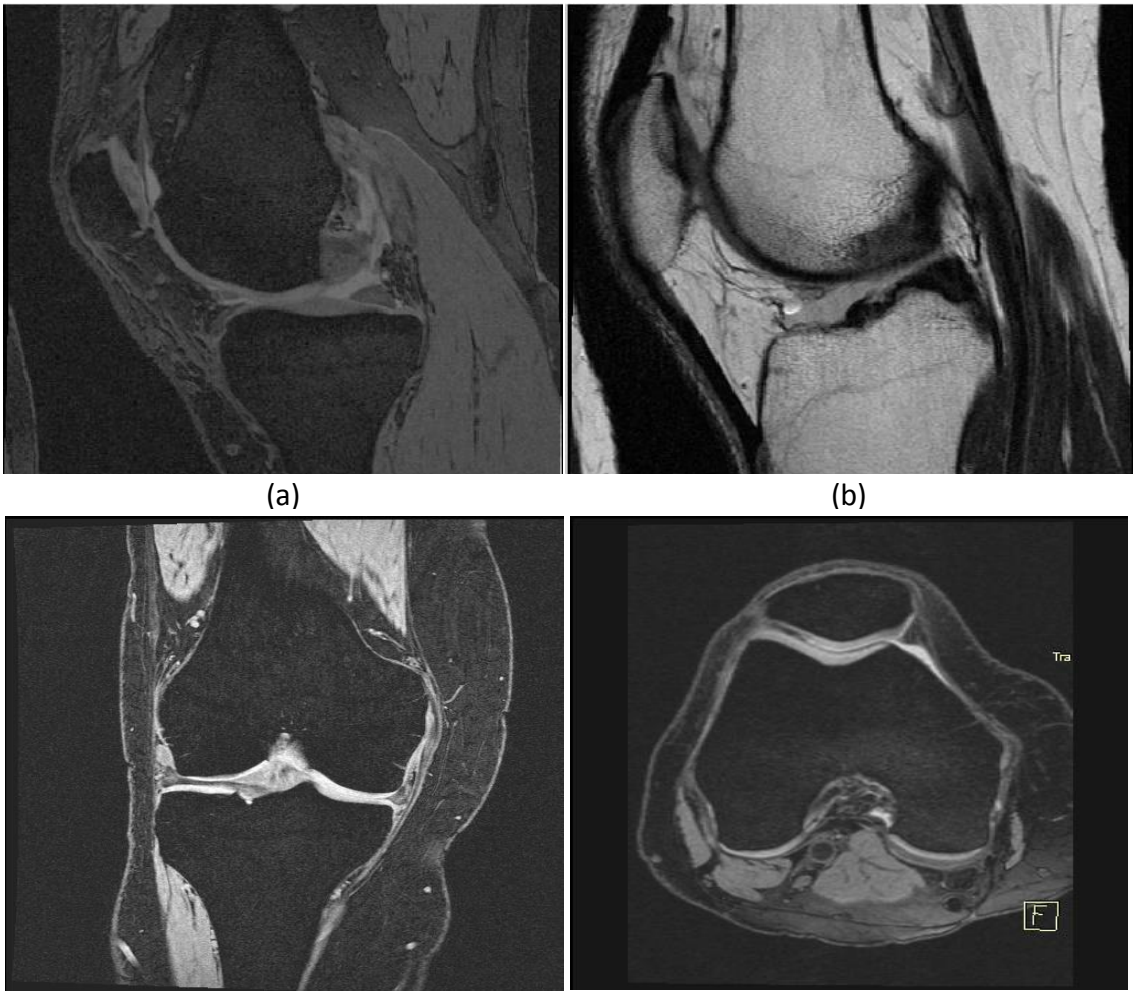

Figure 3.3 MR image slices of the knee joint in (a) sagittal 3-D DESS, (b) sagittal T2 map, (c) coronal T1 3-D FLASH, and (d) axial multi-planar reconstruction standards.

The sagittal OAI MR images scanned at 3T in 3-D DESS WE standard were used in the studies presented in this thesis. Frequency selective WE is a way of fat suppression that leads to higher contrast in between tissue types, and has shorter acquisition

times. In reconstruction of 3-D DESS MR images two or more gradient echoes are acquired by separating each pair with a refocusing pulse, and the data from these echoes are combined. This standard allows shorter acquisition times than SPGR, high SNR, high cartilage-to-fluid contrast, multi-planar reconstruction due to isotropic voxels, and decreased partial volume artefacts. Along with these strengths in imaging the cartilaginous tissue, some of its drawbacks include unreliable depiction of signal intensity changes within cartilage and vulnerability to susceptibility artefacts [62].

3.2.2 Anatomical Structures in Knee Joint MR Images

With better inter-tissue contrast and high-quality imaging capabilities, MR images have been widely preferred in the literature to realize the segmentation of articular cartilage in the knee joint. Studies aimed at reliable systems for monitoring the evidence or progress of osteoarthritis segment some or all of the cartilage compartments in knee MR images. In addition, segmentation of bones can be performed to aid the delineation of cartilage in local volumes. Synovial fluid, ligaments, and menisci are usually anatomical structures of no interest for such segmentation systems. Nonetheless, since they are located near cartilage compartments and have similar appearance to cartilage in MR images, they may be easily confused with cartilage tissue. Therefore, their accurate separation from the segmented cartilage compartments is also an important issue for robust systems.

Figure 3.4 depicts the bones and cartilaginous compartments that were segmented semi-manually in a slice of a knee MR image in 3-D DESS standard and with a sagittal view, which is cross-sectional view orthogonal to the left-right directions of the human body. The axial labels of the MR image with respect to the reference frame of an MR scanner are also designated in the upper left side of the figure. Appearances of bone, cartilage, or some other anatomical structures of the knee joint in axial FS and coronal MR image slices are as in Figure 3.5. It can be noticed in the axial slice in Figure 3.5 (a) that the cartilage is bright, and the synovial fluid is even brighter.

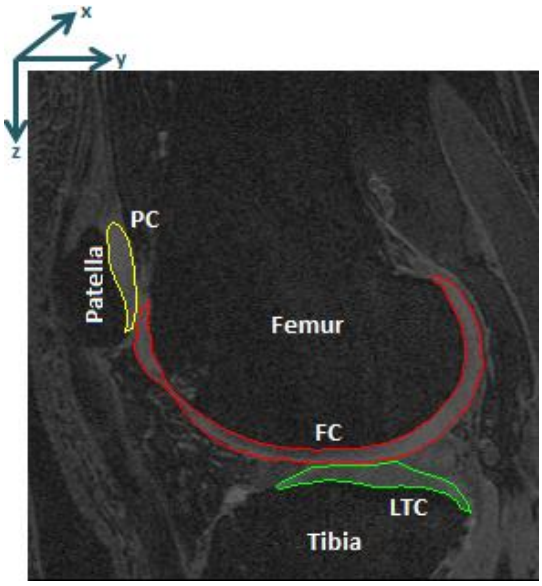

Figure 3.4 The compartments of FC, LTC, and PC, which are delineated in red, green and yellow, respectively, and their corresponding bones labelled in a sagittal 3-D DESS MR image slice.

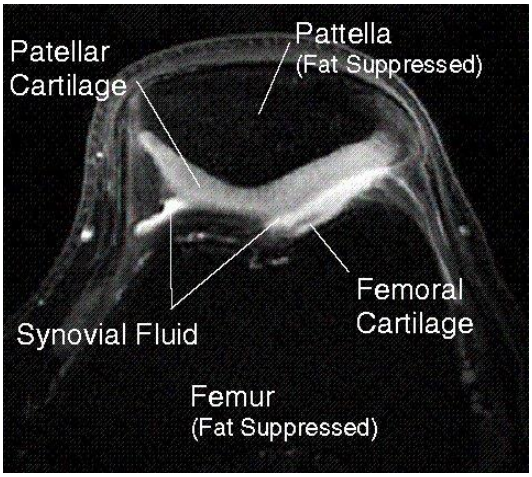

(a)

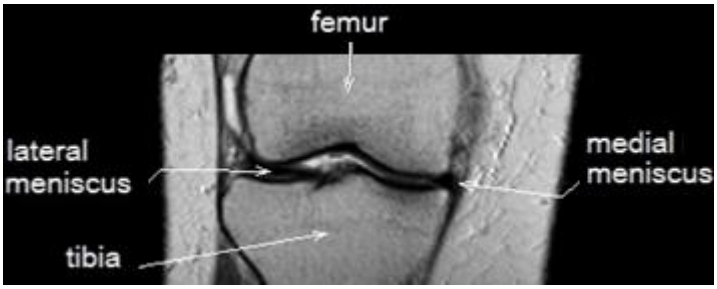

(b)

Figure 3.5 Appearances of some anatomical structures of the knee joint in (a) an axial MR image slice and (b) a coronal MR image slice [70].

CHAPTER 4

AUTOMATIC SEGMENTATION OF CARTILAGE WITH AN IMPROVED VOXEL-CLASSIFICATION-DRIVEN REGION-GROWING ALGORITHM

The study presented in this chapter focuses on the classification-driven region-growing algorithm proposed by Folkesson et al. [15], because this algorithm is an appropriate segmentation method for the degenerative nature of cartilage with its voxel-based approach compared to methods strictly depending on the shape information of the compartments of interest such as statistical shape models [7], [47], [48], [71], [72] or atlases [73]. However, deformable approaches [13], [74], [75], [76] or graph-based approaches [14] may handle the cartilage segmentation problem as accurately by using some contour or image dynamics such as curvature, intensities, or derivatives. But, for all approaches the initialization step of the segmentation method should be designed so that the automatic operation of the system is sustained. Consequently, some researchers have used shape-based methods to segment the knee bones with rigid shapes, and proposed local solutions to segment the cartilage compartments via individual or combined classification, deformable, or graph-based approaches [9], [10], [11], [16], [20], [22], [23]. Unlike such segmentation approaches, the focused classification-driven region-growing algorithm requires neither segmentation of bones nor determination of BCI, which makes it rather practical to apply.

Nonetheless, Folkesson et al. [15] did not clearly explain how the background voxels in the training MR images were handled in their work. Dam and Loog [30] noted their use of the original work by Folkesson et al., and that the original work combined two binary classifiers which used around 500,000 training voxels for background, 120,000 voxels for TC, and 300,000 voxels for FC. This indicates that the original work also

suffered from the abundance of MR image voxels, and somehow reduced their amount. Moreover, the classification-driven region-growing algorithm had the oversegmentation problem around the surfaces of cartilage compartments, which could not totally be solved even by a more localized implementation of the method by Dam et al. [12].

If all voxels in the training MR images are included into the training models, models become more general, but this can result in an infeasible segmentation problem especially for high-field MR images with a great deal of voxels, and systems with limited memory or processing power. Subsampling of the MR image voxels can cure this problem with the cost of loss of generality [12]. However, running effective techniques for selecting the voxels can preserve the segmentation accuracies of most of the works in the literature by enabling a trade-off between the oversegmentation and undersegmentation issues. Therefore, investigation of the effects of various subsampling techniques in segmentation accuracies, as in this study, is important to guide the researchers interested in MR image segmentation through classification, and we believe that our study makes an incremental contribution in this respect.

In the study described in this chapter, high-field MR images in the 3-D DESS standard obtained from the Osteoarthritis Initiative (OAI) database were processed to automatically segment the whole FC, LTC, MTC, and PC tissues of the osteoarthritic knee joints using a variation of a voxel-classification-driven region-growing algorithm [15] with sample-expand method [30]. In consideration of systems with limited resources concerning memory or processing power, the infeasibility of classification that depends on training models composed of millions of voxel samples with high dimensions was eliminated. This was achieved via reduction of the background voxels through Gaussian, uniform, vicinity-correlated (VC) sparse, or VC dense subsampling techniques, and determining a subset of significant features through feature selection. Four training models were generated by various subsampling techniques, and their effects on the final segmentation accuracies were investigated for cartilaginous compartments of interest in test image sequences.

This chapter is organized as follows. Subsection 4.1 clarifies the materials handled and methods implemented in realization of the training phase (Subsection 4.1.3) and the

testing phase (Subsection 4.1.4) of the automatic cartilage segmentation system. Subsection 4.2 elaborates on the subsampling techniques applied when generating the training models. Subsection 0 presents the experiments performed and the results obtained for the OAI data sets. Subsection 4.3.1 analyses computationally most intensive procedure of the system as well as segmentation durations.

4.1 Materials and Methods

Morphological analysis of cartilage for healthy populations may have significance for some studies, such as those targeting the determination of population statistics on cartilage measurements [8]. However, in clinical or surgical practice, it is more probable to encounter patients with frequent knee symptoms due to degenerated articular cartilage, which makes analysis of osteoarthritic knees in MR images crucial. Consequently, this study was conducted using MR images of knee joints that were categorically assessed as osteoarthritic with Kellgren and Lawrence (K-L) grade ≥ 2 but visually evaluated not to have large full-depth deterioration of the cartilage, especially in the FC and TC compartments. The latter condition was due to the use of one third of these MR images for training and to reflect the features of the cartilage voxels properly.

In total, 33 MR images of OAI [77] participants in the progression subcohort [78], which were scanned at baseline, and their corresponding data files of cartilage semi-manually segmented with EndPoint software were used in this study. Appendix A.1 presents further information on the subset of OAI data assessed by Imorphics and demographics of these 33 participants. 10 MR images were processed in training phase of the study, and 23 MR images were processed in testing phase. The original size of the image sequences was 384 × 384 × 160 with resolutions along the z, y, and x axes of $r_z = 0.36$, $r_y = 0.36$, and $r_x = 0.7$ mm, respectively. The labelling of dimensions is based on the reference frame of the MR scanner designated in Figure 3.4.

A block diagram of the implemented cartilage segmentation system for the training and testing phases is shown in Figure 4.1 in an integrated manner. The arrows, dashed blocks, and solid blocks in the chart indicate the course of data flow and system procedures for which the potential of a multi-core processor was exploited and was

not exploited. The green blocks represent offline procedures with output data that were recorded on a hard disk, and white blocks represent online procedures retrieving this recorded data from the hard disk on demand. Additionally, the training and testing procedures are separately depicted in Figure 4.2 and Figure 4.3 for further clarification of this chart. The following subsections elaborate on these procedures in an order that is close to the course of data flow.

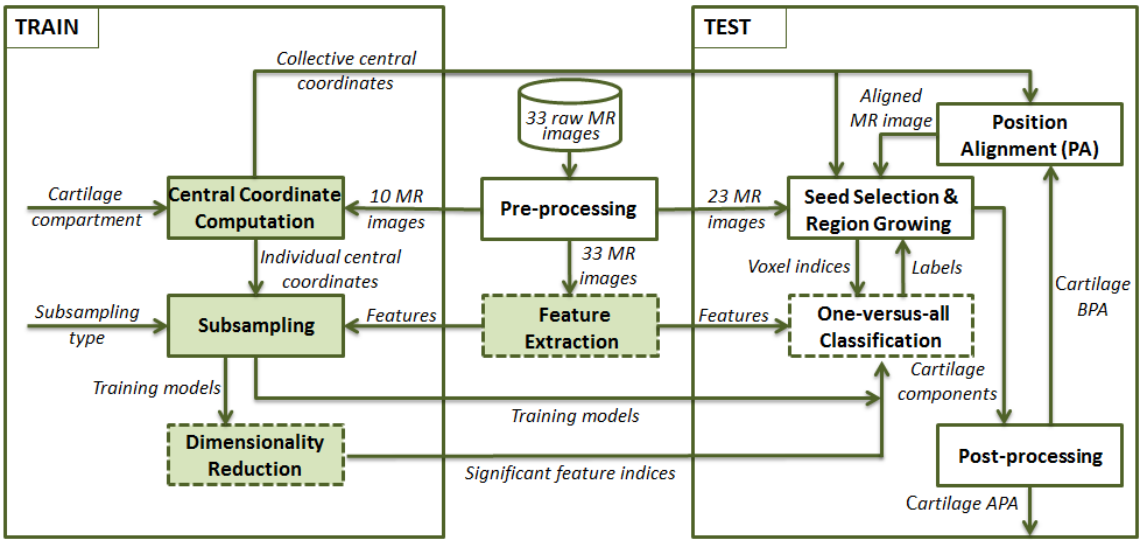

Figure 4.1 Block diagram of the implemented cartilage segmentation system for the training and testing phases.

4.1.1 Preprocessing

Initially, all MR images were cropped to a size of 280 × 280 × 143 both to reduce the burden of the feature extraction process and to remove noisy voxels near the image borders. The cropped region was determined using semi-manual segmentations of the cartilage compartments so that the information pertaining to any compartments in any MR images was retained. The next step was normalization of intensities of each MR image in between values of [0, 1]. Lastly, MR images of right knees were flipped along the x axis to relocate cartilage compartments to relatively consistent positions among all image sequences.

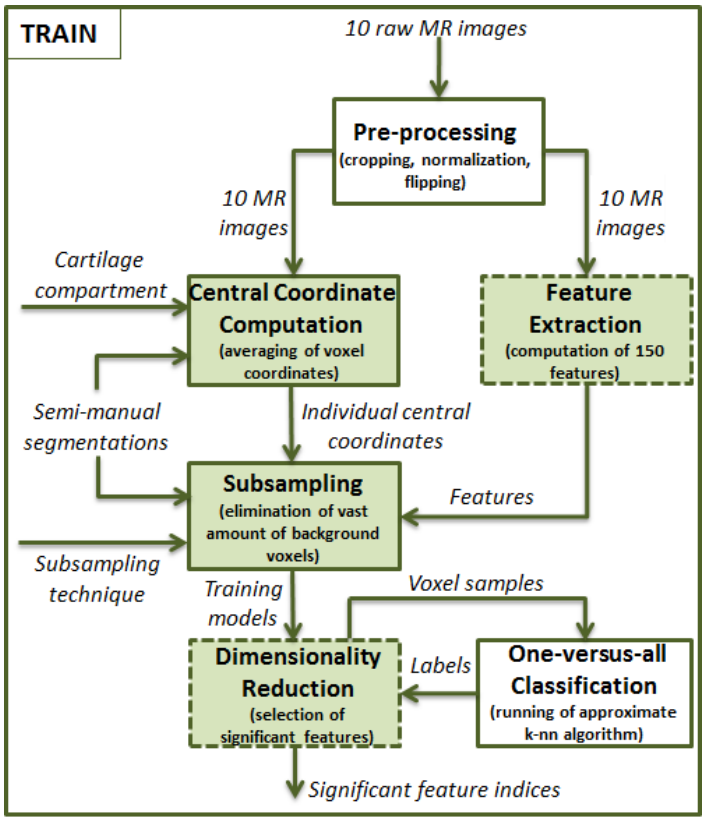

Figure 4.2 Detailed block diagram of the training phase.

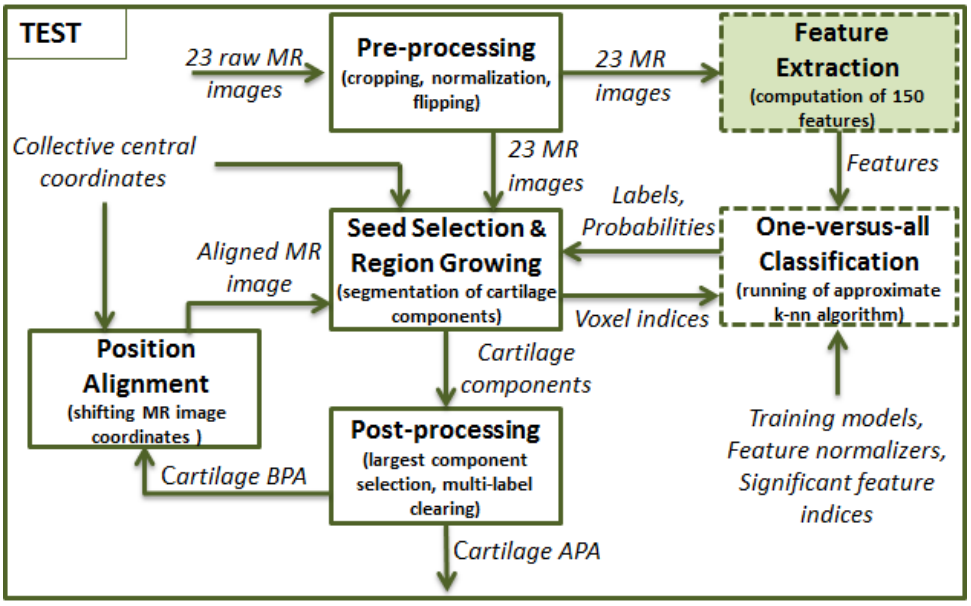

Figure 4.3 Detailed block diagram of the testing phase.

4.1.2 Feature Extraction

In total, 150 features were computed for each voxel of every MR image, which can be denoted as **I**, using three scales of the physical world as σ_i= {0.65 mm, 1.1 mm, 2.5

mm}. These scales were also found to be reasonable according to the means and standard deviations of the subcompartmental cartilage thicknesses of healthy and osteoarthritic populations measured by Williams et al. [8] based on manual segmentations of the cartilage in MR images. The features consisted of voxel coordinates $\boldsymbol{c} = (\mathrm{c}_z, \mathrm{c}_y, \mathrm{c}_x)$, smoothed intensities $\boldsymbol{I}^{\sigma_i}$; first-order derivatives $\boldsymbol{I}_x^{\sigma_i}$, $\boldsymbol{I}_y^{\sigma_i}$, and $\boldsymbol{I}_z^{\sigma_i}$; second-order derivatives $\boldsymbol{I}_{xx}^{\sigma_i}, \boldsymbol{I}_{xy}^{\sigma_i}, \boldsymbol{I}_{xz}^{\sigma_i}, \boldsymbol{I}_{yy}^{\sigma_i}, \boldsymbol{I}_{yz}^{\sigma_i}$, and $\boldsymbol{I}_{zz}^{\sigma_i}$; third-order derivatives $\boldsymbol{I}_{xxx}^{\sigma_i}, \boldsymbol{I}_{yyy}^{\sigma_i}$,and $\boldsymbol{I}_{zzz}^{\sigma_i}$; eigenvalues and eigenvectors of Hessian matrix $\boldsymbol{H}^{\sigma_i}$; and eigenvalues and eigenvectors of structure tensor matrix $\boldsymbol{ST}^{\sigma_o,\sigma_i}$.

The corresponding digital standard deviations on the axes for each value of scale σ_i were calculated as $(\sigma_z = \sigma_i/\mathrm{r}_z, \sigma_y = \sigma_i/\mathrm{r}_y, \sigma_x = \sigma_i/\mathrm{r}_x)$ depending on the spatial resolutions $(\mathrm{r}_z, \mathrm{r}_x, \mathrm{r}_y)$ of the image axes. Then, smoothed intensities of the voxels were found by convolution of the MR image with the 3-D Gaussian filter $\boldsymbol{G}^{\sigma_i}$, the values of which are computed according to a multivariate Gaussian function in (4.1), where **Σ** is a 3 × 3 covariance matrix with diagonal values of $(\sigma_z^2, \sigma_y^2, \sigma_x^2)$, and $\boldsymbol{v}$ is the vector of variables (v_z, v_y, v_x) indicating coordinates of the filter elements.

$$\boldsymbol{G}^{\sigma_i}(\boldsymbol{v}, \boldsymbol{\Sigma}) = \left(\sqrt{(2\pi)^3\,|\boldsymbol{\Sigma}|}\,\right)^{-1} \exp\left(-\frac{1}{2}\,\boldsymbol{v}\boldsymbol{\Sigma}^{-1}\boldsymbol{v}^T\right) \tag{4.1}$$

First, second, and third-order derivatives were computed by convolution of smoothed MR images $\boldsymbol{I}^{\sigma_i}$ with the Prewitt filters of related axes shown in Figure 4.4, consecutively when necessary. Eigenvalues and eigenvectors of $\boldsymbol{H}^{\sigma_i}$ and $\boldsymbol{ST}^{\sigma_o,\sigma_i}$ for each voxel were estimated by decomposition of the matrices given in equations (4.2) and (4.3), respectively. As a result of this decomposition, 12 features comprising 3 sorted eigenvalues and their corresponding eigenvectors each of length 3 were obtained. The scale σ_o for the structure tensor matrix determined the standard deviations of the 3-D Gaussian filter $\boldsymbol{G}^{\sigma_o}$ applied to the image sequences of multiplied first-order derivatives before the decomposition operation. Values of σ_o= {1.1 mm, 2.5 mm} led to six combinations of the (σ_o, σ_i) tuple.

Computational complexity was greatest for the features of eigenvalues and eigenvectors of the structure tensor matrix. Although such features could have been

computed for only a subset of voxels after subsampling (Subsection 4.1.3.2) on each training MR image, they were computed for all voxels both to enable regeneration of training models and feature visualization. On the other hand, computation of only the significant features selected (Subsection 4.1.3.3) sufficed for the test MR images.

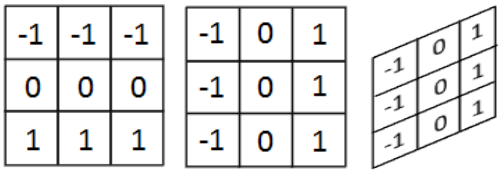

(a) (b) (c)

Figure 4.4 Prewitt filters used to compute the derivatives along the (a) z, (b) y, and (c) x axes.

$$\boldsymbol{H}^{\sigma_i} = \begin{bmatrix} \boldsymbol{I}_{xx}^{\sigma_i} & \boldsymbol{I}_{xy}^{\sigma_i} & \boldsymbol{I}_{xz}^{\sigma_i} \\ \boldsymbol{I}_{xy}^{\sigma_i} & \boldsymbol{I}_{yy}^{\sigma_i} & \boldsymbol{I}_{yz}^{\sigma_i} \\ \boldsymbol{I}_{xz}^{\sigma_i} & \boldsymbol{I}_{yz}^{\sigma_i} & \boldsymbol{I}_{zz}^{\sigma_i} \end{bmatrix} \tag{4.2}$$

$$\boldsymbol{ST}^{\sigma_i,\sigma_o} = \boldsymbol{G}^{\sigma_o} * \begin{bmatrix} \boldsymbol{I}_x^{\sigma_i}\boldsymbol{I}_x^{\sigma_i} & \boldsymbol{I}_x^{\sigma_i}\boldsymbol{I}_y^{\sigma_i} & \boldsymbol{I}_x^{\sigma_i}\boldsymbol{I}_z^{\sigma_i} \\ \boldsymbol{I}_x^{\sigma_i}\boldsymbol{I}_y^{\sigma_i} & \boldsymbol{I}_y^{\sigma_i}\boldsymbol{I}_y^{\sigma_i} & \boldsymbol{I}_y^{\sigma_i}\boldsymbol{I}_z^{\sigma_i} \\ \boldsymbol{I}_x^{\sigma_i}\boldsymbol{I}_z^{\sigma_i} & \boldsymbol{I}_y^{\sigma_i}\boldsymbol{I}_z^{\sigma_i} & \boldsymbol{I}_z^{\sigma_i}\boldsymbol{I}_z^{\sigma_i} \end{bmatrix} \tag{4.3}$$

All features of each training MR image were max-min normalized to be in between values [-1, 1] except position features that were normalized to be in between values [0, 4]. This was because they were selected as significant features, so position error during classification can be penalized a little bit more. The feature normalization parameters for every training image sequence were also stored for use during the automatic segmentation of voxels of test MR images.

4.1.3 Construction of Training Models

To construct the training models, using 10 MR images overall composed of approximately 110 million voxels with 150 features each leads to a system that cannot be feasibly realized in case of limited resources concerning memory or processing power. Even storage of such a large amount of data in memory of typical size is impossible, not to mention the overhead of constructing a parametric model of data or of dealing with the all of the data as the model. Consequently, abundance of the voxels

was eliminated for each MR image via uniform, Gaussian, VC sparse, or VC dense background subsampling techniques, and the high dimensionality of the voxel samples was reduced by feature selection to overcome this problem. Then, the training data sets decreased in size and dimension were directly treated as the models through a non-parametric one-versus-all classification approach enabling parallelization, which is further explained in Subsection 4.1.4.2.

4.1.3.1 Central Coordinate Computation

After preprocessing sequences of training images, central coordinates of each cartilage compartment were calculated by evaluating the training MR images both individually and collectively. To compute the individual central coordinate of a cartilage compartment, 3-D coordinates of the voxels within volume of the compartment, which was delineated by a trained segmenter beforehand, were averaged in the axes for a single training MR image. To compute the collective central coordinate of a cartilage compartment, the same averaging operation was performed by taking voxel coordinates of the compartment in all of 10 training MR images into consideration. Individual central coordinates of the compartments over MR images were useful in Gaussian subsampling of background voxels, and collective central coordinates were useful in seed selection and position alignment in test image sequences.

4.1.3.2 Subsampling

When constructing the training models of each cartilage compartment in each training MR image for one-versus-all classification of the cartilage voxels, all cartilage voxels of the related compartment were labelled as positive samples, whereas the rest were labelled as negative. Nevertheless, since the number of cartilage voxels in an MR image is much lower than the number of background voxels, all cartilage voxels were included in a training model whereas equal number of background voxels were selected via uniform, Gaussian, VC sparse, or VC dense background subsampling techniques. Hence computational infeasibility of the classification problem could be resolved substantially. The four background subsampling techniques enabled construction of four different training models for each cartilage compartment of each training MR image. The subsampling strategies of these techniques are separately

explained in Subsection 4.2, because the main contribution of this study is based on investigation of the subsampling techniques introduced.

4.1.3.3 Dimensionality Reduction

The dimension of voxel features was reduced from 150 to 18 for each cartilage compartment. This was done by comparing the features selected by a forward feature selection algorithm in Gaussian subsampled training models of 3 MR images. The algorithm ran separately for each of those MR images using 10-fold cross-validation of their training models and the classification procedure described in Subsection 4.1.4.2. Due to long response times of the classification algorithm for high dimensions, feature selection was forwardly run for only up to 20 features by treating all features individually.

Next, among the features selected in the training models, significant features for the respective cartilage compartment were identified as those that are exactly the same for at least 2 MR images, those differing only in scale for at least 2 MR images, and those highly discriminative for any of the 3 MR images, in order of decreasing priority. Table 4.1 lists the 18 significant features for each cartilaginous compartment of interest without indicating any priority of significance. Numbers at the lower right corner of the Hessian and structure tensor matrices refer to one of their 12 eigenvalue and eigenvector features in the order stated in Subsection 4.1.2. Figure 4.5 (a) through (d) visualize some significant features selected for FC, LTC, MTC, and PC, respectively. Because MTC and LTC were visible in only the first and second halves of the image sequences, (c) depicts slice number 50, while (a), (b), and (d) depict slice number 110 of the same MR image.

An exhaustive search could not be performed when selecting the features owing to computational constraints, but features found as significant were sufficiently effective in their corresponding classifiers of cartilage compartments. Furthermore, selecting features on the training models of other subsampling techniques did not affect the primarily identified significant features.

4.1.4 Automatic Segmentation

Segmentation of cartilage in test MR images involved a blind approach in a way that no prior information related to entries on the position of cartilage or manual interventions was assumed other than the information derived from the training data sets. To realize the automatic segmentation, the seed selection and position alignment procedures relied on the central coordinates of cartilage compartments, while the classification procedure relied on the training models of various subsampling techniques.

Table 4.1 Significant features selected for classification of the cartilaginous compartments of interest.

Compartment	Selected Features
FC	$c_z,\ c_y,\ c_x,\ I_z^{2.5}, I_y^{2.5},\ I_{zz}^{0.65}, I_{yy}^{0.65}, I_{zz}^{1.1},\ I_{yz}^{1.1},$ $I_{yy}^{1.1}, I_{xy}^{2.5}, I_{yyy}^{0.65}, I_{zzz}^{2.5}, H_1^{0.65}, H_1^{1.1},$ $ST_3^{2.5,0.65}, ST_4^{2.5,0.65}, ST_3^{2.5,1.1}$
LTC	$c_z,\ c_y,\ c_x,\ I_z^{2.5}, I_{zz}^{0.65},\ I_{yy}^{0.65}, I_{zz}^{1.1}, I_{zz}^{2.5}, I_{xy}^{2.5},$ $I_{xx}^{2.5}, I_{zzz}^{0.65}, I_{zzz}^{2.5}, H_1^{0.65}, H_1^{1.1}, ST_1^{1.1,1.1},$ $ST_2^{1.1,1.1}, ST_3^{2.5,0.65}, ST_3^{2.5,1.1}$
MTC	$c_z,\ c_y,\ c_x,\ I_z^{1.1},\ I_z^{2.5}, I_x^{2.5}, I_{zz}^{0.65}, I_{xz}^{0.65},$ $I_{zz}^{1.1}, I_{zz}^{2.5},\ I_{xz}^{2.5}, I_{zzz}^{0.65}, I_{zzz}^{2.5}, I_{xxx}^{2.5}, H_1^{0.65},$ $ST_3^{1.1,0.65}, ST_3^{2.5,0.65}, ST_3^{2.5,1.1}$
PC	$c_z,\ c_y,\ c_x,\ I_s^{0.65},\ I_z^{1.1}, I_y^{1.1}, I_y^{2.5},$ $I_{yy}^{0.65}, I_{xy}^{0.65}, I_{zz}^{1.1}, I_{yy}^{1.1}, I_{zz}^{2.5}, I_{xy}^{2.5},$ $I_{xxx}^{1.1}, I_{zzz}^{2.5}, I_{yyy}^{2.5}, H_1^{1.1},\ ST_1^{1.1,1.1}$

4.1.4.1 Seed Selection and Region-Growing

The classification-driven region-growing algorithm involved the sample-expand method, which enables efficient segmentation of objects of interest with large surface area-to-volume ratio [30]. The algorithm was initialized through determination of at least 100 seed points that belong to the cartilage compartment to be segmented. To achieve this, voxels were randomly chosen using a 3-D Gaussian image with the centre

shifted to the collective centre of the respective cartilage compartment in the entire training data sets as the weights. The chosen voxels were classified with respect to the corresponding training model of a subsampling technique. Then, the voxels classified as cartilage became the seed points of the region-growing algorithm and were grown iteratively by integrating them with the cartilage voxels in their 26-neighbourhood until all of the neighbours were background. During the region-growing procedure, classification probabilities of the voxels were also maintained for each classifier to resolve the issue of multi-labelled voxels in the post-processing procedure.

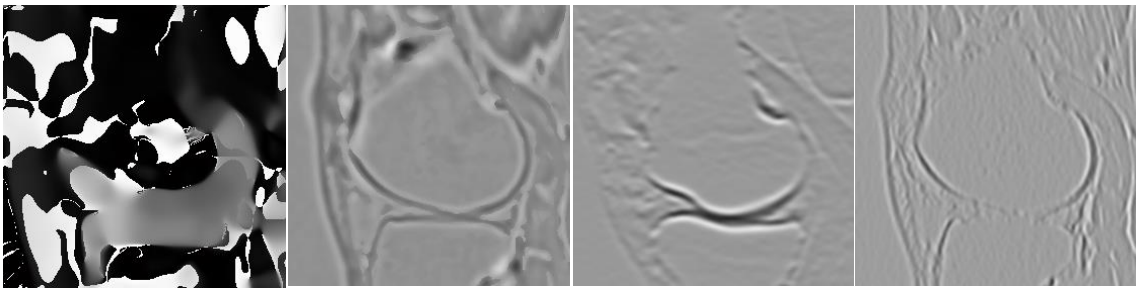

(a) (b) (c) (d)

Figure 4.5 (a) $\mathrm{ST}_4^{2.5,0.65}$, (b) $\mathrm{H}_1^{1.1}$, (c) $\mathrm{I}_{\mathrm{zz}}^{1.1}$, and (d) $\mathrm{I}_{\mathrm{yy}}^{0.65}$ in 50th (c) and 110th (a, b, d) slices of the same MR image.

4.1.4.2 One-Versus-All Classification

The four cartilage compartments of interest have relative positional and morphological differences. However, they have the same structural components and resembling local morphologies, making their appearance similar in MR images. Hence, distinguishing all of these compartments at once with a multi-class classifier was considered to be more prone to failure than distinguishing them separately with one-versus-all classifiers each trained for a cartilage compartment. Four classifiers of FC-versus-all, LTC-versus-all, MTC-versus-all, and PC-versus-all were run to segment the respective cartilage compartment using the selected features of the training model generated by one of the subsampling techniques. The classifiers depended on the approximate k-NN algorithm in the statistical learning toolbox [79] implemented by Mount and Arya [80], [81]. For a training data set of size n and dimension d, the approximate k-NN algorithm constructs a data structure of size $O(dn)$ in $O(dn\log n))$ time. For any query sample, the approximate k-NN are determined with a relative error bound ϵ from the exact k-

NN in $O\big((c_{d,\epsilon} + kd)\ \log n)\big)$ time, where $c_{d,\epsilon}$ is a constant that depends on parameters d and ϵ. These parameters were given as 100 and 3 in this study so that the approximate 100-NN of the queried samples, which had error bound of 3 from the exact 100-NN, were retrieved [82].

Even after subsampling, roughly 300 thousand, 100 thousand, and 70 thousand data samples were available for the training models of FC, TC, and PC, respectively, for a training MR image. When 10 MR images were processed for the training phase, the computational or memory-related capabilities of a resource-limited system would be overwhelmed if a predictive model out of so much data via parametric approaches was built or if all of the data was handled for every query sample in a test image sequence via standard nonparametric approaches. The approximate k-NN algorithm performs quite efficiently on data sets composed of hundreds of thousand samples with dimensions as high as 20 [80]. Consequently, parallelization of the classification procedure on multi-core systems was considered by assigning to each core the task of classification of query samples depending on the training model and feature normalization parameters of only a single MR image. Then, 100 approximate neighbours of the query samples were identified in each task, and the nearest 100 among one thousand neighbours were later determined again. If at least 90% of these neighbours were cartilage of a compartment, then the query samples were labelled as cartilage of that compartment. Otherwise, they were labelled as background. This threshold is indicated by $t_c = 0.9$ and was essential to remove most of the oversegmented fragments of the main cartilage component. Its value was set empirically to maximize the DSC measure of automatic segmentations on a subset of 5 test MR images.

4.1.4.3 Post-Processing

The result of the classification-driven region-growing algorithm was a number of components that represent a cartilage compartment. However, small components were generally false positives, while large components were true positives. Therefore, a connected component-finding algorithm was run, and size of each component was estimated by voxel counting. The component with the greatest size was accepted as

the true segmentation result of the compartment, since this was a relatively robust approach.

When all cartilaginous compartments were segmented, multi-labelled voxels were assigned to a single label based on their probabilities of classification for different compartments. For this purpose, the intersection of the segmented tuples of LTC-MTC, FC-LTC, FC-MTC, FC-PC, LTC-PC, and MTC-PC were investigated in order, and multi-labels were cleared. This operation required the connected component-finding algorithm to be run a second time separately on the segmentation result of each cartilage compartment to remove small isolated components and obtain the greatest component as the final segmentation result.

4.1.4.4 Position Alignment

Positional differences of the knee joints among MR images could affect the accuracies of segmentation negatively since features related to position were significant for most of the classifiers. To tolerate these differences, test MR images can be shifted so that the cartilage compartment to be segmented becomes closer to its counterparts in the training data sets. The amount of shift for each cartilage compartment in a testing image sequence was computed by subtracting the central coordinate of the automatically segmented region of cartilage before position alignment (BPA) and the collective central coordinate of the corresponding cartilage compartment in the training MR images. Because feature extraction procedure was performed offline in this study, position alignment was realized through only relocation of the features other than the position according to the shifting amount instead of shifting the test image sequence itself and computing the significant features as required. Subsequently, the procedures of Subsection 4.1.4.1 to Subsection 4.1.4.3 were repeated, and automatic segmentation of cartilage after position alignment (APA) was achieved.

4.2 Subsampling Techniques

The principle of the subsampling procedure described in Subsection 4.1.3.2 is to select a reasonable subset of background voxels in each training MR image for each

compartment to solve the infeasibility problem of classification. Although partial representation of large amount of background voxels may affect the segmentation accuracies negatively, effective selection of these voxels rather than performing only a random selection can compensate this.

In this study, first of all, uniform subsampling (Subsection 0) of background voxels was implemented for construction of the training models, but this technique did not result in satisfactorily high segmentation accuracies as expected, especially for smaller compartments such as LTC, MTC, and PC. Then, Gaussian subsampling (Subsection 0) of the background voxels was realized, which yielded better segmentation accuracies yet poorer representations for the compartments with highly curved and large shapes such as FC. Therefore, a cartilage vicinity-correlated subsampling technique (Subsection 0) was designed to generate proper representations by flexibly adapting to the shape of the object of interest, and was used to derive VC sparse and VC dense representations for each compartment in the training MR images.

Each subsampling technique adopted a different strategy to determine the selection weights of the background voxels, and then similarly performed a random selection of these voxels depending on the weights. The pseudo-code of the generic algorithm that was run to apply one of the subsampling techniques is as in Figure 4.6. This algorithm common for all techniques first determines the background volume ($\mathbf{V}_{bg}$) that surrounds a cartilage compartment ($\mathbf{V}_{obj}$), and the number of voxels in this compartment (n_{obj}). Second, the selection weights of the background voxels ($\mathbf{W}$) are computed depending on the choice of subsampling technique. Then, n_{obj} unique voxels with the label of 1 in $\mathbf{V}_{bg}$ are randomly selected among the background voxels using $\mathbf{W}$. Finally, the algorithm integrates the cartilage voxel coordinates $\mathbf{C}_{obj}$ and subsampled background voxel coordinates $\mathbf{C}_{bg}$ as well as the corresponding labels of these voxels to generate the training model of the cartilage compartment for a training MR image and a subsampling technique.

Subsampling strategies of the techniques are demonstrated in Figure 4.7 through slicewise visualization of some voxels included in the models of FC for a training image sequence in the first row, and 3-D visualization of all voxels included in the FC training

models of a training MR image in the second row. The voxels of FC compartment are depicted in red, as background voxels are in blue in this figure.

Data: $\mathbf{size}_{MR}$: *size of the training MR image in (z, y, x) axes;*
$\mathbf{V}_{obj}$: *Volume in which object of interest voxels in the training MR image are labelled as 1, and background voxels are labelled as 0;*
$\mathbf{C}_{obj}$: *(z, y, x) coordinates of the object of interest voxels;*
technique: *choice of subsampling technique*
Result: $\mathbf{C}_{train}$: Coordinates of the voxels selected for the training model of the object of interest in the training MR image;
labels: labels of the voxels selected for the training model

1 n_{obj} = *count*($\mathbf{V}_{obj}$ == 1); // number of object voxels
2 /* Negate the volume that highlights object of interest */
3 $\mathbf{V}_{bg}$ = ¬$\mathbf{V}_{obj}$; // volume that highlights background
4 n_{bg} = *count*($\mathbf{V}_{bg}$ == 1); // number of background voxels
5 $\mathbf{C}_{bg}$ = ∅; // (z,y,x) coordinates of subsampled background voxels
6 i = 0; // counter
7 /* Compute selection weights W of the background voxels depending on technique */
8 **if** *technique=='Uniform'* **then**
9 **W** = *UniformWeights*($\mathbf{size}_{MR}$, $\mathbf{V}_{bg}$, $\mathbf{n}_{bg}$);
10 **else if** *technique=='Gaussian'* **then**
11 **W** = *GaussianWeights*($\mathbf{size}_{MR}$, $\mathbf{C}_{obj}$, $\mathbf{n}_{obj}$, $\mathbf{V}_{bg}$);
12 **else if** *technique=='VC sparse'* **then**
13 **W** = *VicinityCorrelatedWeights*($\mathbf{size}_{MR}$, $\mathbf{V}_{obj}$, $\mathbf{V}_{bg}$, 0.9);
14 **else if** *technique=='VC dense'* **then**
15 **W** = *VicinityCorrelatedWeights*($\mathbf{size}_{MR}$, $\mathbf{V}_{obj}$, $\mathbf{V}_{bg}$, 0.67);
16 /* Iterate until nobj background voxels are selected */
17 **while** $i \neq n_{obj}$ **do**
18 /* Select randomly a voxel in $\mathbf{V}_{bg}$ based on weights **W** */
19 $\mathbf{c}_{voxel}$ = *randomSelect*($\mathbf{V}_{bg}$, **W**); // selected voxel coordinate
20 /*If the voxel is not already selected store its coordinate*/
21 **if** $\mathbf{c}_{voxel} \notin \mathbf{C}_{bg}$ **then**
22 $\mathbf{C}_{bg}$ = $\mathbf{C}_{bg}$ ∪$\mathbf{c}_{voxel}$;
23 i = i + 1;
24 $\mathbf{C}_{train}$ = $\mathbf{C}_{obj}$ ∪ $\mathbf{C}_{bg}$;
25 /* Merge label sequences of n_{obj} 1's and n_{bg} 0's*/
26 **labels** = *merge*(*sequence*(n_{obj} , 1); *sequence* (n_{bg}, 0));

Figure 4.6 The generic algorithm: Subsample.

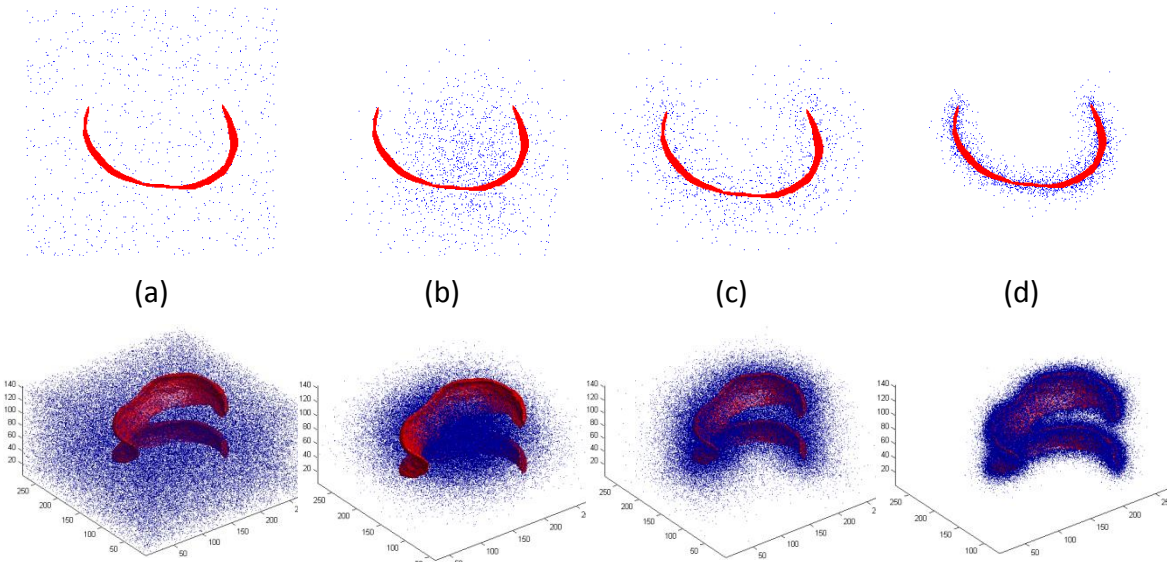

(a) (b) (c) (d)

(e) (f) (g) (h)

Figure 4.7 Voxels of FC models subsampled in a slice (first row) and in all slices (second row) of a training MR image according to (a, e) uniform, (b, f) Gaussian, (c, g) VC sparse, and (d, h) VC dense subsampling techniques.

4.2.1 Uniform Subsampling

Uniform subsampling is the simplest technique, since it used uniform weights during random selection of the background voxels. As Figure 4.7 (a) and (e) show, subsampled background voxels are widely distributed throughout the MR image with uniform subsampling. The algorithm in Figure 4.8, which is called within the generic algorithm in Figure 4.6, presents the pseudo-code of the weight generation process of this subsampling technique for the background voxels.

Data: $\mathbf{size}_{MR}$, $\mathbf{V}_{bg}$, n_{bg}
Result: W
/* A sequence of uniform weights of the same size as the MR image */
$\mathbf{W}$ = *sequence*($\mathbf{size}_{MR}$, 1/ n_{bg});
/* Assign uniform weights to voxels labelled as 1 in Vbg */
$\mathbf{W} = \mathbf{V}_{bg} \boxdot \mathbf{W}$; // element-wise product

Figure 4.8 Algorithm: Uniform weights.

A training model generated with uniform subsampling technique is strong to represent the background voxels in the entirety of MR image. However, it is weak to represent the background voxels in a localized sub-volume of the same MR image. Therefore,

representation of surrounding background voxels of especially small objects of interest in an MR image is insufficient with this technique.

4.2.2 Gaussian Subsampling

Gaussian subsampling technique weighted background voxels according to the intensities of a 3-D Gaussian image, which has the same size as the MR images and a centre shifted to the centre of the cartilage compartment of interest. The weight generation algorithm of this technique is pseudo-coded in Figure 4.9.

Data: $\mathbf{size}_{MR}$, $\mathbf{C}_{obj}$, n_{obj}, $\mathbf{V}_{bg}$
Result: W
/*Find (z, y, x) central coordinate of the object of interest*/
$\mathbf{centre}_{obj} = \text{sum}(\mathbf{C}_{obj})/n_{obj}$;
/* Generate a 3-D Gaussian image with size of sizeMR and standard deviation of $\text{size}_{MR}/6$ */
Gauss3D = *generate3DGauss*($\mathbf{size}_{MR}$, $\mathbf{size}_{MR}/6$);
/* Compute the amount of shift to carry the centre of 3-D Gaussian image to the centre of object */
$\mathbf{centre}_{Gauss} = \mathbf{size}_{MR}/2$;
shiftAmount = $\mathbf{centre}_{obj}$ - $\mathbf{centre}_{Gauss}$;
/* Translate 3-D Gaussian image by the shift amount */
$\mathbf{Gauss3D}_{shifted}$ = *translate*(**Gauss3D**, **shiftAmount**);
/* Assign Gaussian weights to voxels labelled as 1 in V_{bg} */
$\mathbf{W} = \mathbf{V}_{bg} \boxdot \mathbf{Gauss3D}_{shifted}$; // element-wise product

Figure 4.9 Algorithm: Gaussian weights.

Gaussian subsampling samples in a more localized volume in comparison to uniform subsampling so can generate better representations for objects that can be fully bounded by the constructed Gaussian sphere. However, it can fail to represent the objects with large and curved shapes properly. This problem is well-defined in Figure 4.7 (b) and (f) for FC compartment. Central coordinate of FC compartment do not exactly coincide with the compartment itself due to curved shape of FC. In addition to this, FC is the largest compartment of all, so the sphere in 3-D Gaussian image cannot envelope this compartment. Consequently, the background voxels near central coordinate of FC are frequently selected, whereas those distant from the centre are rarely selected. Although modifying the values of the covariance matrix of the Gaussian function to adjust the shape of Gaussian according to the shape of the object

of interest as much as possible might mitigate this problem, a more flexible solution is required as presented in the next subsection.

4.2.3 Vicinity-Correlated Subsampling

A subsampling approach that can be conveniently adaptable for objects with any shape and size is necessary for generation of effective representations, and vicinity-correlated subsampling was designed for this purpose. The background voxel-weighting algorithm of vicinity-correlated subsampling is presented in Figure 4.10, which is the basis of both VC sparse and VC dense subsampling techniques.

Data: $\mathbf{size}_{MR}$, $\mathbf{V}_{obj}$, $\mathbf{V}_{bg}$, sparseness
Result: W
W = *sequence*(**size**$_{MR}$, 0); // weights matrix of zeroes
sphere = *prepareSphere*(5); // 3-D sphere with 5-pixel diameter
$\mathbf{V}_{current} = \mathbf{V}_{obj}$;
$\mathbf{C}_{dilated}$ = *sequence*(3, 0); // dummy initialization with (0,0,0)
$weight_{current}$ = 100;
/* Dilate $V_{current}$ until it covers the entire MR image */
while ¬ ($\mathbf{C}_{dilated}$ == ∅) **do**
/* Morphologically dilate $V_{current}$ with sphere */
$\mathbf{V}_{dilated}$ = *dilate*($\mathbf{V}_{current}$, **sphere**);
/* Find dilated portion of $V_{dilated}$ */
$\mathbf{V}_{difference} = \mathbf{V}_{dilated} - \mathbf{V}_{current}$; // element-wise subtract
/* Find coordinates of voxels with value 1 in $V_{difference}$ */
$\mathbf{C}_{dilated}$ = *coordinatesOf*($\mathbf{V}_{difference}$ == 1);
if ¬ ($\mathbf{C}_{dilated}$ == ∅) **then**
/* Assign $weight_{current}$ to $\mathbf{C}_{dilated}$ coordinates in **W** */
$\mathbf{W}(\mathbf{C}_{dilated}) = weight_{current}$;
$\mathbf{V}_{current} = \mathbf{V}_{dilated}$; // update $\mathbf{V}_{current}$
/* Modify $weight_{current}$ using sparseness */
$weight_{current} = weight_{current}$ *sparseness;
/* Normalize **W** so that its values add up to 1 */
W =**W**/*sum*(**W**);

Figure 4.10 Algorithm: Vicinity-correlated weights.

To weight the background voxels, VC subsampling iteratively dilates the volume of the cartilage compartment by a spherical morphological operator with a diameter of 5

voxels until the full size of the MR image was reached, and assigns each dilated portion to a weight that constantly decreases with the number of iterations. The difference between the VC sparse and VC dense subsampling techniques is related to the rate of change of these assigned weights. As the lines 13 and 15 of the algorithm in Figure 4.6 define, sparse and dense techniques apply decreases of 10% and 33% in the weight of the previous iteration, respectively, through the *sparseness* parameter of the algorithm in Figure 4.10. Figure 4.7 (g) and (h) show how the background volume around FC can be represented as intended with vicinity-correlated subsampling approach. Background voxels that surround FC are selected within a wider volume for VC sparse subsampling, and within a narrower volume for VC dense subsampling.

4.3 Experimental Results

The automatic segmentation results of FC, LTC, MTC, and PC for 23 test MR images were validated against their reference semi-manual segmentations by computing the measures of DSC, sensitivity, and specificity according to equations (1.1), (1.2), and (1.3). Table 4.2 presents the means and standard deviations of these measures for each compartment of cartilage in all test image sequences before and after the enhancement of position alignment for the four different training models. The results demonstrate that uniform subsampling enabled the highest sensitivity values when VC dense subsampling produced the highest specificity values for all cartilage compartments. Most of the best DSC values were observed in the case of VC sparse subsampling, which had relatively balanced sensitivity and specificity values. The reasons for these results can be clarified through the classification trade-off between background and cartilage voxels for the various subsampling techniques. The degree of separability of the classifier affects the accuracy of segmentation now that there is no other restriction on termination of the growing cartilage volume other than the neighbouring voxels classified as background in this segmentation approach.

When uniform subsampling collected excessively distributed background samples for the training models, the representation of background samples was weaker in the vicinity of cartilage. Thus, there was oversegmentation of the respective cartilage compartments combined with other similar structures. This resulted in maximization

of sensitivity and minimization of specificity measures. The situation was reversed when VC dense subsampling intensely collected background samples near cartilage. Then, the bias toward strong representation of those background samples caused undersegmentation of the cartilage. However, it should be noted that augmentation of DSC measures could be possible for these two techniques if the classification threshold t_c is assigned proper values so that $t_c > 0.9$ for uniform subsampling and $t_c < 0.9$ for VC dense subsampling. But even then the DSC measures for VC sparse subsampling with $t_c = 0.9$ remained optimal. Table 4.3 indicates this effect of t_c on mean DSC measures when differently subsampled training models were used.

Table 4.2 Means and standard deviations (Std.) of DSC, sensitivity (Sens.), and specificity (Spec.) measures of the automatically segmented cartilaginous tissues in the knee joint with respect to their manual segmentations before and after the enhancement of position alignment for the training models generated by different subsampling techniques.

Cartilage Compartment		**FC**		**TC**		**LTC**		**MTC**		**PC**		**Total**	
Sampling	**Measure (%)**	BPA	APA	BPA	APA	BPA	APA	BPA	APA	BPA	APA	BPA	APA
Uniform	DSC Mean	79.51	80.59	69.10	66.49	69.02	65.89	69.25	67.00	56.72	57.31	74.70	74.76
	DSC Std.	4.00	2.90	3.91	4.93	6.43	7.02	4.71	5.26	13.33	13.24	3.14	4.01
	Sens. Mean	**85.98**	**90.69**	**94.90**	**97.82**	**94.24**	**98.55**	**95.64**	**96.91**	**90.08**	**92.68**	**90.61**	**94.86**
	Sens. Std.	9.51	4.23	5.80	1.48	8.81	1.12	4.33	2.41	10.85	6.71	7.13	2.63
	Spec. Mean	99.65	99.59	99.66	99.58	99.83	99.78	99.83	99.81	99.68	99.67	99.01	98.87
	Spec. Std.	0.09	0.10	0.09	0.08	0.06	0.04	0.05	0.05	0.13	0.13	0.26	0.24
Gaussian	DSC Mean	79.28	80.50	80.48	82.04	80.75	83.17	**79.89**	80.65	**66.16**	71.03	**79.10**	81.03
	DSC Std.	3.67	3.07	3.82	3.23	6.38	4.72	3.49	2.72	12.41	8.93	3.61	2.63
	Sens. Mean	82.85	87.47	85.82	90.54	85.80	92.76	85.94	88.30	70.84	76.45	83.08	88.08
	Sens. Std.	8.18	4.62	7.94	3.33	11.83	3.13	6.40	4.89	15.12	9.88	7.86	3.68
	Spec. Mean	99.69	99.64	99.88	99.87	99.95	99.94	99.94	99.94	99.90	99.91	99.49	99.44
	Spec. Std.	0.10	0.11	0.04	0.03	0.02	0.02	0.02	0.02	0.04	0.04	0.14	0.14
VC Sparse	DSC Mean	**79.37**	**82.60**	**80.71**	**83.08**	**81.37**	**84.57**	79.69	**81.28**	66.01	**72.60**	78.71	**81.93**
	DSC Std.	5.79	3.55	4.46	2.96	6.55	3.71	4.33	3.33	13.85	8.53	5.35	2.88
	Sens. Mean	74.45	79.89	78.66	84.00	79.36	86.87	78.07	81.10	63.18	71.50	74.47	80.12
	Sens. Std.	9.83	5.86	7.80	4.36	11.23	4.31	7.70	6.34	15.76	9.60	8.83	4.46
	Spec. Mean	99.85	99.84	99.93	99.92	99.97	99.96	99.96	99.96	99.94	99.94	99.73	99.71
	Spec. Std.	0.05	0.05	0.02	0.02	0.01	0.02	0.02	0.01	0.03	0.03	0.07	0.07
VC Dense	DSC Mean	74.24	76.87	72.50	76.55	74.26	79.43	70.26	73.17	59.20	66.48	72.41	75.75
	DSC Std.	5.82	4.80	5.57	3.94	7.48	3.98	6.09	5.44	14.58	8.68	5.44	3.84
	Sens. Mean	63.00	66.51	59.94	65.56	62.34	69.79	57.55	61.19	48.07	56.19	60.55	65.06
	Sens. Std.	8.13	6.60	7.36	5.34	10.42	6.13	7.98	7.33	14.19	9.28	7.01	4.94
	Spec. Mean	**99.93**	**99.93**	**99.98**	**99.98**	**99.99**	**99.99**	**99.99**	**99.99**	**99.97**	**99.97**	**99.88**	**99.88**
	Spec. Std.	0.03	0.03	0.01	0.01	0.01	0.01	0.01	0.01	0.02	0.02	0.04	0.04

The training models of the VC sparse subsampling technique enabled an effective representation of the voxels in training data sets. Consequently, they resulted in the highest DSC measures especially APA, and resolved both problems of oversegmentation and undersegmentation to some extent. This implies that the VC sparse subsampling technique can be appropriate for similar classification-based segmentation approaches both to reduce the computational complexity of handling all voxel samples of an MR image and to accomplish robust delineation of an object of interest.

Table 4.3 The effect of t_c on the mean DSC APA (%) for each compartmental training model of the subsampling techniques in a subset of 5 testing MR images by setting the parameters of k and ϵ to 100 and 2, respectively.

Subsampling	$\mathbf{t_c}$	**FC**	**LTC**	**MTC**	**PC**
Uniform	0.95	**82.60**	**67.82**	**74.61**	**66.84**
	0.9	80.12	61.02	69.59	59.13
	0.7	70.58	48.04	55.74	43.50
	0.5	60.74	40.65	46.95	32.97
Gaussian	0.95	**81.25**	**81.78**	**81.31**	**71.37**
	0.9	80.00	79.34	80.98	69.44
	0.7	72.46	68.26	74.60	52.28
	0.5	65.29	59.23	66.98	38.84
VC sparse	0.95	79.95	81.25	78.03	69.32
	0.9	**83.12**	**82.22**	**81.69**	**72.09**
	0.7	81.34	74.76	78.67	66.71
	0.5	76.10	67.14	73.56	57.74
VC dense	0.95	72.10	72.14	66.24	56.09
	0.9	77.69	77.89	73.14	**64.91**
	0.7	**82.92**	**81.93**	**81.43**	51.86
	0.5	78.78	73.54	80.45	16.23

Superiority of the DSC measures APA for VC sparse subsampling technique was also indicated with paired t-tests performed at 5% significance level. As shown in Table 4.4, compartmental DSC measures APA for VC sparse are statistically significantly better than DSC measures BPA for VC sparse, and DSC measures BPA or APA for the other techniques. However, the difference of DSC measures APA for Gaussian subsampling technique in segmentation of MTC and PC were insignificant, which means that Gaussian subsampling can approximate to VC sparse subsampling for such small and ellipsoid structures.

Figure 4.11 shows the plots of the individual DSC measures of the segmented compartments in each test MR image BPA and APA for the subsampling techniques.

The information related to DSC means and standard deviations in Table 4.2 was overlaid on the plots. The blue and red dots point out individual DSC measures BPA and APA, the blue and red solid lines connect the mean DSC measures BPA and APA, and dashed blue and red lines parallel to the horizontal axis designate mean ± standard deviation BPA and APA, respectively. The position alignment procedure improved the average DSC for all compartments of cartilage, with the greatest improvement for PC. The only exception was tibial compartments for the training models of uniform subsampling. These compartments are smaller volumes so closely positioned to each other and FC that position alignment increased false positive rate more than increasing true positive rate due to random subsampling of background. The poorer DSC values and larger standard deviations for PC revealed in Table 4.2 indicate relative inadequacy of PC-versus-all classifier. This may be due to severe osteoarthritic deteriorations of cartilage for this compartment or similarity of the significant features of PC to the corresponding features of other nearby anatomical structures such as synovial fluid.

Table 4.4 Statistical significance of compartmental DSC measures APA for VC sparse subsampling technique. NS denotes statistically insignificance, when S denotes statistically significance of the measures.

Significance	**Uniform**		**Gaussian**		**VC Sparse**		**VC Dense**	
	BPA	APA	BPA	APA	BPA	APA	BPA	APA
FC	S	S	S	S	S	__	S	S
LTC	S	S	S	S	S	__	S	S
MTC	S	S	S	NS	S	__	S	S
PC	S	S	S	NS	S	__	S	S

Figure 4.12 presents the 3-D views of semi-manually and automatically segmented compartments of interest for one of the test MR images. The system again achieved highest DSC measures when the training models of the VC sparse subsampling were used for this MR image, and these measures were 85%, 82%, 83%, and 82% for FC, LTC, MTC, and PC, respectively.

The principal problems encountered during experimentation of the automatic segmentation system were solved as follows. Because some MR images were composed of a wide range of intensities due to noise, especially near the borders of the images, such images had low inter-tissue contrast after normalization. Therefore,

use of un-cropped full MR images prevented the system from distinguishing between the cartilage regions and background for such images. This problem was eliminated by cropping the MR images. Another problem was related to accepting the largest component as the segmentation result of a cartilage compartment in the post-processing procedure. For instance, when a cartilage compartment was detected in the form of several connected components due to worn-out regions of the cartilage, the largest component was only a partial representation of the whole compartment. In another instance, when some misclassified large components were grown, the truly classified cartilage component was totally eliminated. However, these difficulties were mostly overcome by optimization of the system parameters.

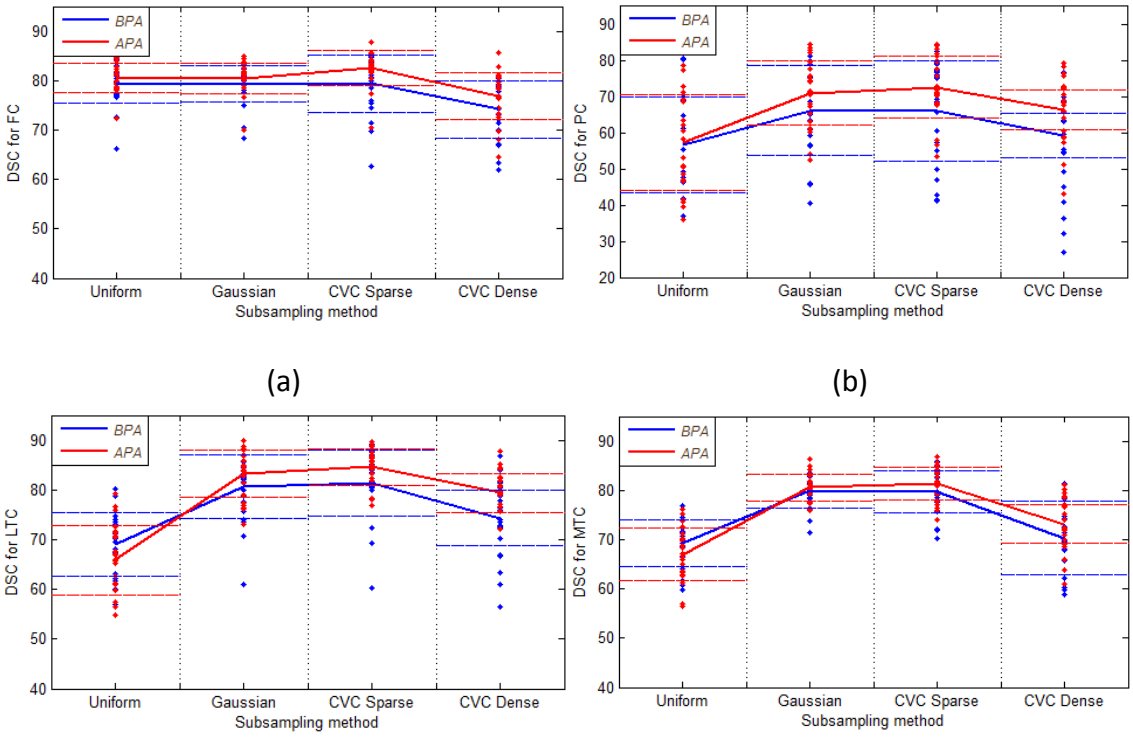

Figure 4.11 Plots of the individual percentage DSC measures for the cartilage compartments in each test MR image. The information related to DSC means and standard deviations in Table 4.2 is overlaid on the plots.

Some other observations emerged from sub-experiments are that an increase in the number of training MR images affected DSC measure positively, random subsampling of training models to improve system performance resulted in lower DSC values, and adding more features for the training models did not contribute to average segmentation accuracies. Furthermore, halving the MR images in slices in order to

reduce the computational complexity resulted in significant fall in segmentation accuracies as presented in Table 4.5 due to rather thin morphology of the cartilage. Figure 4.13 demonstrates the inadequacy of the automatic segmentations in halved MR images for one of the testing MR images with the larger tears in worn-out regions of the cartilage and greater volumes of oversegmented protrusions.

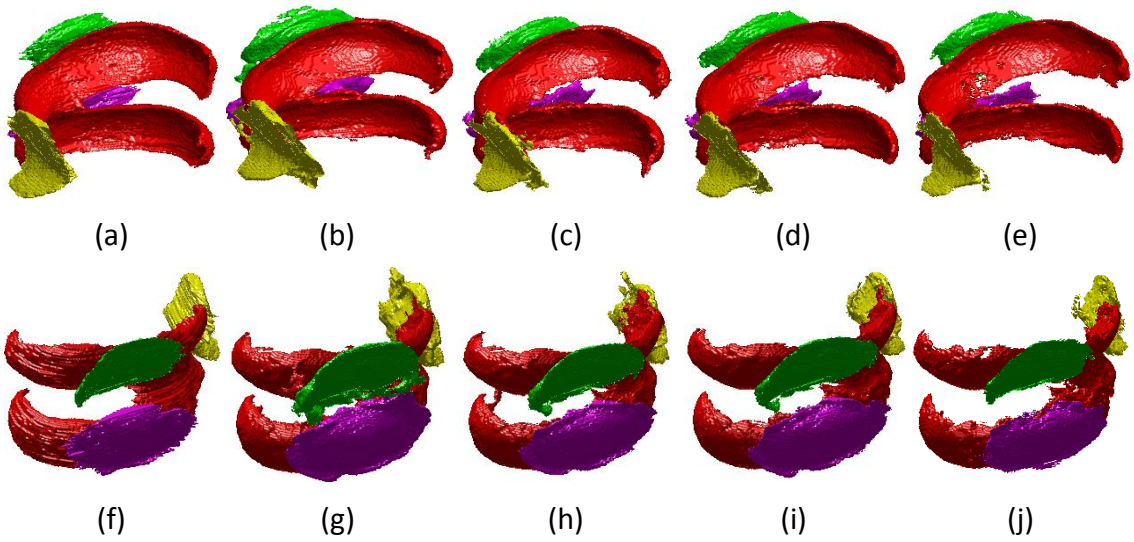

Figure 4.12 Superior (first row) and inferior (second row) 3-D views of cartilage compartments, which were manually segmented (a, f) and automatically segmented based on the training models of uniform (b, g), Gaussian (c, h), VC sparse (d, i), and VC dense (e, j) subsampling techniques, for one of the test MR images.

Table 4.5 The effect of halving the MR images slicewise on the mean DSC (%) measures and segmentation durations for each compartmental training model of the subsampling techniques in a subset of 5 testing MR images by setting the parameters of $k, \epsilon,$ and t_c to $100, 2,$ and 0.9, respectively.

Subsampling	measure	FC	LTC	MTC	PC
Uniform	DSC_BPA	64.18	39.45	48.05	39.41
	DSC_APA	63.49	37.97	47.63	39.35
	Duration_APA	20.66	2.26	1.87	3.01
Gaussian	DSC_BPA	63.81	54.80	61.94	42.62
	DSC_APA	63.24	52.34	62.69	**44.13**
	Duration_APA	18.76	1.98	1.82	2.39
VC sparse	DSC_BPA	72.65	**56.62**	63.31	41.50
	DSC_APA	73.28	56.45	**65.56**	41.03
	Duration_APA	13.43	1.72	1.51	2.46
VC dense	DSC_BPA	**74.21**	54.30	62.18	37.93
	DSC_APA	73.43	50.93	62.89	39.54
	Duration_APA	16.05	2.19	1.68	2.76

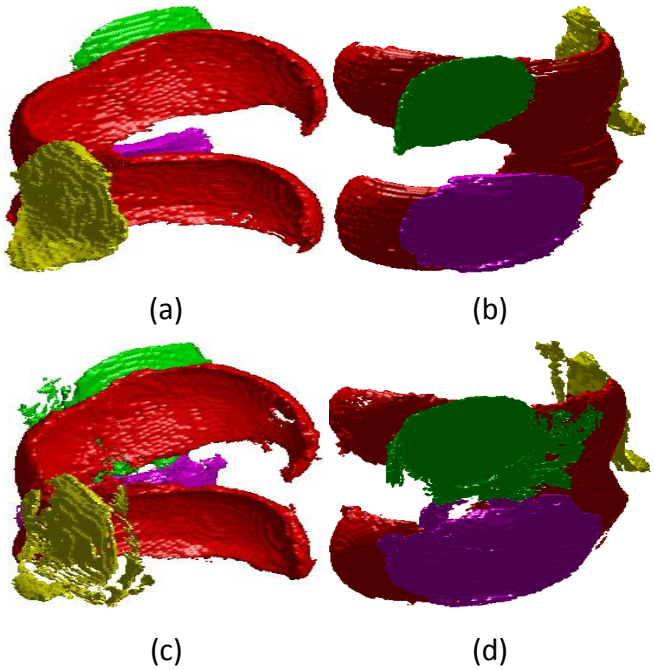

(a) (b)

(c) (d)

Figure 4.13 Superior (a, c) and inferior (b, d) 3-D views of manually (a, b) and automatically (c, d) segmented cartilage compartments in one of the testing MR images that were halved slicewise.

4.3.1 Computational Analyses

The system described in Subsection 4.1 was experimented on a 4-core 2.8 GHz laptop with 6 GB of RAM and a 500 GB hard disk using MATLAB, which facilitated the implementation with its toolboxes. The computationally most intensive procedure was one-versus-all classification based on approximate k-NN, which was a C++ application called by MATLAB. For instance, according to the computational complexities of approximate k-NN in Subsection 4.1.4.2, classifying a voxel as cartilage or background depending on the FC model of 10 training image sequences would require preprocessing time of $O(350 \times 10^6)$ for data structure construction and $O(12 \times 10^3)$ time to find the approximate 100-NN while ignoring the constant $c_{d,\epsilon}$. However, the computation time of the same task with classification procedure in parallel on 4 cores was $\lceil 10/4 \rceil [O(30 \times 10^6) + O(10 \times 10^3)]$. Therefore, the parallel version was slightly more advantageous in this approach as long as not too many query samples were tested at a time frequently.

The automatic segmentation durations were greatest for FC, which is the largest compartment among all, as listed in Table 4.6.The durations increased proportionally

to the sensitivity of the subsampling techniques for all cartilage compartments because generally the cartilage region had been grown larger than before in the case of increased sensitivity. Also, segmentation durations APA were twice the durations BPA, since the position alignment procedure used the central coordinate information of a cartilage component, which was produced as a result of the first run of the segmentation algorithm. However, those durations can be reduced further by increasing the error bound ϵ and decreasing the number of nearest neighbours k in the approximate k-NN algorithm. The probable consequence is that the segmentation accuracies will be affected. For example, when k was 10 and ϵ was 2, average DSC for FC APA decreased to 15 min for the training models of VC sparse subsampling with approximately 4% decline in average DSC. Increasing the value of ϵ affected the average segmentation accuracies less negatively than decreasing the value of k. Table 4.7 and Table 4.8 demonstrate these effects of the parameters ϵ and k, respectively, on the mean DSC measures and segmentation durations.

Table 4.6 Automatic segmentation durations of the cartilage compartments in minutes BPA and APA when differently subsampled training models were used.

Duration (min)		Uniform	Gaussian	VC Sparse	VC Dense
FC	BPA	12.67	12.29	9.81	9.48
	APA	24.56	23.14	19.22	17.64
LTC	BPA	2.44	2.20	2.09	1.76
	APA	4.05	3.30	3.07	2.65
MTC	BPA	2.15	1.94	1.93	1.60
	APA	3.47	2.93	2.82	2.41
PC	BPA	2.71	2.13	2.09	1.40
	APA	4.99	3.64	3.49	2.55
Total	BPA	19.97	18.56	15.93	14.23
	APA	37.07	33.01	28.60	25.24

Table 4.7 The effect of parameter ϵ on the mean DSC measures and segmentation durations for the compartmental training models of VC sparse subsampling in a subset of 5 testing MR images, when k is 100, and t_c is 0.9.

Measure	ϵ	FC	LTC	MTC	PC
DSC_BPA (%)	0	**82.61**	**76.70**	**81.62**	66.63
	1	82.51	76.59	81.42	**67.22**
	2	82.04	76.69	80.92	66.63
	3	81.53	76.35	80.22	66.01
DSC_APA (%)	0	**83.35**	80.98	81.82	69.82
	1	83.31	81.45	**81.93**	70.97
	2	83.12	82.22	81.69	**72.09**
	3	82.89	**82.26**	81.26	72.04
Duration_APA (min)	0	89.00	11.25	11.85	18.33
	1	25.19	3.71	3.37	4.46
	2	**18.12**	3.03	2.81	3.32
	3	18.71	**2.87**	**2.68**	**3.12**

Table 4.8 The effect of parameter k on the mean DSC measures and segmentation durations for the compartmental training models of VC sparse subsampling in a subset of 5 testing MR images, when ϵ is 2, and t_c is 0.9.

Measure	k	FC	LTC	MTC	PC
DSC_BPA (%)	100	**82.04**	**76.69**	**80.92**	**66.63**
	50	81.64	76.48	80.18	65.35
	10	79.13	73.70	76.66	61.92
DSC_APA (%)	100	**83.12**	**82.22**	**81.69**	**72.09**
	50	82.61	81.78	81.13	71.32
	10	79.76	79.65	78.16	68.91
Duration_APA (min)	100	18.12	3.03	2.81	3.32
	50	17.29	2.66	**2.36**	**2.81**
	10	**14.86**	**2.56**	2.46	3.06

CHAPTER 5

APPLICATON OF MARR-HILDRETH EDGE AND HARRIS CORNER DETECTION METHODS IN VOLUMETRIC IMAGES

In this chapter, how Marr-Hildreth edge detection and Harris corner detection methods can be extended to work in 3-D images is explained in Subsection 5.1 and Subsection 5.2. Subsection 5.3 evaluates advantageous and disadvantageous aspects of the explained 3-D methods overall. The results obtained by processing knee MR images of OAI using the following methods are compared in Subsection 5.3.1; 3-D Marr-Hildreth, 2-D Marr-Hildreth run consecutively in slices, and accelerated 3-D Marr-Hildreth that reduced computational complexity. In Subsection 5.3.2, the interest point detection performances of 2-D and 3-D implementations of the LoG and Harris corner detection methods in binary and intensity-based volumetric images of FC model are discussed.

5.1 Extension of Marr-Hildreth Method

Marr-Hildreth is a method firstly defined to be applied in 2-D images [35], [36]. Its edge detection procedure is based on identification of zero-crossings after LoG filtering that enables revealing of direction-invariant (isotropic) points in images. To extend the 2-D Marr-Hildreth edge detection method into 3-D, first, a mathematical model of the LoG function that considers probable variations in standard deviations of the parameters was derived. Then, an algorithm, which determines the zero-crossing points in rows, columns, and slices depending on 6-connectivity of the voxels, was designed.

5.1.1 LoG Filtering

When rows, columns, and slices of an MR image are denoted with (z, y, x) axes, it is generally the case that the resolution of x axis in these images is lower compared to the resolutions of z and y axes. If smoothing is performed using a spatial filter with a standard deviation of σ_i in physical world units for all axes, the digital standard deviations of this filter can be calculated as described in Subsection 4.1.2. Accordingly, the sizes (s_z, s_y, s_x) of the filter to be applied in the image can be calculated as in (5.1).

$$\left[s_z, s_y, s_x\right] = \left[2\lceil 3\sigma_z \rceil + 1, 2\left\lceil 3\sigma_y \right\rceil + 1, 2\lceil 3\sigma_x \rceil + 1\right] \tag{5.1}$$

Probability distribution of a multivariate Gaussian function $\boldsymbol{G}^{\sigma_i}$ is given in equation (4.1), which is used to compute the 3-D Gaussian filter elements with the mean vector $\boldsymbol{\mu}$ = [0 0 0], covariance matrix $\boldsymbol{\Sigma}$ that have diagonal values of $(\sigma_z^2, \sigma_y^2, \sigma_x^2)$, and axial coordinate vector of the filter elements $\boldsymbol{v}$ composed of the variables (v_z, v_y, v_x). The Laplacian function that is the sum of second order partial derivatives of the 3-variable Gaussian function can be derived with (5.2) ignoring the multiplier of the exponential term in (4.1). For the response of the Laplacian filter produced with this function to be suppressed in regions with homogenous density, the sum of filter values must be 0, and this can be obtained by subtracting the mean filter value from all values of the filter.

$$\begin{aligned}\nabla^2 G(\boldsymbol{v}, \boldsymbol{\Sigma}) &= \frac{\partial^2 G}{\partial v_z^2} + \frac{\partial^2 G}{\partial v_y^2} + \frac{\partial^2 G}{\partial v_x^2} \\ &= \left(\frac{v_z^2}{\sigma_z^4} - \frac{1}{\sigma_z^2} + \frac{v_y^2}{\sigma_y^4} - \frac{1}{\sigma_y^2} + \frac{v_x^2}{\sigma_x^4} - \frac{1}{\sigma_x^2}\right) \exp\left(-\frac{1}{2}\boldsymbol{v}\boldsymbol{\Sigma}^{-1}\boldsymbol{v}^T\right) \\ &= (\boldsymbol{v}\boldsymbol{\Sigma}^{-2}\boldsymbol{v}^T - tr(\boldsymbol{\Sigma}^{-1})) \exp\left(-\frac{1}{2}\boldsymbol{v}\boldsymbol{\Sigma}^{-1}\boldsymbol{v}^T\right)\end{aligned} \tag{5.2}$$

Figure 5.1 visualizes 3-D Gaussian and 3-D LoG filters produced according to the related equations, with higher filter values in darker and lower values in lighter colours for the filter values scaled between [0, 1]. It can be observed from the figure that, as in 2-D, Gaussian filter values are highest around the filter centre, and positive values located close to the centre of the LoG filter are surrounded by negative values.

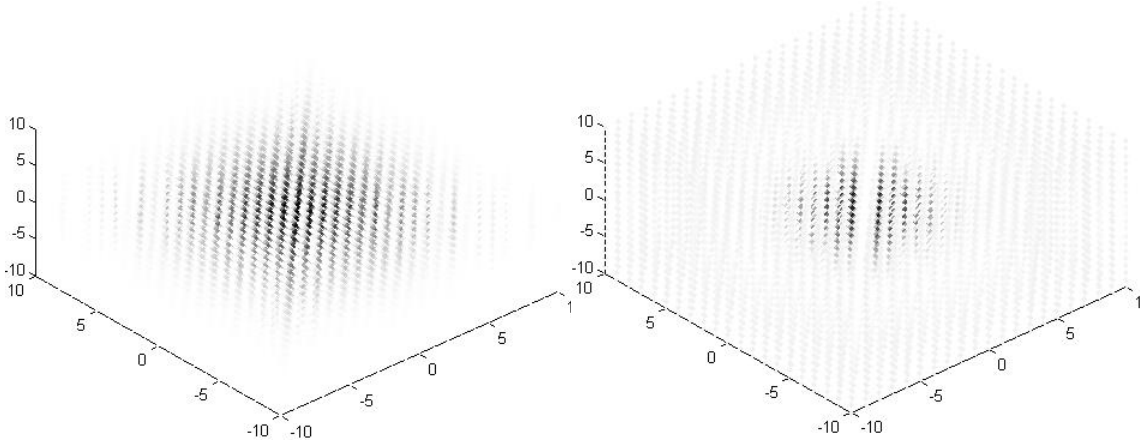

(a) (b)

Figure 5.1 (a) 3-D Gauss, (b) 3-D LoG filters.

Since visualization of 3-D LoG filter values in Figure 5.1 does not allow it to be fully understood, details in some filter slices taken along the z axis are shown in Figure 5.2. When the MR image is isotropic the filter slices along each axis are symmetric as in Figure 5.2 (a), and otherwise they are asymmetric as in Figure 5.2 (b).

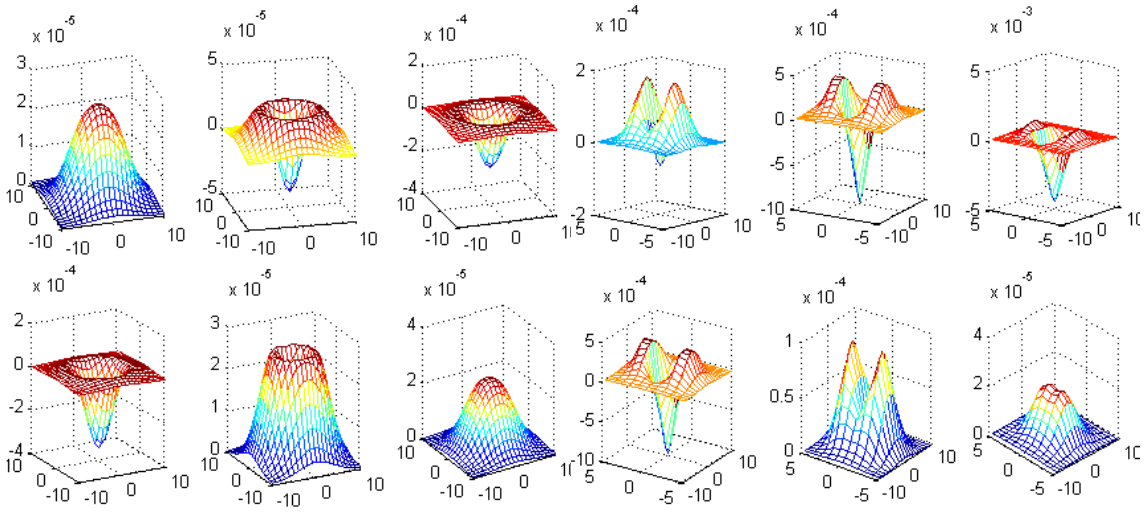

(a) (b)

Figure 5.2 Some slices of 3-D LoG filters along z axis for (a) isotropic and (b) anisotropic MR images.

5.1.2 Finding Zero Crossings

In the Laplacian image generated by convolution of the MR image and LoG filter, the coordinates, where the values of neighbouring elements change sign, indicate the zero-crossing points. When the amplitude of the difference between neighbouring values that change sign is greater than a certain threshold, the zero-crossing points are

assigned as edge points. Thus, thicker edges are thinned, and more robust edge points can be obtained [83].

The two cases illustrated in Figure 5.3 are examined to identify zero-crossing points in a 3-D image by taking the values of the image elements and their neighbours at 6-connectivity into account. In the first case, the image element shown with the minus sign is compared one by one to its 6 neighbours shown with plus sign, and the condition that the element itself is negative, and its neighbour is positive is controlled. When at least one of the six comparisons meets this condition, the element designated with the minus sign is a zero-crossing point. The same element becomes an edge point, if the difference between the values of element-neighbour couples that satisfy the zero-crossing condition is larger than a multiple (for example 0.7 times) of the mean absolute value of the Laplacian image.

In the second case, if at least one of the three axially opposing neighbour couples of a zero-valued image element has a sign change, the central element with the value of 0 becomes the zero-crossing point. If the value difference between any of the opposing neighbours with a sign change is larger than 2 times the threshold used in the first case, the zero-valued central element is determined as an edge point.

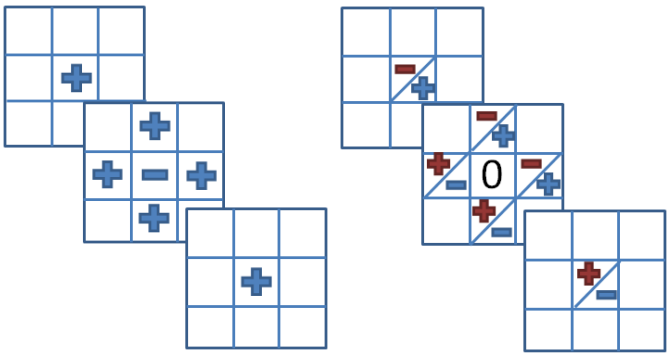

(a) (b)

Figure 5.3 (a) First case and (b) second case examined on Laplacian image to find zero crossing points.

5.2 Extension of Harris Corner Detection Method

Standard Harris corner detection works in 2-D images to search for pixel coordinates, which have significant gradients both along z and y axes within a neighbourhood surrounding themselves. Such pixel coordinates mostly correspond to the corner

points, and are particularly useful since they can be repetitively detected in images that have similar contents. Therefore, they can be identified as the interest points of the image. When extending the Harris corner detection method into 3-D for volumetric images, the effect of gradients along the x axis is taken into consideration as well to compute local intensity differences within Gaussian smoothed windows, and the cornerness value of the voxels is measured according to these integral differences. Then voxel coordinates with high cornerness value are determined as the possible corner or interest points.

5.2.1 Scale-Space Representation

In the standard case, the scale-space representation of a volumetric image $\boldsymbol{I}$ is constructed by repetitively smoothing the image using spherical Gaussian filters $\boldsymbol{G}^{\sigma_i}$ to detect the corner points with various scales of the physical world denoted by σ_i. Hence, details at fine scale are gradually removed to enable the significant gradients at coarser scales to be caught as the probable interest points. This repetitive smoothing operation can be applied again every time the image is resized so that the scale-space is represented at multiple levels of details [38], which significantly contribute the scale invariance of the interest point detectors.

The scale-space of $\boldsymbol{I}$ is a four-dimensional data structure for each level of the image, so a voxel element of the scale-space is indexed by the scale and coordinate tuple of $(\sigma_i, \boldsymbol{c})$. The corner detection algorithm is run in each 3-D image $\boldsymbol{I}^{\sigma_i}$ with the scale of σ_i, and the cornerness image C^{σ_i} is obtained. Then, the voxel coordinates that have maximal cornerness value within their four-dimensional local neighbourhood $\boldsymbol{W}$, which contain the voxels from rectangular spatial regions in the contiguous scales, are searched in each level of the scale-space.

However, detection of corners using the scale-space representation of intensities may lead to poor localization of the corners on the surface of an object of interest, because the gradient estimation for cornerness measurement is performed in smoothed volumetric images within the constructed scale-space. The case of low localization of the corner points may constitute a disadvantage depending on the purpose of the corner detection procedure, especially when the corners are used to establish

automatic correspondences on the object surfaces. Consequently, a slightly different approach was followed in our 3-D Harris corner detection method to determine well-localized corners in the scale-space representation, which involved iteratively smoothing the first-order derivative products rather than smoothing the intensities, as clarified in the following subsection.

5.2.2 Measurement of Cornerness

Initially, the first-order partial derivatives, $\boldsymbol{I}_z$, $\boldsymbol{I}_y$, and $\boldsymbol{I}_x$, were computed squeezing the derivative of a 1-D Gaussian filter along the respective axes similar to the filters in Figure 4.4 to accurately determine the coordinates of salient locations in the volumetric image $\boldsymbol{I}$. Then, pairwise products of the first-order derivatives were repetitively smoothed as in (5.3) with the 3-D Gaussian filters $\boldsymbol{G}^{\sigma_i}$ both to construct a scale-space representation and an auto-correlation matrix $\boldsymbol{M}$. Accordingly, each element in the images of derivative products was weighted by its surrounding neighbours within a Gaussian sphere of radius $3\sigma_i$ depending on their distances so that farther neighbours had less effect on the subsequently constructed matrix $\boldsymbol{M}$. Thus, convolving the derivative products with local Gaussian windows defined by σ_i, $\boldsymbol{M}$ could represent the image gradients along different directions, other than the three main directions of z, y, and x, and define local geometry of the image plane. The correspondent elements of the pairwise products of first-order derivatives at a coordinate $\boldsymbol{c}$ comprise the $3x3$ auto-correlation matrix $\boldsymbol{M^c}$ given in (5.4).

$$\boldsymbol{M} = \boldsymbol{G}^{\sigma_i} * \begin{bmatrix} \boldsymbol{I}_z^2 & \boldsymbol{I}_z\boldsymbol{I}_y & \boldsymbol{I}_z\boldsymbol{I}_x \\ \boldsymbol{I}_y\boldsymbol{I}_z & \boldsymbol{I}_y^2 & \boldsymbol{I}_y\boldsymbol{I}_x \\ \boldsymbol{I}_x\boldsymbol{I}_z & \boldsymbol{I}_x\boldsymbol{I}_y & \boldsymbol{I}_x^2 \end{bmatrix} = \begin{bmatrix} \boldsymbol{A} & \boldsymbol{D} & \boldsymbol{E} \\ \boldsymbol{D} & \boldsymbol{B} & \boldsymbol{F} \\ \boldsymbol{E} & \boldsymbol{F} & \boldsymbol{C} \end{bmatrix} \tag{5.3}$$

$$\boldsymbol{M^c} = \begin{bmatrix} \boldsymbol{A}(\boldsymbol{c}) & \boldsymbol{D}(\boldsymbol{c}) & \boldsymbol{E}(\boldsymbol{c}) \\ \boldsymbol{D}(\boldsymbol{c}) & \boldsymbol{B}(\boldsymbol{c}) & \boldsymbol{F}(\boldsymbol{c}) \\ \boldsymbol{E}(\boldsymbol{c}) & \boldsymbol{F}(\boldsymbol{c}) & \boldsymbol{C}(\boldsymbol{c}) \end{bmatrix} \tag{5.4}$$

The cornerness values C^{σ_i} of the image voxels were measured through the linearized formula in (5.5), which was based on the determinant and trace of the auto-correlation matrix $\boldsymbol{M}$ as well as a constant coefficient k_H. Although a coefficient depending on σ_i was also added prior to the determinant term in the study by Yu et al. [46], it did not

indicate an improvement on the resulting corners detected. Therefore, this coefficient was neglected in (5.5). The determinant of $\boldsymbol{M}$ was calculated as in (5.6) according to the Sarrus rule defined for finding determinant of 3x3 matrices. The trace of $\boldsymbol{M}$ given in (5.7) was obtained by addition of the diagonal values of $\boldsymbol{M^c}$ for every voxel coordinate $\boldsymbol{c}$. Alternatively, the determinant and trace of $\boldsymbol{M}$ could have been found by multiplication and addition of the three eigenvalues of $\boldsymbol{M^c}$, respectively. Nevertheless, the latter approach would be computationally more complex, since it requires eigenvalue decomposition of every $\boldsymbol{M^c}$.

$$\mathrm{C}^{\sigma_\mathrm{i}} = |\boldsymbol{M}| - k_H \, tr(\boldsymbol{M})^3 \tag{5.5}$$

$$|\boldsymbol{M}| = \boldsymbol{A}_{\square}\boldsymbol{B}_{\square}\boldsymbol{C} + \mathbf{2}(\boldsymbol{D}_{\square}\boldsymbol{F}_{\square}\boldsymbol{E}) - (\boldsymbol{E}_{\square}\boldsymbol{B}_{\square}\boldsymbol{E}) - (\boldsymbol{A}_{\square}\boldsymbol{F}_{\square}\boldsymbol{F}) - (\boldsymbol{D}_{\square}\boldsymbol{D}_{\square}\boldsymbol{C}) \tag{5.6}$$

$$tr(\boldsymbol{M}) = \boldsymbol{A} + \boldsymbol{B} + \boldsymbol{C} \tag{5.7}$$

Consequently, unlike the standard approach of Harris corner detection method run in the scale-space of image intensities, instead of first performing smoothing operations on the image, then computing the first-order derivative products, and again smoothing these products for determining the weighted gradients, only computation of the first-order derivative products and their convolution with the filters of $\boldsymbol{G}^{\sigma_\mathrm{i}}$ were realized in the proposed approach. However, the proposed approach was considered to incorporate the basic functionalities of the standard one.

5.2.3 Suppression of Weak Corners

According to the formula in (5.5), the cornerness value is expected to increase for the interior region voxels, edge voxels, and corner voxels with respect to the order of their mentioning. Therefore, to detect the true corner points in the image a threshold $t_H^{\sigma_\mathrm{i}}$ over the cornerness values $\mathrm{C}^{\sigma_\mathrm{i}}$ should be applied such that voxel coordinates with cornerness value greater than or equal to $t_H^{\sigma_\mathrm{i}}$ are accepted as the probable corners. This threshold was dynamically computed according to (5.8) based on the maximum and minimum cornerness values of the voxels at scale σ_i, and the coefficient r_C that specified the narrowing ratio of range of cornerness values.

$$t_H^{\sigma_\mathrm{i}} = \mathrm{C}_{min}^{\sigma_\mathrm{i}} + r_\mathrm{C} \left| \mathrm{C}_{max}^{\sigma_\mathrm{i}} - \mathrm{C}_{min}^{\sigma_\mathrm{i}} \right| \tag{5.8}$$

Finally, the corners not locally maximum in cornerness value in the scale-space representation were suppressed to emphasize the strong corners alone. For this purpose, every element in each C^{σ_i} were controlled whether it has the maximal cornerness value in a multi-rectangular window $\boldsymbol{W}$, which was centred at coordinate $\boldsymbol{c}$ of the controlled element at σ_i. The checked condition to assign $\boldsymbol{c}$ as the corner point or not for a $\boldsymbol{W}$ with the size of $[s_z, s_y, s_x, s_\sigma]$ can be defined as in (5.9), where $(\boldsymbol{v}, \sigma_{\boldsymbol{W}})$ pair denoted the coordinate and scale of the elements in $\boldsymbol{W}$, and was assigned to a range of values that are indicated by the following set: $\left\{(\boldsymbol{v}, \sigma_{\boldsymbol{W}}) \middle| \boldsymbol{v} = \left[\left(-\left\lfloor\frac{s_z}{2}\right\rfloor, \left\lfloor\frac{s_z}{2}\right\rfloor\right), \left(-\left\lfloor\frac{s_y}{2}\right\rfloor, \left\lfloor\frac{s_y}{2}\right\rfloor\right), \left(-\left\lfloor\frac{s_x}{2}\right\rfloor, \left\lfloor\frac{s_x}{2}\right\rfloor\right)\right], \sigma_{\boldsymbol{W}} = \left(\sigma_{i-\left\lfloor\frac{s_\sigma}{2}\right\rfloor}, \sigma_{i+\left\lfloor\frac{s_\sigma}{2}\right\rfloor}\right)\right\}$.

$$\begin{cases} \boldsymbol{c}\ is\ a\ corner\ at\ scale\ \sigma_i, & \forall(\boldsymbol{v}, \sigma_{\boldsymbol{W}}) \in \boldsymbol{W},\ C^{\sigma_i}(\boldsymbol{c}) - C^{\sigma_w}(\boldsymbol{c}+\boldsymbol{v}) \geq t_{\boldsymbol{d}} \\ \boldsymbol{c}\ is\ not\ a\ cornerat\ scale\ \sigma_i, & otherwise \end{cases} \quad (5.9)$$

5.3 Experimental Results

Marr-Hildreth edge detection and Harris corner detection methods in 3-D, which are described in Subsection 5.1 and Subsection 5.2, were implemented, and evaluated through two separate sets of experiments. Subsection 5.3.1 presents the experiments for comparison of 3-D Marr-Hildreth method with its accelerated 3-D and 2-D versions. The experiments in Subsection 5.3.2 were performed for comparative analysis of 3-D Harris corner detection method, its 2-D version, and LoG filtering approaches that were modified for finding the interest points in 2-D slices of a volumetric image or directly in a volumetric image.

5.3.1 Edge Detection with Marr-Hildreth Method

20 3-D DESS knee MR images of OAI with dimensions of (280 x 280 x 143) in (z, y, x) were processed using 3-D Marr-Hildreth, 2-D Marr-Hildreth applied on every slice of the image, and accelerated 3-D Marr-Hildreth method that reduced computational complexity. Figure 5.4 shows three consecutive slices of one of the MR images used in comparison of these methods.

When the number of elements in the MR image is denoted with N, and each dimension of the LoG filter is roughly accepted as s, computational complexity of the convolution of the 3-D filter with the entire MR image and convolution of the 2-D filter

with each slice of the image are $O(Ns^3)$ and $O(Ns^2)$, respectively. The accelerated 3-D filtering technique that reduces the complexity of 3-D filtering operation, which exponentially increase with a rise in the value of s, down to $O(8Ns)$ without significantly changing the precision of the filtering operation, was based on the separability property of the 3-D LoG filter according to (5.10) [32]. In this technique, convolution of one dimensional (1-D) LoG and Gauss filters stretched along z, y, and x dimensions were consecutively convolved with the MR image in the order they appear in the equation, and the obtained results were merged.

$$\begin{aligned}\nabla^2 G(\boldsymbol{v}, \boldsymbol{\Sigma}) = {} & \nabla^2 G(v_z, \sigma_z) * G\big(v_y, \sigma_y\big) * G(v_x, \sigma_x) \\ & + G(v_z, \sigma_z) * \nabla^2 G\big(v_y, \sigma_y\big) * G(v_x, \sigma_x) \\ & + G(v_z, \sigma_z) * G\big(v_y, \sigma_y\big) * \nabla^2 G(v_x, \sigma_x)\end{aligned} \tag{5.10}$$

The dimensions of the LoG and Gauss filters were computed using equation (5.1) with the σ value assigned to be 1.1 mm, which is the approximate cartilage thickness in knee joint [8]. Accordingly, 3-D LoG filter was in dimensions of (21 x 21 x 11), 2-D Log filter was (21 x 21), and 1-D Gauss or 1-D LoG filters used by the accelerated 3-D method in z, y, and x axes were (21 x 1), (21 x 1), and (11 x 1), respectively. In a computer with a processing power of 2.8 GHz, while the convolution of an MR image with 3-D LoG filter lasted about 57 seconds, convolution with 1-D filters used for the accelerated 3-D LoG filtering method only lasted about 2 seconds.

The edge points found in the images after LoG filtering were identified by detecting zero-crossing points depending on 6-connectivity of the voxels for 3-D and accelerated 3-D Marr-Hildreth methods (Subsection 5.1.2), and 4-connectivity of the pixels in the slices for 2-D Marr-Hildreth method. Figure 5.5 shows the LoG filtering results of 3-D, 2-D, and accelerated 3-D methods from left to right; for 53rd, 54th, and 55th MR image slices in Figure 5.4 from top to bottom. The edge points detected in the 54th slice of the same MR image are as in Figure 5.6 for the three methods from left to right with the same order.

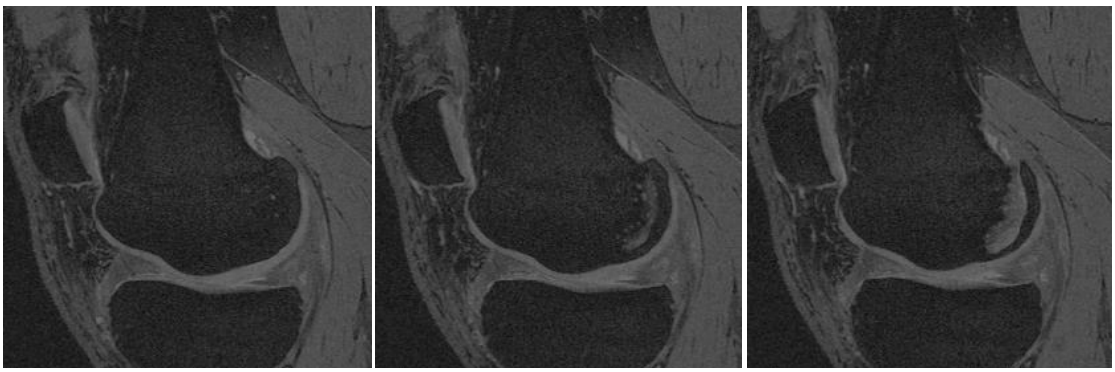

(a) (b) (c)

Figure 5.4 (a) 53rd, (b) 54th, and (c) 55th slices of an MR image.

Since 3-D LoG filtering also took the image elements along the axis of slices into account, its filtering results appeared smoother and more photographic compared to 2-D filtering results. However, it can be observed that the edge images of 3-D methods contained most of the principal edges of bone and cartilage tissues in the edge images of 2D method. Additionally, the fact that 3-D method is sensitive to variations in the z dimension caused more prominent edges and locally clustered edge points in Figure 5.6 (a) in comparison to Figure 5.6 (b) due to the differences between the LoG image slices in Figure 5.5 (a), (d) and (g). The LoG and edge images of the accelerated 3-D method were indistinguishably similar to those of the 3-D method.

When DSC measure in (1.1) was calculated between the edge points found by the 3-D and accelerated 3-D methods for 20 MR images, the average DSC value was found as 0.99. This indicates that there were some, albeit minor, differences between these methods. On the other hand, since the scope of the 3-D methods is wider than that of the 2-D method, it is not plausible to directly compare the edge points found by these two methods using DSC measure. But, it was found that on the average of 20 MR images 37% of the edge points detected by the 2-D method overlap with the edge points detected by the 3-D method. Slight deviations in the relative locations of the edge points found by the methods owing to the smoothing property of LoG filtering, and loss of significance in some high intensity differences within 2-D slices, when differences in all three dimensions are taken into consideration, can be regarded among the factors that caused this percentage of overlap to be low.

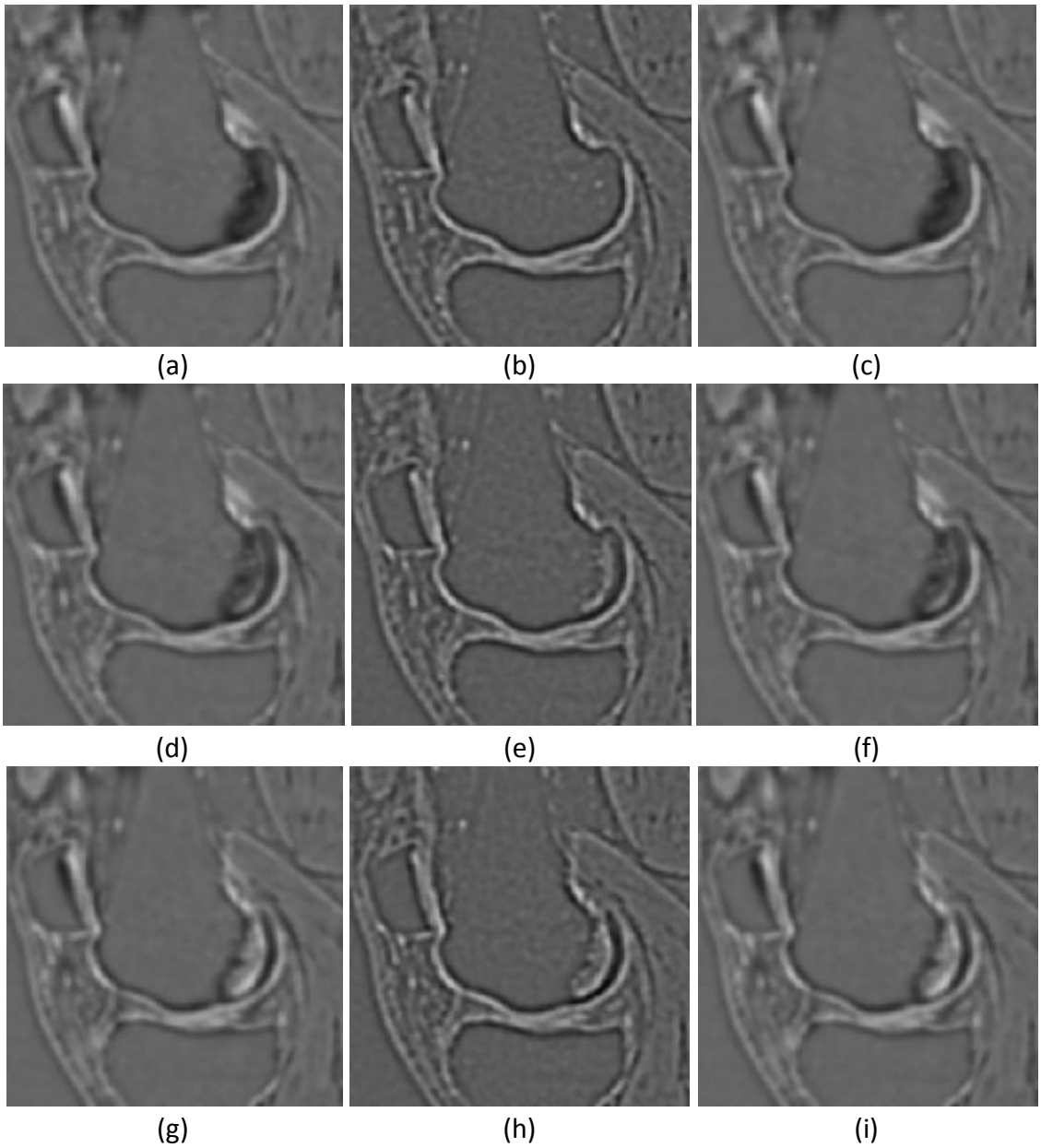

Figure 5.5 LoG filtering results of 3-D (a,d,g), 2-D (b,e,h) and accelerated 3-D (c,f,i) Marr-Hildreth methods in 53rd (a-c), 54th (d-f), and 55th (g-i) MR image slices given in Figure 5.4.

(a) (b) (c)

Figure 5.6 Edge points detected with (a) 3-D, (b) 2-D, and (c) accelerated 3-D Marr-Hildreth methods in 54th MR image slice given in Figure 5.4.

5.3.2 Interest Point Detection with LoG Filtering and Harris Corner Detection

Volumetric binary and intensity-based images of FC model were interpolated to have the property of isotropy along the axes. Then, they were processed to qualitatively assess the proposed 3-D Harris corner detection method, LoG filtering-based 3-D interest point detection method, and slicewise 2-D implementations of these methods. Interest point finding with LoG filtering approach was realized via weak corner suppression (Subsection 5.2.3) in both the original and negative LoG filtered volumetric images, and then finding local maximum or minimums in their scale-space representation (Subsection 5.2.1). The 3-D LoG filtering operation explained in Subsection 5.1.1 was implemented according to the optimized equation in (5.10) for the experiments presented in this subsection. Similarly, all 3-D Gaussian filtering operations in the methods were optimized with consecutive convolutions using 1-D Gaussian filters as in (5.11) to reduce the computational complexity of the volumetric image smoothing.

$$G(\boldsymbol{v}, \boldsymbol{\Sigma}) = G(v_z, \sigma_z) * G(v_y, \sigma_y) * G(v_x, \sigma_x) \tag{5.11}$$

Figure 5.7 shows the interest points detected by the four methods at various scales, which were indicated by lighter colours as the scale increased. The constant coefficient k_H in (5.5) is known to yield best results with a value in between 0.04 and 0.06 for 2-D Harris corner detection method [42], so was assigned to 0.05 for 2-D implementation of the method. However, it was observed to be effective with the value of 0.005 for the 3-D implementation of the method as proposed in the study by Laptev and

Lindeberg [44]. The coefficient r_C in (5.8) was given different values for different methods to have a subset of strongest interest points roughly in similar regions so that a qualitative evaluation of the methods could be feasible. r_C was determined as 1 for the 2-D implementations to maintain the strongest interest points only whereas it was 0.9 for 3-D LoG filtering method to remove some of the densely distributed corners over the interior surface of the object of interest. In 3-D method of Harris, corners at most salient locations of the object were obtained when r_C was 0.5. The scale of physical world σ_i was set to each of the values in the set of $\{0.5, 0.7, 1, 1.4\}$ in mm. $\boldsymbol{W}$ was determined as $[3, 3, 4]$ for the 2-D and $[3, 3, 3, 4]$ for the 3-D implementations to detect locally maximal corners greater in cornerness value than their neighbours in all scales by the threshold $t_{\boldsymbol{d}} = 0.01$. The standard deviation of 1-D Gaussian filter, which was differentiated to compute the first-order derivatives in Harris corner detection method, was set to 0.08 for both of the 2-D and 3-D implementations. This approximately resulted in the differentiating vector of $[5, 0, -5]$, which was squeezed along the z, y, and x axes.

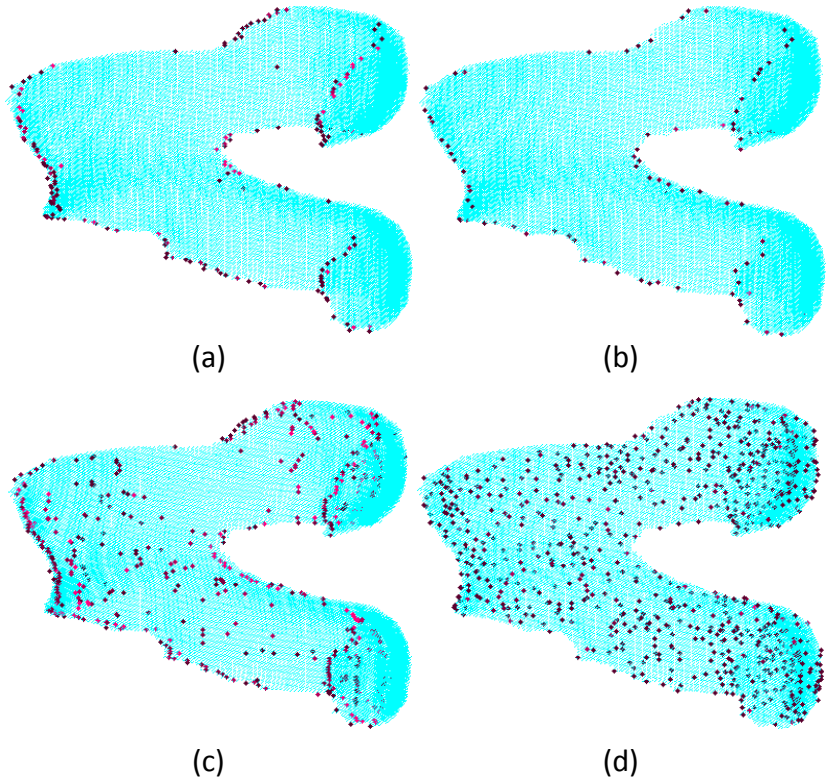

Figure 5.7 The interest points detected by (a) 2-D and (b) 3-D methods of Harris as well as (c) 2-D and (d) 3-D LoG filtering-based methods in a binary image of FC model.

According to Figure 5.7, 2-D implementations of Harris and LoG filtering generated interest points assembled near the boundaries of FC surface, since local maximization procedures did not take the voxels along x axis into consideration. The interest points of 3-D LoG filtering-based method tended to be distributed over the interior surface of the object when corners of 3-D Harris method were in most salient positions on the object surface. This tendency of 3-D LoG filtering-based method did not alter even when values of r_C or $t_{\boldsymbol{d}}$ were changed to 0.95 and 0.5, respectively, as demonstrated in Figure 5.8. In general, interest points of LoG filtering-based method deviated from their expected positions near the surface boundaries with the rise of the values in the set of scales. However, interest points were rather stable in their salient positions with the proposed 3-D Harris corner detection method even when the values in scale set were increased to $\{1, 1.4, 2, 2.8\}$ (see Figure 5.9).

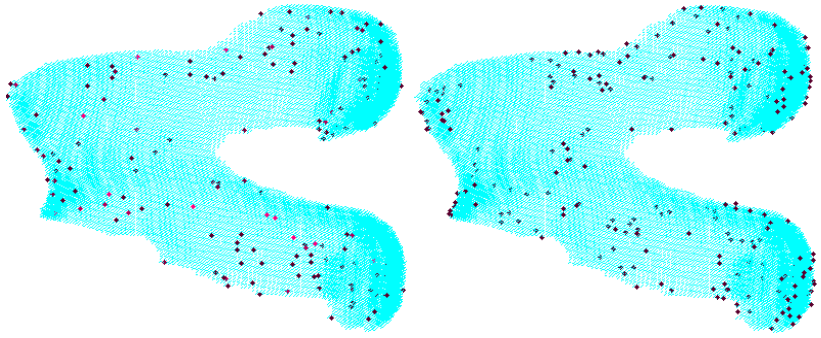

(a) (b)

Figure 5.8 The interest points detected when (a) r_C was changed to 0.95, or (b) $t_{\boldsymbol{d}}$ was changed to 0.5 for 3-D LoG filtering-based method.

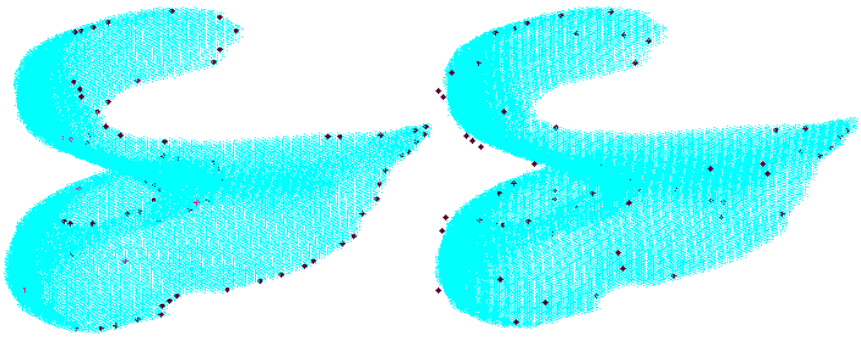

(a) (b)

Figure 5.9 The interest points detected with (a) 3-D Harris corner detection method and (b) 3-D LoG filtering-based method when the values in scale set were doubled.

Running of the methods with the same parameter values in an intensity-based volumetric image of FC produced the interest points depicted in Figure 5.10. For all of

the methods, the detected points differed from those detected in binary FC image due to the effects of noise or inhomogeneity of the cartilage tissue voxels in intensity-based images. Nevertheless, the interest points of 2-D or 3-D Harris corner detection method were observed to be influenced by these effects less than the points of LoG filtering-based method.

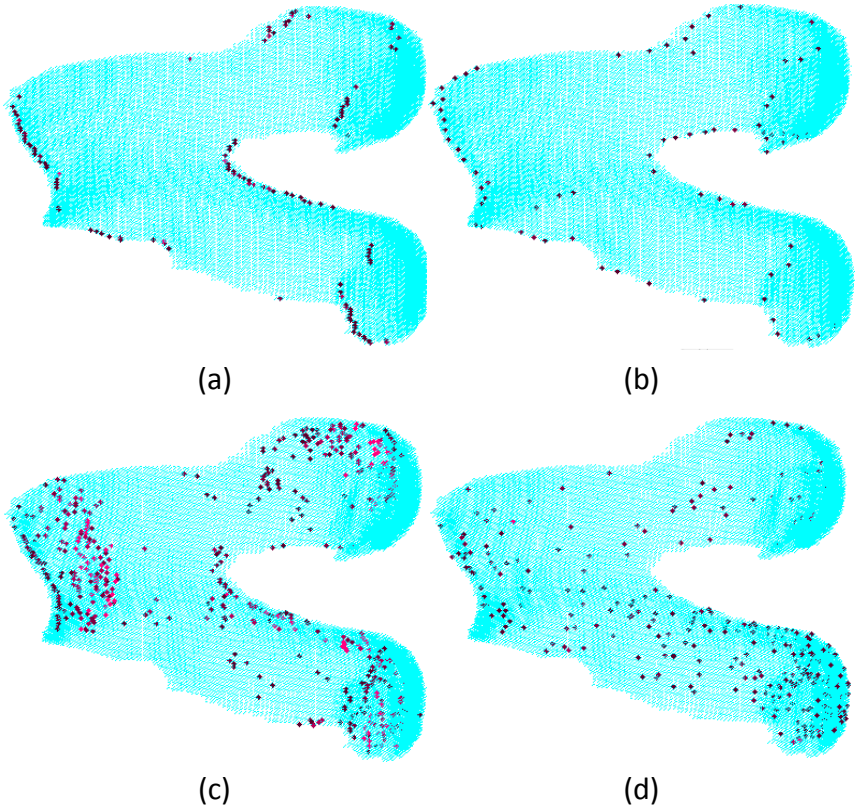

Figure 5.10 The interest points detected by (a) 2-D and (b) 3-D methods of Harris as well as (c) 2-D and (d) 3-D LoG filtering-based methods in an intensity-based FC image.

Moreover, the proposed implementation of Harris corner detection in scale-spaces based on first-order derivative products was compared to its standard implementation in scale spaces based on intensities in Figure 5.11 using parameters similar to those aforementioned. The proposed method was observed to produce more stable interest points in significant positions near the surface boundaries. Although for the standard implementation $t_H^{\sigma_i}$ and $t_{\boldsymbol{d}}$ were set to directly 0 and a very small value of 0.005, the number of found interest points was fairly insufficient.

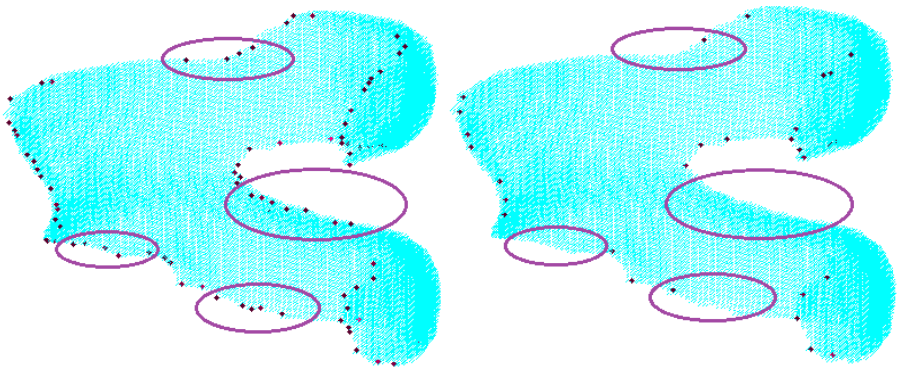

(a) (b)

Figure 5.11 The results of 3-D Harris corner detection method on volumetric binary model of FC using the scale-space representations based on (a) first-order derivative products or (b) intensities.

The proposed 3-D Harris corner detection method resulted in a sparser set of interest points near the surface boundaries of FC with the introduced values of parameters. But, it was also possible to produce a dense set of interest points over the FC surface decreasing the value of coefficient r_C in (5.8) as shown in Figure 5.12. Consequently, the proposed method enables implementation of automatic correspondence finding algorithms that establish correspondences of dense sets of interest points over the objects of interest.

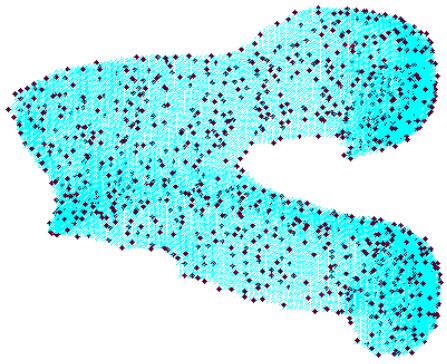

Figure 5.12 A denser set of interest points on the surface of FC with the proposed 3-D Harris corner detection method.

CHAPTER 6

HYBRID CARTILAGE SEGMENTATION WITH INTEGRATION OF VOXEL CLASSIFICATION-BASED SEGMENTATION AND ACTIVE APPEARANCE MODEL SEGMENTATION

Segmentation by classification-driven region-growing algorithm is an appropriate approach for the degenerative nature of the cartilage. However, it may be prone to inaccurate segmentations especially in the case of severe full-depth deteriorations, and cannot totally handle oversegmentation and undersegmentation issues alone as indicated in Figure 6.1. Integration of high-level cues such as relative positions and shapes of the cartilage compartments with the voxel classification-driven region-growing algorithm may address the aforementioned segmentation problems, and enhance the automatic segmentation results. Because, the relative positions of cartilaginous compartments are fixed, and these compartments have roughly similar morphology in spite of their probability of degeneration in time.

Consequently, this chapter describes a hybrid cartilage segmentation system, which was designed to fuse the segmentation results of a tissue classification module and an appearance modelling module. The tissue classification module was based on the classification-driven region-growing algorithm described in Chapter 4. The appearance modelling module segmented the testing MR images masked with the initial segmentation results of tissue classification module using the previously trained appearance model that depended on statistical parameters of shape and texture. Thus, the hybrid segmentation system paves the way for that the classification probabilities of the former module can be regulated by the shape and texture information of the latter module.

(a) (b) (c)

Figure 6.1 Some oversegmented cartilage spurs in automatic segmentation results of voxel-classification-driven region-growing algorithm that ran depending on training models of VC sparse subsampling. The spurs are especially distinguishable for (a) FC, (b) PC, and (c) LTC.

Figure 6.2 illustrates the interaction between the main modules of the hybrid cartilage segmentation system. Since the tissue classification module is explained in detail in Chapter 4, only the modules of appearance modelling and information fusion are clarified in the Subsection 6.1. The results of the experiments related to the AAM segmentation and early hybrid segmentation are assessed especially for FC compartment in Subsection 6.2.

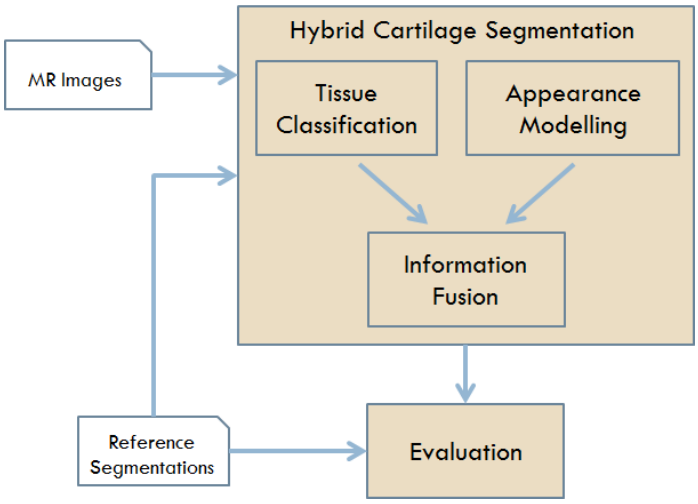

Figure 6.2 The main modules of the hybrid cartilage segmentation system.

6.1 Methodology

The proposed hybrid cartilage segmentation system is presented in detail particularly for appearance modelling and information fusion modules in Figure 6.3. Atlas generation and correspondence finding are auxiliary modules to enable running of appearance model generation procedure.

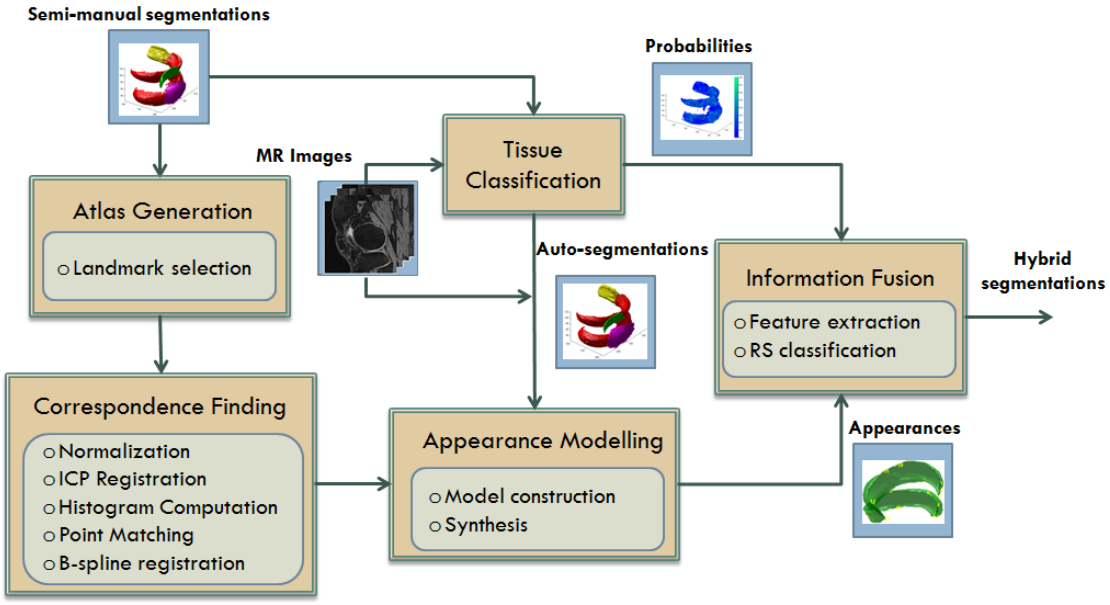

Figure 6.3 The main and auxiliary modules of the proposed hybrid cartilage segmentation system in detail.

The tissue classification module of the hybrid system ran depending on the training models of VC sparse subsampling technique. In atlas generation, correspondence finding, and appearance modelling modules, 10 training MR images used in tissue classification module were also processed during the course of training the appearance models. Before training of the appearance model, first of all, the semi-manual segmentations of the training MR images were preprocessed to generate binary or intensity-based atlases of every cartilage compartment in atlas generation module. Then, set of dense correspondences were determined on the atlas surfaces of each compartment so that an appearance model of the respective compartment was constructed to represent statistical variations of shape and texture between the atlases.

Prior to AAM segmentation, the binary automatic segmentation results of tissue classification module were used to mask 23 testing MR images to remove most of the irrelevant parts and focus roughly on the cartilage compartment of interest. During segmentation, the masked intensity-based volumetric images of a compartment were tried to be synthesized by the related appearance model using a search algorithm, which was previously trained to guess the optimal parameter update for the model. Thus, the belonging probabilities of image voxels to a cartilage compartment were

obtained through the segmentation based on voxel classification-driven region growing algorithm in a testing MR image. Furthermore, the compartmental appearance information, which combined both the shape and texture information, was obtained through the AAM segmentation. Finally, information fusion module was considered for integration of the appearance information and belonging probabilities to correct false classifications in segmentation results especially due to oversegmented spurs in cartilage compartments.

6.1.1 Atlas Generation

Atlases can be conveniently generated based on the semi-manual segmentations of the cartilage compartments. Better representation of the anatomical variations of the compartmental morphology in between participants requires use of multiple atlases [84]. However, rise in number of atlases leads to a further increased computational complexity for multi-atlas registration-based segmentation methods [10], [85], [86]. Hence, the number of atlases used by the method should be adjusted so that trade-off between the segmentation accuracies and computational complexity is satisfied.

Accordingly, the cartilage compartments that did not have large significant deterioration in 10 training MR images were retrieved as volumes delineated by the semi-manual segmentations to generate the atlases. Then, each compartmental cartilage volume was morphologically closed through 5 times dilation followed by 5 times erosion using a sphere with 5-pixel diameter to fill in small holes, and obtain a slightly smoother atlas. The resulting binary volume was used as a mask on the original training MR image to obtain an atlas composed of intensities. Therefore, 10 binary atlases and 10 intensity-based atlases were recorded both for each compartment separately and for all compartments in a combined manner as multi-object atlases. The multi-object atlases were considered to be useful for incorporation of relative positional information of the compartments into segmentation process. Figure 6.4 shows a slice of the semi-manually delineated FC volume in a training MR image, and the corresponding slices of the binary and intensity-based FC atlases generated for this MR image. Figure 6.5 depicts various binary FC compartment atlases, which were generated with the described closing operation, in 3-D view.

(a) (b) (c)

Figure 6.4 The corresponding slices of (a) semi-manually segmented volume, (b) binary atlas, and (c) intensity-based atlas of FC compartment in a training MR image.

Figure 6.5 Various binary atlases generated for FC compartment using morphological closing operation in 3-D.

6.1.1.1 Landmark Selection

A subset of interest points at salient positions close to the atlas boundaries were semi-automatically selected as landmarks from among those detected over a binary atlas surface. Since 2-D Harris corner detection algorithm could determine larger number of well-localized interest points that have higher probability of correspondence in between atlases (see Subsection 5.3.2), this algorithm was run in binary atlases of the compartments. Then, a number of interest points roughly in similar positions were collected through a user interface to determine the corresponding landmarks for the atlases of each compartment type.

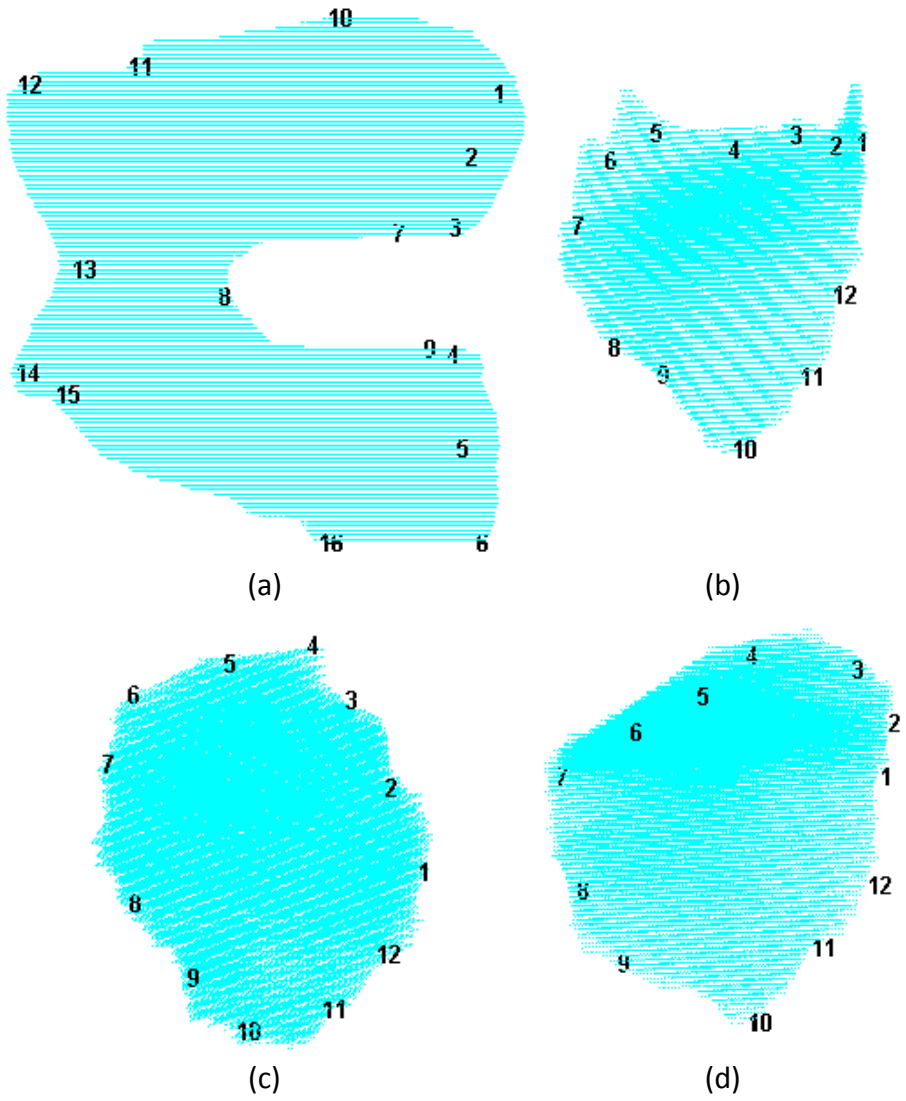

Figure 6.6 Interest points semi-automatically collected as landmarks on the surfaces of (a) FC, (b) LTC, (c) MTC, and (d) PC atlases of a training MR image.

These compartmental landmarks were firstly useful to measure the accuracy of found correspondences in correspondence finding procedure (Subsection 6.1.2). After correspondence finding via registration, the landmarks on a reference atlas surface were propagated to the target atlas surfaces so that the difference between the propagated landmarks of the reference atlas and semi-automatically collected landmarks of a target atlas could be computed. Secondly, compartmental landmarks enable computation of some geometric features, which can be effective in designing classifiers for the information fusion module (Subsection 6.1.4). Computation of the geometric features is possible via propagation of the landmarks on reference atlas to the AAM segmentation result, which is the synthesized cartilage compartment in a testing MR image by the appearance model (Subsection 6.1.3.2). The landmark

propagation operation was achieved through B-spline registration process based on the point correspondences between the reference and target surfaces.

6.1.2 Correspondence Finding

The point correspondences between the atlas surfaces were established to be able to construct an appearance model for a compartment. One of the atlases for each compartment of interest was selected as the reference atlas volume denoted by $\boldsymbol{V}_r$ and the rest were determined as the target atlas volumes denoted by $\boldsymbol{V}_t$. The surfaces of $\boldsymbol{V}_r$ and $\boldsymbol{V}_t$ were represented at two scales as triangular meshes of faces and vertices that form each of these faces. The set of vertices, in other words points, at two scales constituted two point clouds so that the point cloud in fine scale included larger number of points than the one in coarse scale. The point clouds for $\boldsymbol{V}_r$ at coarse and fine scales are denoted by $\boldsymbol{P}_r$ and $\boldsymbol{P}_{r_L}$, where r is a fixed integer that identifies the reference atlas. Similarly, the point clouds for $\boldsymbol{V}_t$ at coarse and fine scales are denoted by $\boldsymbol{P}_t$ and $\boldsymbol{P}_{t_L}$, where t is an integer in the set of $\{1,2,\dots,N_A\}$ that includes r, and N_A is the number of atlases for a cartilage compartment of interest. Accordingly, an iterative procedure using shape context [88] was run to register the reference point cloud $\boldsymbol{P}_r$ to the target point cloud $\boldsymbol{P}_t$ in coarse scale by executing a number of steps, which are depicted in Figure 6.7, and explained through the following subsections.

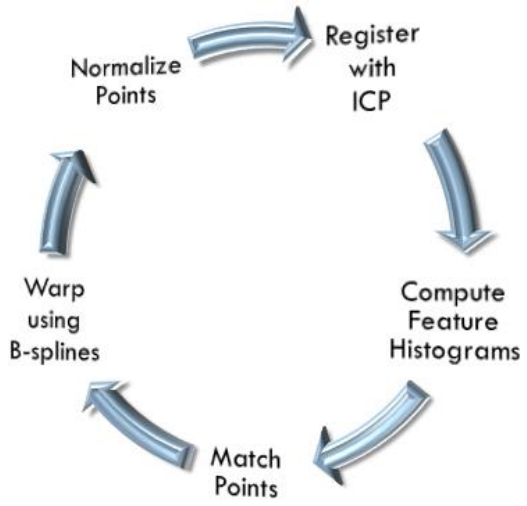

Figure 6.7 Steps of the iterative registration procedure for finding point correspondences on atlas surfaces.

6.1.2.1 Point Normalization

Each point in the point cloud of $\boldsymbol{P}_r$, $\boldsymbol{P}_{r_L}$, $\boldsymbol{P}_t$, or $\boldsymbol{P}_{t_L}$ was normalized by being shifted with the mean and scaled with the mean length of its respective point cloud. Equations (6.1) and (6.2) give the mean and scale computations for the point cloud $\boldsymbol{P}_r$, and equation (6.3) indicates how the normalization of each point $\boldsymbol{p}_r^j$ in $\boldsymbol{P}_r$ was performed, where N_r denotes the number of points in $\boldsymbol{P}_r$.

$$\boldsymbol{\mu}_r = \frac{1}{N_r}\sum_{j=1}^{N_r} \boldsymbol{p}_r^j \tag{6.1}$$

$$\mathrm{s}_r = \frac{1}{N_r}\sum_{j=1}^{N_r} \left\|\boldsymbol{p}_r^j\right\| \tag{6.2}$$

$$\boldsymbol{p'}_r^j = \frac{\boldsymbol{p}_r^j - \boldsymbol{\mu}_r}{\mathrm{s}_r}, \quad j = 1 \dots N_r \tag{6.3}$$

6.1.2.2 Iterative Closest Point Algorithm

After point normalization, iterative closest point (ICP) algorithm [89], [90] was run to register a target atlas point cloud $\boldsymbol{P}_t$ to the reference atlas point cloud $\boldsymbol{P}_r$. Main steps of ICP are briefly explained in the following paragraphs.

1. Determine the closest point $\boldsymbol{p'}_r^k$ as $\boldsymbol{p'}_y^j$ in $\boldsymbol{P}_r$ for each point $\boldsymbol{p'}_t^j$ in $\boldsymbol{P}_t$ using 1-NN algorithm with Euclidean distance. $\boldsymbol{p'}_t^j$ indicates j$^{\text{th}}$ normalized point of t$^{\text{th}}$ target atlas.
2. For the closest point pairs ($\boldsymbol{p'}_y^j$, $\boldsymbol{p'}_t^j$), compute alignment parameters of translation $\boldsymbol{T}$, scale s, and rotation $\boldsymbol{R}$ according to the equations (6.4), (6.5), and (6.6), respectively. Because s and $\boldsymbol{R}$ are needed to compute $\boldsymbol{T}$, and $\boldsymbol{R}$ is needed to compute s, the parameters should be computed in proper order.

$$\boldsymbol{T} = \boldsymbol{\mu}_y - s\boldsymbol{R}(\boldsymbol{\mu}_t) \tag{6.4}$$

$$s = \frac{\sum_{j=1}^{N_t} \boldsymbol{p'}_y^j \boldsymbol{R}(\boldsymbol{p'}_t^j)}{\sum_{j=1}^{N_t} \left\|\boldsymbol{p'}_t^j\right\|^2} \tag{6.5}$$

$$\boldsymbol{R} = \overline{\boldsymbol{Q}}^{\boldsymbol{T}} \boldsymbol{Q} \tag{6.6}$$

3. Transform target point cloud $\boldsymbol{P}_t$ according to the alignment parameters $\boldsymbol{T}$, s, and $\boldsymbol{R}$, and obtain the registered target point cloud $\boldsymbol{P}_{t'}$.
4. Compute the cost of iteration by averaging the point differences between $\boldsymbol{P}_{t'}$ and $\boldsymbol{P}_r$.
5. Iterate as if $\boldsymbol{P}_t$ is $\boldsymbol{P}_{t'}$ while the cost of iteration is improved more than its 2%.

Appendix B clarifies the ICP algorithm in Subsection B.2 by focusing on derivation of the optimal translation $\boldsymbol{T}$, scale s, and rotation $\boldsymbol{R}$ for determining the point correspondences with minimal error. Mathematical basics of the quaternions, which are useful to derive the optimal rotation equation (6.6), are given in Subsection B.1.

6.1.2.3 Feature Histogram Computation

Histograms of features for both the reference atlas points $\boldsymbol{P}_r$ and registered target atlas points $\boldsymbol{P}_{t'}$ were individually formed in this step. For each point of a shape in coarse scale, its difference from each other point of the same shape in fine scale was computed. Then, the computed features for a point using these differences included the logarithm of point difference norms denoted by $\boldsymbol{f}_n$; a normalized angle between z-y coordinates of the differences denoted by $\boldsymbol{f}_a$; and unit x direction of the differences, denoted by $\boldsymbol{f}_x$. The resulting values of $\boldsymbol{f}_n$, $\boldsymbol{f}_a$, and $\boldsymbol{f}_x$ were scaled with 10, 10 and 7, respectively. As a result, a histogram with 10x10x7 bins for ($\boldsymbol{f}_n$,$\boldsymbol{f}_a$,$\boldsymbol{f}_x$) sequence was constructed and stored for each point.

6.1.2.4 Point Matching

The reference atlas points $\boldsymbol{P}_r$ were matched to registered target atlas points $\boldsymbol{P}_{t'}$ that had closest feature histograms. For every point in $\boldsymbol{P}_r$ the histogram distances were computed for every other point in $\boldsymbol{P}_{t'}$. Point pairs farther than the maximum distance

threshold were assigned to a cost of infinity. Then, point matches between the first and second sets with the minimum costs were identified. If the cost of matching for matched point pairs was infinite, these matches were removed.

6.1.2.5 B-spline Registration

The point matches were regulated with a B-spline grid using a coarse-to-fine refinement strategy. B-spline warped point positions were computed using original target atlas points $\boldsymbol{P}_t$, reference atlas points $\boldsymbol{P}_r$, and the determined matches. The warping between data sets is kept diffeomorphic, by constraining the Jacobian of the B-spline transformation grid. Accordingly, the registered reference atlas point cloud $\boldsymbol{P}_{r'}$ was obtained by updating the point coordinates of $\boldsymbol{P}_r$.

$\boldsymbol{P}_{r'}$ as part of a triangulated mesh was converted into a volume of voxels, and the holes of this volume were filled in. Later, the warped reference atlas points were matched to interpolated points on the object boundary $\boldsymbol{V}_t$ to increase DSC between the registered reference atlas and the target atlases. Finally, already registered reference atlas was again B-spline warped based on the interpolated point positions found in the previous step.

6.1.3 Appearance Modelling

6.1.3.1 Model Construction

Training of appearance model was constructed using the corresponding meshes, which describe the atlas surfaces [91]. Using 4 scales of these meshes, the following steps were performed.

1) A shape model was prepared to describe the mean and variance of the atlas meshes with principal component analysis [92].
2) A texture model was prepared to describe the mean and variance of the intensity-based atlas texture with principal component analysis.
3) A combined model of shape and texture information was prepared, since they can be correlated to each other.

4) A search model was prepared to find the parameters of the location and the combined shape-texture of interested compartment in testing MR images.

When training for the search model, the appearance model and translation parameters were modified with a known amount, and error was measured between the intensities that form the genuine atlas and intensities described by the model. Then, correlations between the modification amount and the found error were used to prepare an inverse model.

6.1.3.2 Synthesis

The models constructed at different scales during AAM training was applied beginning from the coarsest scale up to the finest scale in the accordingly resized testing MR images masked with the automatic segmentations that were obtained through tissue classification using training models of VC sparse subsampling method. AAM segmentation was accomplished by iteratively preparing an error vector with the difference between the model and testing MR image intensities, and querying the search model with this error vector to obtaining the optimal parameter and location update for the appearance model. Thus, approximate synthesis of the automatically segmented compartment by the model without loss of main shape information was targeted.

6.1.4 Information Fusion

The final hybrid segmentations are considered to be produced by the classifiers, which were trained mainly with the false classifications, depending on the probabilities, intensities of AAM segmentation, and some geometrical features, which were computed according to the surface points of AAM segmentation and the propagated landmarks on this surface.

6.2 Experimental Results

Table 6.1 gives the results of the correspondence finding procedure for FC when a KLG-2 right knee of a male at age 72 and with height 1.70 m, weight 77.8 kg, and BMI 27.0 kg/m^2 was used as the reference atlas. Figure 6.8 shows the reference FC atlas in

combination with some target FC atlases, and the registered reference atlas as well as the mapped landmarks after the correspondence finding procedure.

Two experiments were performed for the appearance model segmentation. The first experiment involved training the AAM with 10 FC atlases, which were also in the training set of tissue classification module. In the second experiment the training set was split into two groups one of which included five participants with heights greater than or equal to 1.60 m and weights greater than or equal to 90 kg, and the other contained the remaning five. The former and latter groups were named as large and small groups, respectively. The aim of the second experiment was to observe whether the model could be improved when its description for the principal variations of appearance is limited to samples with similar properties so that all testing MR images could be approximately segmented with this appearance model without loss of overall segmentation accuracies. AAM segmentation with these models resulted in the accuracies in Table 6.2.

Table 6.1 Accuracies and durations of correspondence finding phase for each of 10 training FC compartment atlases.

Atlas ID	Mean Point Distance	Landmark Distance Mean	Landmark Distance Std.	Duration (hour)	Number of Vertices
1	0.52	9.70	10.44	3.07	19270
2	0.69	14.38	10.36	5.26	26676
3	0.63	11.29	8.17	3.76	22092
4	0.58	11.00	7.72	3.44	21000
5	0.72	7.89	4.02	6.33	28972
6	0.59	8.65	5.81	2.44	18232
7 (reference)	0.010	4.82×10^{-3}	6.34×10^{-3}	3.42	20806
8	0.65	15.76	8.22	4.24	23882
9	0.57	7.98	6.14	2.58	18396
10	0.55	10.82	7.12	2.94	18442

(a)

(b)

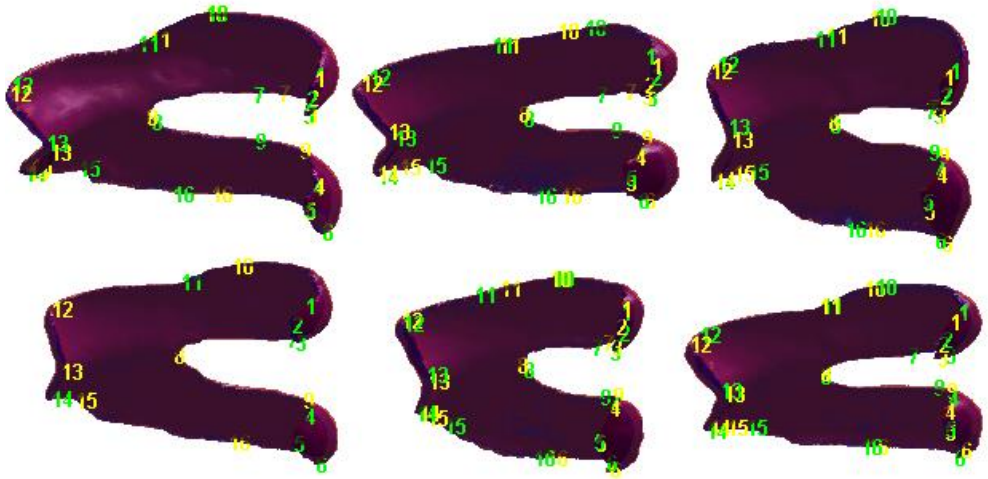

(c)

Figure 6.8 (a) Reference atlas, which is illustrated at lower left, in blue drawn on to red target atlases shown in Figure 6.5. (b) Reference atlas drawn on to target atlases after registration. (c) Landmarks of target atlases in green and propagated landmarks of registered reference atlas in yellow enumerated on the registered atlas surfaces in (b).

Table 6.2 AAM segmentation accuracies and durations for the two experiments.

Test	**Model of 10 training FC atlases**				**Models of 5 large/5 small FC atlases**			
MR ID	DSC	sensitivity	specificity	duration	DSC	sensitivity	specificity	duration
1	75.21	79.09	99.68	13.13	62.69	67.02	99.52	13.47
2	**14.11**	**15.22**	**98.41**	**14.31**	**73.66**	**82.02**	**99.36**	**13.26**
3	68.05	74.39	99.56	13.95	64.74	71.68	99.51	13.55
4	75.01	82.32	99.53	14.17	73.63	80.65	99.52	13.95
5	**33.63**	**40.11**	**99.30**	**13.93**	**72.19**	**85.65**	**99.63**	**14.27**
6	80.11	80.08	99.73	14.15	73.00	74.86	99.59	13.26
7	77.15	88.91	99.62	14.35	74.30	87.96	99.55	13.47
8	73.65	84.99	99.58	14.60	71.18	84.73	99.51	14.01
9	**25.00**	**20.08**	**99.43**	**13.22**	**57.93**	**67.84**	**99.06**	**13.20**
10	72.94	85.48	99.54	14.04	63.87	77.47	99.39	13.83
11	76.14	86.75	99.51	13.77	71.93	83.99	99.41	13.67
12	67.40	75.63	99.25	14.16	63.51	72.36	99.15	13.41
13	73.61	82.88	99.54	14.22	70.78	81.52	99.47	13.79
14	71.40	76.37	99.61	13.24	67.78	73.97	99.54	13.99
15	**71.39**	**80.89**	**99.54**	**13.90**	**40.57**	**34.39**	**99.65**	**13.35**
16	75.86	83.04	99.43	13.91	74.62	83.18	99.37	13.79
17	3.53	2.41	99.59	13.39	3.60	2.82	99.34	13.62
18	**31.17**	**31.09**	**99.33**	**13.57**	**62.98**	**64.07**	**99.62**	**13.91**
19	73.11	77.10	99.46	14.16	66.81	72.22	99.30	13.63
20	66.13	68.37	99.38	13.32	74.73	75.85	99.56	13.41
21	**68.77**	**77.19**	**99.30**	**13.84**	**1.11**	**0.92**	**99.05**	**14.28**
22	74.82	72.20	99.68	13.77	74.43	75.75	99.57	13.87
23	76.94	81.66	99.48	14.17	73.69	77.00	99.46	14.20
Mean	***61.96***	***67.23***	***99.46***	***13.88***	***62.33***	***68.60***	***99.44***	***13.70***

The training of AAM was achieved in about 80 min and 60 min for the first and second experiments, respectively. Mean AAM segmentation durations of FC in a testing MR image did not significantly differed for the two experiments, and were approximately 14 min.

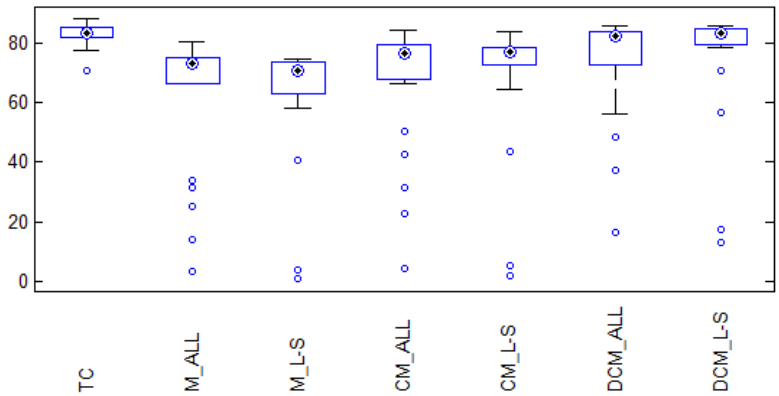

Figure 6.9 Box plots of DSC values obtained with classication-based segmentation of tissue classification module (TC), segmentation with AAM trained using all trainin atlases, segmentation with AAM trained using splited training atlases into large and small groups.

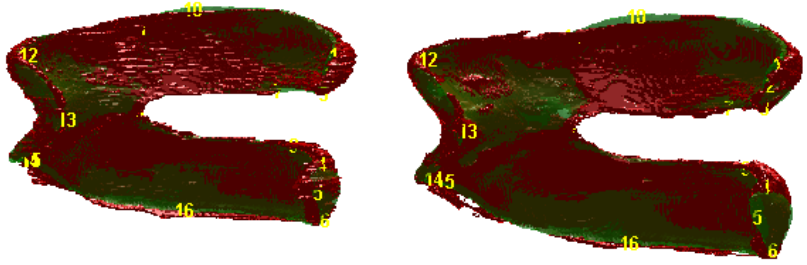

(a)

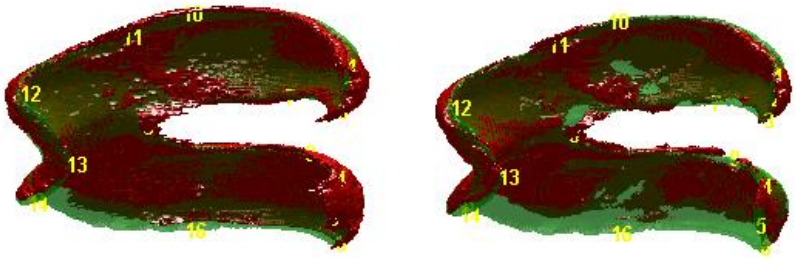

(b)

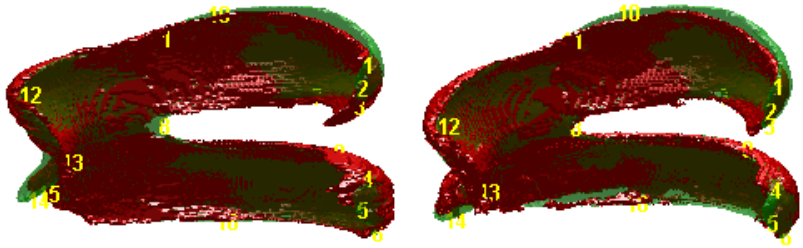

(c)

Figure 6.10 Sample AAM segmentations of FC compartment, which could roughly adapt to the automatic segmentation results in three different MR images in (a), (b), and (c). AAM segmentations are in green and drawn on top of the manual segmentations (left hand side) and automatic segmentations (right hand side) of FC depicted in red.

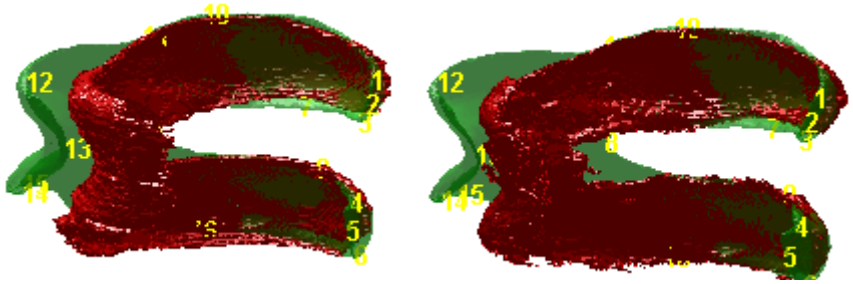

(a)

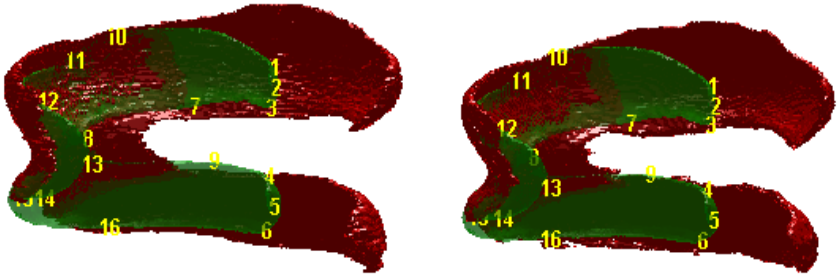

(b)

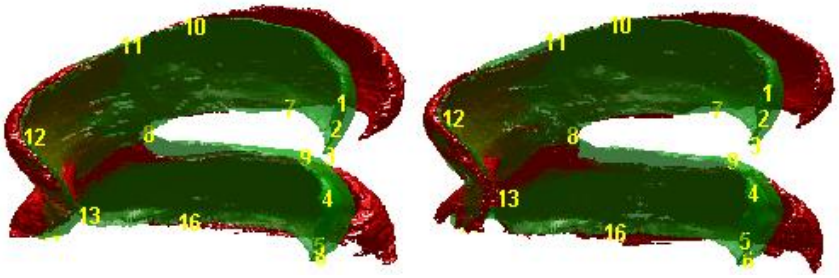

(c)

Figure 6.11 Sample AAM segmentations of FC compartment, which could not apparently adapt to the automatic segmentation results in three different MR images in (a), (b), and (c). AAM segmentations are in green and drawn on top of the manual segmentations (left hand side) and automatic segmentations (right hand side) of FC depicted in red.

The confusion matrix for the automatic segmentation results of FC by the tissue classification module is as in Table 6.3. According to these automatic segmentation results, intersection of the voxels that have probabilities of being FC higher than 0 with the voxels classified as cartilage despite being background (FP) is 100%. In addition, intersection of the voxels that have probabilities of being FC higher than 0 with the voxels classified as background despite being cartilage (FN) is 72.41%, so 27.59% of the FC voxels had 0% probability of being cartilage in average.

Table 6.3 Confusion matrix for automatic segmentation results of FC by the tissue classification module.

Positive	**TP**	**FN**
	0.97%	0.25%
Average	*109,270*	*28,506*
Negative	**TN**	**FP**
	98.61%	0.16%
Average	*11,055,846*	*17,582*

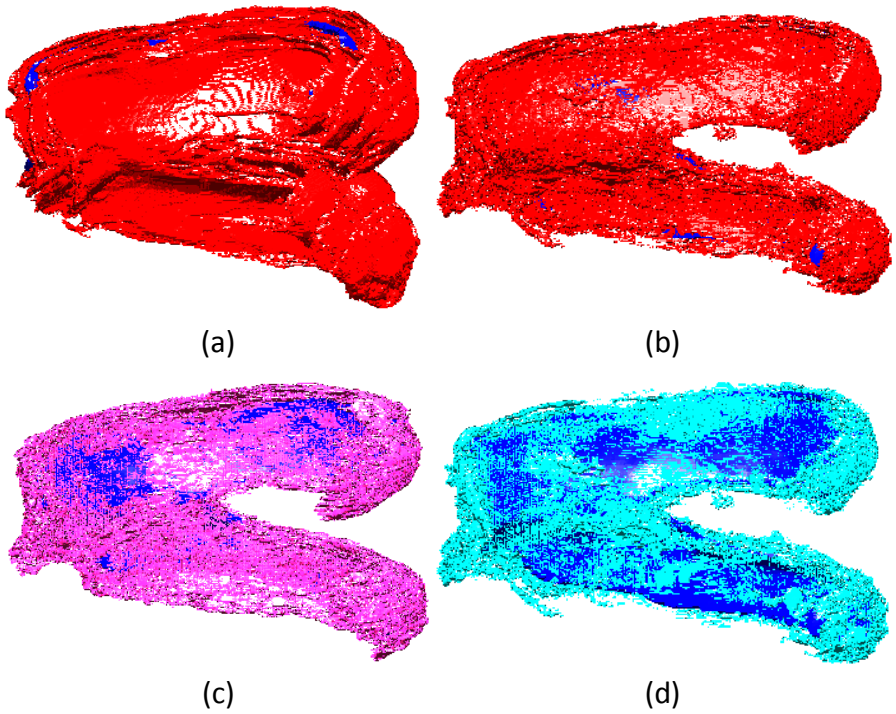

(a) (b)

(c) (d)

Figure 6.12 Segmentation results of FC for the testing MR images that had DSC values above 50% in Table 6.2 (a) without any transformation and (b) with transformation into the frame of reference atlas. The transformed (c) FN and (d) FP classifications into the frame of reference atlas.

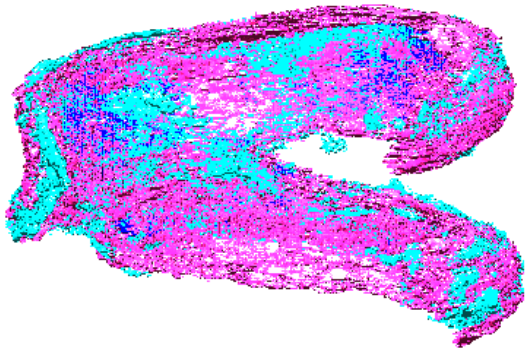

Figure 6.13 Combined error map of FP and FN classifications of tissue classification.

CHAPTER 7

DISCUSSION AND CONCLUSIONS

This chapter mainly discusses the methodological approaches and results of the segmentation system described in Chapter 4 in comparison to related works. Then, it concludes the thesis with an overview of the core findings and contributions of the presented studies in Chapter 4, Chapter 5, and Chapter 6, and a few suggestions on future works that may worth researching.

Direct comparison of the results of the related studies in the literature is generally unreasonable because of their dependence on distinct data sets of MR images. These data sets are constructed through different standards with various sizes or qualities by scanning participants who have specific symptoms of osteoarthritis or do not have any symptoms at all. Moreover, manual segmentations used for validation of the automatic segmentations are always affected by segmenter variability. Nonetheless, taking these factors into account, the results of the studies mentioned in Subsection 1.1 and our study can be mutually assessed.

Since most of the related studies used DSC measure to validate the automatic segmentations, Table 7.1 lists the DSC means and standard deviations of segmented cartilage compartments for these studies to facilitate the assessments. The studies were grouped in the table according to their requirement to find a volume of interest (VOI), segment a bone, or determine BCI before segmentation of a cartilage compartment. The average DSC values for the study by Vincent et al. [21], which came first in the SKI10 challenge [19], were given as presented by Shan et al. [10].

Because deterioration of cartilage can affect the segmentation accuracies negatively [8], [12], high DSC values obtained in some studies may be attributed to

their conduct of the experiments in MR images of only healthy participants [9]. Zhang et al. [17] processed MR images of participants with unknown health status. Some studies [10], [15], [16], [23] partially involved osteoarthritic participants, whereas some others [11], [12], [22] included osteoarthritic participants exclusively as our study did. Studies that used SKI10 data set [20], [21] segmented MR images scanned before knee surgeries, so they handled purely pathological cases.

In addition to this, validation was performed partially for some studies by using the selected slices of MR images due to large labour intensity of 3-D manual segmentations [16], [22], or evaluating parts of the cartilage compartments [10], [15], [20], [21]. Studies that used SKI10 data set [20], [21] segmented only load-bearing regions of articular cartilage in tibiofemoral joint, and Shan et al. [10] segmented load-bearing regions of FC. Consequently, accuracies of the whole 3-D cartilage compartments could not be provided by these studies. Although segmentation of only load-bearing regions that have higher probability of cartilage deterioration can lead to a fall in average accuracies, pieces of the cartilage compartment boundaries, where segmentation errors mostly occur due to oversegmentation, were eliminated with partial validation.

Furthermore, an increase in the number of training MR images can improve system accuracies [22] bringing about yet longer segmentation durations. Therefore, studies that trained their system using a greater number of MR images were more probable to obtain higher DSC values, e.g. [11] with 58, [21] with 80, and [12] with 44 training MR images. Leave-one-out cross-validation method, which enables use of most of the MR images for training while achieving testing of all MR images, was applied in [9], [17], [22], [23]. The studies with limited data sets were Lee et al. [22] with 10 MR images, Tamez-Pena et al. [23] with 6 images, Zhang et al. [17] with 11 images, and Hani et al. [18] with 3 images. In spite of being an uncommon practice, processing of multi-modal images for each participant can highlight the cartilaginous tissues so that notable accuracies can be obtained as in the study by Zhang et al. [17], which processed four MR images with different modalities for a participant.

It is hard to mention if any method is significantly superior to another overall. Though, as can be understood from Table 7.1 that accuracies of PC compartment

considerably increased for the methods that had localized segmentation strategies. Among the other studies, our work is mostly comparable to the work by Dam et al. [12], which used the same MR image data sets of OAI as ours. But, they could improve the accuracies approximately 2% for LTC and 1% for PC compartments despite their heavy preprocessing with multi-atlas registration. Consequently, it can be inferred that our study has attained comparable segmentation accuracies with respect to some previous studies, especially when application of our approach on exclusively knee MR images of symptomatic participants is taken into consideration.

Table 7.1 Percentage means and standard deviations of the compartmental DSC values for some of the studies in the literature and our study.

	Study	FC	LFC	MFC	TC	LTC	MTC	PC
NONE	Folkesson et al. [15]	—	—	77±8	—	—	81±6	—
	Our study	82.6±3.6	—	—	83.1±3.0	84.6±3.7	81.3±3.3	72.6±8.5
VOI	Dam et al. [12]	—	84.2±4.	81.4±4.4	—	86.6±3.4	81.2±5.5	73.9±11.6
BONE & BCI	Yin et al. [16]	84±4	—	—	80±4	—	—	80±4
	Fripp et al. [9] (SVM)	86.2±4	—	—	81.2±5	—	—	81.7±10.5
	Fripp et al. [9] (HDM)	84.8±7.6	—	—	82.6±8.3	—	—	83.3±13.5
	Lee et al. [22]	82.5±2.8	—	—	80.8±2.57	—	—	82.1±3.89
BONE	Vincent et al. [21], [10]	86.1±6.5	—	—	86.5±5.4	—	—	—
	Tamez-Pena et al. [23]	88±4.	—	—	84±5.	—	—	—
	Zhang et al. [17]	86.4±8.7	—	—	88.0±10.2	—	—	84.1±7.4
	Shan et al. [10]	76±4.8	—	—	84.1±3.7	—	—	—
	Wang et al. [11]	85.0±3.3	—	—	83.7±4	—	—	79.2±8.88
	Lee et al. [20]	72±8	—	—	72±7	—	—	—

Similarly, due to the fact that our work and the other works processed MR images with different sizes, segmented some or parts of cartilage compartments in the knee joint, or were run on different platforms, a direct computational performance comparison among them cannot be made. Moreover, most of the researchers did not clearly explain if the provided measures were for the entire cartilage segmentation procedure including the VOI, bone, or BCI determination, and segmentation of all cartilage compartments. As to computational performances of the studies in Table 7.1, Folkesson et al. [15] noted that they had achieved automatic segmentation of MFC and MTC in a testing MR image in 10 min on a 2.8 GHz standard desktop. But, Dam and Loog [30] stated that their efficient algorithms dropped 2.5-hour computation time of the original work by Folkesson et al. [15] to 16 min. Some researchers made no mention of the segmentation durations of their possibly computationally demanding

approaches requiring multi-atlas registrations or statistical shape model searches [11], [12], [23]. The studies that had segmentation durations for an MR image above the average were Zhang et al. [17] with 33 min when using a 48-core high performance computer and Shan et al. [10] with at least 10 hours. Other studies that had roughly close performances provided the following details on their approximate segmentation durations and experimental platforms; Yin et al. [16] in 20 min with Intel Core 2 Duo 2.6 GHz processor and 4 GB RAM, Fripp et al. [9] 15 min for SVM-based and 15-30 min for HDM-based methods, Vincent et al. [21] in 15 min with Intel Core 2 Duo and Core 2 Quad processors, Lee et al. [22] in 15-21 min, and Lee et al. [20] in 40 min with 2.4 GHz 2 Quad processor and 2 GB RAM. Our study can be ranked among these studies with its 29-minute mean segmentation duration in total for training models of VC sparse subsampling (Table 4.6).

In conclusion, it is necessary to deal with large number of voxels in MR images either using localized approaches or subsampling methods to implement efficient MR image segmentation systems based on voxel-classification approaches. In the study mentioned in Chapter 4, we experimentally showed that vicinity-correlated background voxel subsampling method is a better choice than uniform or Gaussian subsampling to distinguish objects of interest from other similar and close structures frequently encountered in MR images, especially for objects with highly curved and complex shapes. Furthermore, it was possible to obtain reasonable accuracies with respect to the studies in the literature for segmentation of cartilage compartments in high-field knee MR images through voxel-classification-driven region-growing algorithm, when training models of VC sparse subsampling and a proper set of values for the system parameters were used. Consequently, the findings of this study can provide a basis for other researches that focus on segmentation of anatomical structures in MR images with voxel-classification. The performance of the classification procedure could be substantially increased due to elimination of a great deal of background voxels in the training models and reduced number of features. Additionally, the proposed system could segment the cartilage compartments without prior segmentation of bones or determination of BCI, and requiring multiple MR images of a participant. Therefore, the system can be applied efficiently without

significant loss of accuracies even for MR images of osteoarthritic participants, which makes it promising from clinical point of view.

In 3-D Marr-Hildreth edge detection study presented in Chapter 5, it was observed that the method expanded into third dimension could maintain the ability of the standard method in finding the principal edges within 2-D slices along with gaining further sensitivity against intensity differences in the direction of the slices. Moreover, it was experimentally verified that the described accelerated 3-D Marr-Hildreth implementation can perform a successful approximation by expediting the application of high-dimensional LoG filter of the 3-D method. Nonetheless, there are some shortcomings related to the presented 3-D Marr-Hildreth method. Since Marr-Hildreth edge points do not depend on direction information, improving the points with directional information as in the Canny edge detection method, or finding the surface normal for the points, which are known to belong to anatomical surfaces [31], require additional computations. Furthermore, when the LoG filter is constructed with different digital standard deviations on the axes as allowed by the equation (5.2), the symmetry of the filter within the slices disappears, and the method is applied at the cost of losing its property of isotropy. To overcome this issue MR images can be interpolated so that the image resolutions are equal in all axes [37].

With regard to the conclusions of the interest point detection study in Chapter 5, 3-D methods prevented the points assembled in local regions on FC surface, since they took the voxels along the slices into consideration when computing the local maximums in all scales. Therefore, they led to more distinct points in more distinguishable positions. The fact that 3-D Harris corner detection method found interest points especially near the surface boundaries was intuitively reasonable, since strongest interest points are expected to be located in such salient positions. But, this did not necessarily mean that the method of 3-D Harris could not find interest points on interior surfaces. A denser set of interest points over FC surface was possible with this method by increasing the range of cornerness values for the detected points. However, strongest interest points tended to reside only over interior surfaces of FC for 3-D LoG filtering-based method. The dissimilarity between these two methods in positions of strongest points probably resulted from their different definitions of

interest points such that 3-D LoG filtering-based method assumed interest points to have large gradients in all directions rather than taking mainly the three directions of (z, y, x) into account as in 3-D method of Harris [46]. Overall, results indicated that the proposed 3-D Harris corner detection, which worked depending on scale-space of the first-order derivative products, was superior in determining well-localized corners in salient positions near the surface boundaries of FC models. Nevertheless, the rotation or scale invariance comparison of the interest points detected by the assessed methods remains as an open question for future works.

In Chapter 6, AAM segmentation could not successfully synthesize the FC compartments in all testing MR images, and hence the information fusion module could not be realized as intended. Therefore, voxel classification-based segmentation method was experimentally shown to be more effective than the hybrid segmentation method for FC. This result was in contradiction with the hypothesis revealed in Subsection 1.3. However, in spite of being trained with only 5 or 10 atlases, the appearance models approximately accomplished synthesis of FC compartment in most of the testing MR images by preserving the main shape of FC. Moreover, AAM segmentation results enabled inter-participant transformation of the reference atlas among testing MR images. Accordingly, error analysis of the tissue classification module could be performed.

If segmentation of all testing MR images is achieved by the appearance modelling module and the information fusion module is implemented as described in Subsection 6.1.4 depending on the learned misclassifications, then the hybrid segmentation method may lead to a more reliable cartilage segmentation system. Because then, both the degenerative characteristic and approximate appearance of the cartilage compartments are to be taken into consideration to obtain the final segmentations. In addition to this, compartmental shape information determined via AAM segmentation may refer to non-deteriorated original morphology of the cartilage compartment, so be useful in measurement of approximate tissue loss when analysed in comparison to the results of the tissue classification module.

The following future works may be considered concerning automatic segmentation and assessment of the cartilage in MR images of the knee joint. Training of the

appearance models with greater number of atlases or proper modification of AAM segmentation algorithm may be tried in order to improve the hybrid segmentation method. If the cartilage compartments can be delineated with high accuracies, quantitative measurements such as thickness [93], [94], [95], volume [8], [96], or surface area over the segmented cartilage compartments are possible. Because most of the segmentation errors occur close to the compartmental boundaries and most of deterioration is over the load-bearing regions of the cartilage, trimming of the compartmental segmentation results or sub-compartmental evaluation may be considered [8]. But such operations are likely to require also segmentation of the bones as well as BCI determination. Furthermore, temporal assessment of the MR images of a participant with respect to his previous scans is important to monitor the progress of osteoarthritis. For this purpose, it is reasonable that training the segmentation system using the scans of a single participant and testing it with the subsequent scans of the same participant can yield better segmentation results [97]. Nonetheless, this requires all training images of each participant to be manually segmented, which is an extremely laborious task for the trained segmenters.

REFERENCES

[1] Preim, B. and Bartz, D., (2007).Visualization in Medicine: Theory, Algorithms, and Applications, Morgan Kaufmann, Amserdam.

[2] Birkfellner, W., (2014). Applied Medical Image Processing: A Basic Course, CRC Press Taylor & Francis Group, London.

[3] Taylor, R. H., (2006). "A Perspective on Medical Robotics", Proceedings of the IEEE, 94(9): 1652-1664.

[4] Pham, D. L., Xu, C., and Prince, J. L., (2000). "Current Methods in Medical Image Segmentation", 1. Annual Review of Biomedical Engineering, 2(1): 315-337.

[5] Wirjadi, O., (2007). "Survey of 3-D Image Segmentation Methods", ITWM.

[6] Ma, Z., Tavares, J. M. R., Jorge, R. N., and Mascarenhas, T., (2010). "A Review of Algorithms for Medical Image Segmentation and Their Applications to the Female Pelvic Cavity", Computer Methods in Biomechanics and Biomedical Engineering, 13(2): 235-246.

[7] Heimann, T. and Meinzer, H. P., (2009). "Statistical Shape Models for 3-D Medical Image Segmentation: A Review", Medical Image Analysis, 13(4): 543-563.

[8] Williams, T. G.,Holmes, A. P., Waterton, J. C., Maciewicz, R. A., Hutchinson, C. E., Moots, R. J., and Taylor, C. J., (2010). "Anatomically Corresponded Regional Analysis of Cartilage in Asymptomatic and Osteoarthritic Knees by Statistical Shape Modelling of the Bone", IEEE Transactions on Medical Imaging, 29(8): 1541-1559.

[9] Fripp, J., Crozier, S., Warfield, S. K., and Ourselin, S., (2010). "Automatic Segmentation and Quantitative Analysis of the Articular Cartilages from Magnetic Resonance Images of the Knee", IEEE Transactions on Medical Imaging, 29(1): 55-64.

[10] Shan, L., Zach, C., Charles, C., and Niethammer, M., (2014). "Automatic Atlas-Based Three-Label Cartilage Segmentation from MR Knee Images", Medical Image Analysis, 18(7): 1233-1246.

[11] Wang, Q., Wu, D., Lu, L., Liu, M., Boyer, K. L., and Zhou, S. K., (2014). "Semantic Context Forests for Learning-based Knee Cartilage Segmentation in

3D MR Images", Medical Computer Vision: Large Data in Medical Imaging, 105-115.

[12] Dam, E. B., Lillholm, M., Marques, J., and Nielsen, M., (2015). "Automatic Segmentation of High-and Low-Field Knee MRIs Using Knee Image Quantification with Data from the Osteoarthritis Initiative", Journal of Medical Imaging, 2(2): 024001-024001.

[13] McInerney, T. and Terzopoulos, D., (1996). "Deformable Models in Medical Image Analysis: A Survey", Medical Image Analysis, 1(2): 91–108.

[14] Peng, B., Zhang, L., and Zhang, D., (2013). "A Survey of Graph Theoretical Approaches to Image Segmentation", Pattern Recognition, 46(3): 1020-1038.

[15] Folkesson, J., Dam, E. B., Olsen, O. F., Pettersen, P. C., and Christiansen, C., (2007). "Segmenting Articular Cartilage Automatically Using a Voxel Classification Approach", IEEE Transactions on Medical Imaging, 26(1): 106-115.

[16] Yin, Y., Zhang, X., Williams, R., Wu, X., Anderson, D. D., and Sonka, M., (2010). "LOGISMOS—Layered Optimal Graph Image Segmentation of Multiple Objects and Surfaces: Cartilage Segmentation in the Knee Joint", IEEE Transactions on Medical Imaging, 29(12): 2023-2037.

[17] Zhang, K., Lu, W., and Marziliano, P., (2013). "Automatic Knee Cartilage Segmentation from Multi-contrast MR Images Using Support Vector Machine Classification with Spatial Dependencies", Magnetic Resonance Imaging, 31(10): 1731-1743.

[18] Hani, A. M., Kumar, D., Malik, A., Walter, N., Razak, R., and Kiflie, A., (2013). "Automatic Segmentation of Articular Cartilage from Combined Assessment of Sodium and Proton MR Knee Images", Osteoarthritis and Cartilage, 21: S198-S199.

[19] Heimann, T., Morrison, B. J., Styner, M. A., Niethammer, M., and Warfield, S., (2010). "Segmentation of Knee Images: A Grand Challenge", Proc. MICCAI Workshop on Medical Image Analysis for the Clinic, 207-214.

[20] Lee, J. G., Gumus, S., Moon, C. H., Kwoh, C. K., and Bae, K. T., (2014). "Fully Automated Segmentation of Cartilage from the MR Images of Knee Using a Multi-atlas and Local Structural Analysis Method", Medical Physics, 41(9): 092303.

[21] Vincent, G., Wolstenholme, C., Scott, I., and Bowes, M., (2010). "Fully Automatic Segmentation of the Knee Joint Using Active Appearance Models", Medical Image Analysis for the Clinic: A Grand Challenge, 224-230.

[22] Lee, S., Park, S. H., Shim, H., Yun, I. D., and Lee, S. U., (2011). "Optimization of Local Shape and Appearance Probabilities for Segmentation of Knee Cartilage in 3-D MR Images", Computer Vision and Image Understanding, 115(12): 1710-1720.

[23] Tamez-Pena, J. G., Farber, J., Gonzalez, P. C., Schreyer, E., Schneider, E., and Totterman, S., (2012). "Unsupervised Segmentation and Quantification of

Anatomical Knee Features: Data from the Osteoarthritis Initiative", IEEE Transactions on Biomedical Engineering, 59(4): 1177-1186.

[24] Shan, L., Charles, C., and Niethammer, M., (2012). "Automatic Multi-atlas-based Cartilage Segmentation from knee MR Images", 9th IEEE International Symposium on Biomedical Imaging, 1028-1031.

[25] Shan, L., Charles, C., and Niethammer, M., (2013). "Longitudinal Three-label Segmentation of Knee Cartilage", 10th IEEE International Symposium on Biomedical Imaging, 1376-1379.

[26] Babalola, K. O., Patenaude, B., Aljabar, P., Schnabel, J., Kennedy, D., Crum, W., ..., and Rueckert, D., (2009). "An Evaluation of Four Automatic Methods of Segmenting the Subcortical Structures in the Brain", NeuroImage, 47(4): 1435-1447.

[27] Ryzhkov, M. D., Knee Cartilage Segmentation Algorithms: A Critical Literature Review, http://dspace.library.uu.nl/handle/1874/308831, 1 September 2015.

[28] Hani, A. F. M., Kumar, D., Malik, A. S., Walter, N., Razak, R., and Kiflie, A., (2015). "Multinuclear MR and Multilevel Data Processing: An Insight into Morphologic Assessment of In Vivo Knee Articular Cartilage", Academic Radiology, 22(1): 93-104.

[29] Folkesson, J., Olsen, O. F., Pettersen, P., Dam, E., and Christiansen, C., (2005). "Combining Binary Classifiers for Automatic Cartilage Segmentation in Knee MRI", Computer Vision for Biomedical Image Applications, Berlin, 230-239.

[30] Dam, E. B., and Loog, M., (2008). "Efficient Segmentation by Sparse Pixel Classification", IEEE Transactions on Medical Imaging, 27(10): 1525-1534.

[31] Monga, O., Deriche, R., and Rocchisani, J. M., (1991). "3D Edge Detection Using Recursive Filtering: Application to Scanner Images", CVGIP: Image Understanding, 53(1): 76-87.

[32] Bomans, M., Hohne, K. H., Tiede, U., and Riemer, M., (1990). "3-D Segmentation of MR Images of the Head for 3-D Display", IEEE Transactions on Medical Imaging, 9(2): 177-183.

[33] Pielot, R., Scholz, M., Obermayer, K., Gundelfinger, E. D., and Hess, A., (2001). "3D Edge Detection to Define Landmarks for Point-Based Warping in brain Imaging", IEEE International Conference on In Image Processing, October 2001, 2: 343-346.

[34] Scovanner, P., Ali, S., and Shah, M., (2007). "A 3-Dimensional Sift Descriptor and its Application to Action Recognition", 15th ACM International Conference on Multimedia, September 2007, 357-360.

[35] Marr, D., and Hildreth, E., (1980), "Theory of Edge Detection", Proceedings of the Royal Society of London B: Biological Sciences, 207(1167): 187-217.

[36] Shrivakshan, G. T., and Chandrasekar, C., (2012). "A Comparison of Various Edge Detection Techniques Used in Image Processing". IJCSI International Journal of Computer Science Issues, 9(5): 272-276.

[37] Brejl, M., and Sonka, M., (2000). “Directional 3D Edge Detection in Anisotropic Data: Detector Design and Performance Assessment”, Computer Vision and Image Understanding, 77(2): 84-110.

[38] Lowe, D. G., (2004). “Distinctive Image Features from Scale-Invariant Keypoints”, International Journal of Computer Vision, 60(2): 91-110.

[39] Harris, C., and Stephens, M., (1988). “A Combined Corner and Edge Detector”, Alvey Vision Conference, August 1988, 15: 50.

[40] Moravec, H. P., (1977). “Towards Automatic Visual Obstacle Avoidance”, 5th International Joint Conference on Artificial Intelligence, 1977, Massachusetts Institute of Technology, 584.

[41] Moravec, H. P., (1979). “Visual Mapping by a Robot Rover”, 6th International Joint Conference on Artificial Intelligence, August 1979, 1: 598-600.

[42] Parks, D., and Gravel, J. P., Corner Detection, ftp://v2201206130498606.yourvserver.net/pt/shared/doc/CornerDetection.pdf, 25 July 2016.

[43] Schmid, C., Mohr, R., and Bauckhage, C., (1998). “Comparing and evaluating interest points”, IEEE Sixth International Conference on Computer Vision, January 1998, 230-235.

[44] Laptev, I., and Lindeberg, T., (2005). “On Space-Time Interest Points”, International Journal of Computer Vision, 64(2-3): 107-123.

[45] Sipiran, I., and Bustos, B., (2011). “Harris 3D: A Robust Extension of the Harris Operator for Interest Point Detection on 3D Meshes”, The Visual Computer, 27(11): 963-976.

[46] Yu, T. H., Woodford, O. J., and Cipolla, R., (2013). “A Performance Evaluation of Volumetric 3D Interest Point Detectors”, International Journal of Computer Vision, 102(1-3): 180-197.

[47] Cootes, T. F., Edwards, G. J., and Taylor, C. J., (2001)."Active Appearance Models", IEEE Transactions on Pattern Analysis and Machine Intelligence, 23(6): 681-685.

[48] Mitchell, S. C., Bosch, J. G., Lelieveldt, B. P., Van der Geest, R. J., Reiber, J. H., and Sonka, M., (2002). “3-D Active Appearance Models: Segmentation of Cardiac MR and Ultrasound Images”, IEEE Transactions on Medical Imaging, 21 (9): 1167–1178.

[49] Droual, R., Articulations, http://droualb.faculty.mjc.edu/Lecture%20Notes/Unit%202/chapter 8 articulations%20with%20figures.htm, 29 November 2015.

[50] Health Pages, Knee Joint Anatomy, Function and Problems, http://www.healthpages.org/anatomy-function/knee-joint-structure-function-problems/, 29 November 2015.

[51] Taylor, T., Knee Joint, http://www.innerbody.com/image/skel16.htm, 29 November 2015.

[52] University of Washington Orthopaedics and Sports Medicine, Joints, http://www.orthop.washington.edu/?q=patient-care/articles/arthritis/joints.html, 29 November 2015.

[53] Schmidler, C., (2016). Knee Pain: Symptoms, Causes, and Treatments, http://www.healthpages.org/health-a-z/knee-pain-symptoms-causes-treatment/, 4 April 2016.

[54] Schmidler, C., (2016). Knee Problems and Repairs, http://www.healthpages.org/surgical-care/knee-arthroscopy/, 4 April 2016.

[55] WebMD, Knee Pain Health Center, http://www.webmd.com/pain-management/knee-pain/picture-of-the-knee, 4 April 2016.

[56] Felson, D. T., (2009). "Developments in the Clinical Understanding of Osteoarthritis", Arthritis Research and Therapy, 11(1), 203.

[57] Schmidler, C., (2016). Osteoarthritis in the Knee, February 10, http://www.healthpages.org/health-a-z/osteoarthritis-knee/, 4 April 2016.

[58] Biswal, S., Hastie, T., Andriacchi, T.P., Bergman, G.A., Dillingham, M.F., and Lang, P., (2002). "Risk Factors For Progressive Cartilage Loss in the Knee: A Longitudinal Magnetic Resonance Imaging Study in Forty-Three Patients". Arthritis & Rheumatism, 46(11):2884-2892; Reviewer: Eckstein, F., Cicuttini, F., Raynauld, J. P., Waterton, J. C., and Peterfy, C., (2006). "Magnetic Resonance Imaging (MRI) of Articular Cartilage in Knee Osteoarthritis (OA): Morphological Assessment", Osteoarthritis and Cartilage, 14: 46-75.

[59] Amin, S., LaValley, M.P., Guermazi, A., Grigoryan, M., Hunter, D.J., Clancy, M., …, and Felson, D.T., (2005). "The Relationship Between Cartilage Loss on Magnetic Resonance Imaging and Radiographic Progression in Men and Women with Knee Osteoarthritis", Arthritis & Rheumatism, 52(10): 3152-3159; Reviewer: Eckstein, F., Cicuttini, F., Raynauld, J. P., Waterton, J. C., and Peterfy, C., (2006). "Magnetic Resonance Imaging (MRI) of Articular Cartilage in Knee Osteoarthritis (OA): Morphological Assessment", Osteoarthritis and Cartilage, 14: 46-75.

[60] Başbuğ, E., Osteofit Nedir? Tedavisi Nasıldır?, http://www.rehberim.net/forum/hakkinda-bilgi-nedir-682/854650-osteofit-nedir-tedavisi-nasildir.html, 1 September 2015.

[61] Eckstein, F., Cicuttini, F., Raynauld, J. P., Waterton, J. C., and Peterfy, C., (2006). "Magnetic Resonance Imaging (MRI) of Articular Cartilage in Knee Osteoarthritis (OA): Morphological Assessment", Osteoarthritis and Cartilage, 14: 46-75.

[62] Crema, M. D., Roemer, F. W., Marra, M. D., Burstein, D., Gold, G. E., Eckstein, F., Baum, T., Mosher, T. J., Carrino, J. A., and Guermazi, A. 2011. "Articular Cartilage in the Knee: Current MR Imaging Techniques and Applications in Clinical Practice and Research", Radiographics, 31 (1): 37–61.

[63] Knipe, H. and Pai, V., Kellgren and Lawrence System for Classification of Osteoarthritis of Knee, http://radiopaedia.org/articles/kellgren-and-lawrence-system-for-classification-of-osteoarthritis-of-knee, 1 September 2015.

[64] Wildy, K. S., Zaim, S., Peterfy, C. G., Newman, A. B., Kritchevsky, S., and Nevitt, M. C., (2001). “Reliability of the Whole-Organ Review MRI Scoring (WORMS) Method For Knee Osteoarthritis (OA) in a Multicenter Study”, Arthritis And Rheumatism, 44(9): S155-S155.

[65] Kornaat, P. R., Ceulemans, R. Y., Kroon, H. M., Riyazi, N., Kloppenburg, M., Carter, W. O., ..., and Bloem, J. L., (2005). “MRI Assessment of Knee Osteoarthritis: Knee Osteoarthritis Scoring System (KOSS)—Inter-Observer and Intra-Observer Reproducibility of a Compartment-Based Scoring System”, Skeletal Radiology, 34(2): 95-102.

[66] Lightbox Radiology Education, Introduction to MRI Physics, https://www.youtube.com/watch?v=Ok9ILIYzmaY, 19 March 2015.

[67] Comprehensive Diagnostic Imaging, 3T MRI Scans: How Does a MRI Work?, http://cdiok.com/?page_id=14, 30 March 2015.

[68] Kornaat, P. R., Reeder, S. B., Koo, S., Brittain, J. H., Yu, H., Andriacchi, T.P., and Gold, G.E., (2005). “MR Imaging of Articular Cartilage at 1.5 T and 3.0 T: Comparison of SPGR and SSFP Sequences”, Osteoarthritis Cartilage, 13(4), 338-344.

[69] Eckstein, F., Hudelmaier, M., Wirth, W., Kiefer, B., Jackson, R., Yu. J., …, and Schneider, E., (2006). “Double Echo Steady State (DESS) Magnetic Resonance Imaging of Knee Articular Cartilage At 3 Tesla: A Pilot Study for the Osteoarthritis Initiative”, Annals of the Rheumatic Diseases, 65(4), 433-441.

[70] MRIMaster.com, MRI Cross Sectional Anatomy of Knee, https://mrimaster.com, 21 March 2015.

[71] Cootes, T. F., Taylor, C. J., Cooper, D. H., and Graham, J., (1995). “Active Shape Models- Their Training and Application”, Computer Vision and Image Understanding, 61(1): 38-59.

[72] Heimann, T., Wolf, I., and Meinzer, H.-P., (2006). “Active Shape Models for a Fully Automated 3D Segmentation of the Liver– An Evaluation on Clinical Data”, Medical Image Computing and Computer-Assisted Intervention–MICCAI 2006: 41–48.

[73] Cabezas, M., Oliver, A., Llad´o, X., Freixenet, J., and Cuadra, M. B., (2011). “A Review of Atlas-Based Segmentation for Magnetic Resonance Brain Images”, Computer Methods and Programs in Biomedicine, 104 (3): e158–e177.

[74] Kass, M., Witkin, A., and Terzopoulos, D., (1988)."Snakes: Active Contour Models", International Journal of Computer Vision, 1(4): 321-331.

[75] Osher, S. and Sethian, J. A., (1988). “Fronts Propagating with Curvature-Dependent Speed: Algorithms Based on Hamilton-Jacobi Formulations”, Journal of Computational Physics, 79(1): 12–49.

[76] Baillard, C., Hellier, P., and Barillot, C., (2001). “Segmentation of Brain 3D MR Images Using Level Sets and Dense Registration, Medical Image Analysis, 5(3): 185–194.

[77] Osteoarthritis Initiative (OAI), http://www.oai.ucsf.edu/, 10 August 2014.

[78] Nevitt, M., Felson, D., and Lester, G, (2006). The Osteoarthritis Initiative: protocol for the cohort study, http://oai.epi-ucsf.org/datarelease/docs/StudyDesignProtocol, 14 August 2014.

[79] Lin, D., Statistical Learning Toolbox, (2006), http://www.mathworks.com/matlabcentral/fileexchange/12333-statistical-learning-toolbox, 20 March 2015.

[80] Mount, D. M. and Arya, S., (2010), ANN: A Library for Approximate Nearest Neighbor Searching, http://www.cs.umd.edu/mount/ANN/, 11 March 2015.

[81] Arya, S., Mount, D. M., Netanyahu, N. S., Silverman, R., and Wu, A. Y., (1998). "An Optimal Algorithm for Approximate Nearest Neighbor Searching Fixed Dimensions", Journal of the ACM (JACM), 45 (6): 891–923.

[82] Mount, D. M., (2006), ANN Programming Manual, http://www. cs. umd. edu/~mount/ANN/Files/1.1, 10 August 2015.

[83] Gonzalez, R. C., and Woods, R. E. (2008). Digital Image Processing, Pearson Prentice Hall, Upper Saddle River, NJ.

[84] Aljabar, P., Heckemann, R. A., Hammers, A., Hajnal, J. V., and Rueckert, D., (2009). "Multi-Atlas Based Segmentation of Brain Images: Atlas Selection and its Effect on Accuracy", Neuroimage, 46(3): 726-738.

[85] Maintz, J. A. and Viergever, M. A., (1998). "A Survey of Medical Image Registration", Medical Image Analysis, 2(1): 1-36.

[86] Zitova, B. and Flusser, J., (2003). "Image Registration Methods: A Survey", Image and Vision Computing, 21(11): 977-1000.

[87] Buck, R. J., Wyman, B. T., Graverand, L., Hellio, M. P., Wirth, W., and Eckstein, F., (2010). "An Efficient Subset of Morphological Measures for Articular Cartilage in the Healthy and Diseased Human Knee", Magnetic Resonance in Medicine, 63(3): 680-690.

[88] Kroon, D.-J., (2012), Shape Context Based Corresponding Point Models, https://www.mathworks.com/matlabcentral/fileexchange/30845-shape-context-based-corresponding-point-models, 5 December 2015.

[89] Besl, P. J. and McKay, N. D., (1992). "A method for Registration of 3-D Shapes", IEEE Transactions on Pattern Analysis and Machine Intelligence, 14(2): 239-256.

[90] Zhang, Z., (1994). "Iterative Point Matching for Registration of Free-form Curves and Surfaces", International Journal of Computer Vision, 13(2): 119-152.

[91] Kroon, D.-J., (2012), Active Shape Model (ASM) and Active Appearance Model (AAM), https://www.mathworks.com/matlabcentral/fileexchange/26706-active-shape-model--asm--and-active-appearance-model--aam-?requestedDomain=www.mathworks.com, 12 November 2014.

[92] Smith, L. I., (2002). A Tutorial on Principal Components Analysis, Cornell University, USA.

[93] Acosta, O., Bourgeat, P., Zuluaga, M. A., Fripp, J., Salvado, O., Ourselin, S., and Alzheimer's Disease Neuroimaging Initiative, (2009). "Automated Voxel-Based 3D Cortical Thickness Measurement in a Combined Lagrangian–Eulerian PDE Approach Using Partial Volume Maps", Medical Image Analysis, 13(5): 730-743.

[94] Jones, S. E., Buchbinder, B. R., and Aharon, I., (2000). "Three-Dimensional Mapping of Cortical Thickness Using Laplace's Equation", Human Brain Mapping, 11(1): 12-32.

[95] Yezzi, A. J. and Prince, J. L., (2003). "An Eulerian PDE Approach for Computing Tissue Thickness", IEEE Transactions on Medical Imaging, 22(10): 1332-1339.

[96] Hughes, S. W., D'arcy, T. J., Maxwell, D. J., Saunders, J. E., Ruff, C. F., Chiu, W. S. C., and Sheppard, R. J., (1996). "Application of a New Discrete Form of Gauss' Theorem for Measuring Volume", Physics in Medicine and Biology, 41(9): 1809.

[97] Baldwin, M. A., Langenderfer, J. E., Rullkoetter, P. J., and Laz, P. J., (2010). "Development of Subject-Specific and Statistical Shape Models of the Knee Using an Efficient Segmentation and Mesh-Morphing Approach", Computer Methods and Programs In Biomedicine, 97(3): 232-240.

[98] Williams, T. G., Holmes, A. P., Bowes, M., Vincent, G., Hutchinson, C. E., Waterton, J. C., Maciewicz, R., and Taylor, C. J., (2010). "Measurement and Visualisation of Focal Cartilage Thickness Change by MRI in a Study of Knee Osteoarthritis Using a Novel Image Analysis Tool", The British Journal of Radiology, 83(995): 940-948.

[99] Balamoody, S., Williams, T. G., Waterton, J. C., Bowes, M., Hodgson, R., Taylor, C. J., and Hutchinson, C. E., (2010). "Comparison of 3T MR Scanners in Regional Cartilage-Thickness Analysis in Osteoarthritis: A Cross-Sectional Multicenter, Multivendor Study", Arthritis Research & Therapy, 12(5): 1.

[100] Farag, A. A., (2014). "Biomedical Image Analysis: Statistical and Variational Methods", Cambridge University Press, UK.

[101] Spong, M. W., Hutchinson, S., and Vidyasagar, M., (2006). "Robot Modeling and Control", Volume 3, Wiley, New York.

APPENDIX A

OSTEOARTHRITIS INITIATIVE

The OAI [77] is a public-private partnership comprised of five contracts (N01-AR-2-2258; N01-AR-2-2259; N01-AR-2-2260; N01-AR-2-2261; N01-AR-2-2262) funded by the National Institutes of Health, a branch of the Department of Health and Human Services, and conducted by the OAI Study Investigators. Private funding partners include Merck Research Laboratories; Novartis Pharmaceuticals Corporation, GlaxoSmithKline; and Pfizer, Inc. Private sector funding for the OAI is managed by the Foundation for the National Institutes of Health. This thesis was prepared using an OAI public use data set and does not necessarily reflect the opinions or views of the OAI investigators, the NIH, or the private funding partners.

OAI public use database, which is available at http://www.oai.ucsf.edu/, include 4796 participants in total. Each of these participants is assigned to one of three subcohorts, which are progression subcohort (1390 participants), incidence subcohort (3284 participants), and non-exposed control subcohort (122 participants), by assessing the knee X-ray images for osteophytes and joint space narrowing [78]. Clinical data and medical images have been collected for the participants at baseline visit, and yearly or half-yearly (interim) follow-up visits. Medical images available for the participants are MR images of knee and thigh, and X-ray images of some anatomical regions such as knee, hands, or pelvis.

The MR images of the knee joint have been scanned in coronal, axial, or sagittal imaging planes with various imaging standards including 3-D DESS, T2 MAP, and T1 3-D FLASH. The knee MR image acquisition standards available for the OAI participants are presented in Table A.1 as well as their scan times. The sagittal 3-D DESS image

sequences produced with Siemens Trio 3.0T high-field MR scanners are composed of (384×384x160) voxels, each of which represents a volume of (0.36 x 0.36 x 0.7) mm^3. The coronal and axial 3-D DESS images are not separately scanned but reconstructed using the sagittal 3-D DESS MR images.

Table A.1 The knee MR image sequences and their scan times in minutes.

No	Scan Type	Scan Time (min)		
		Right knee	Left knee	Total
1	Localizer (3-plane)	0.5	0.5	1.0
2	Sagittal 3-D DESS WE	10.6	10.6	21.2
3	Coronal MPR 3-D DESS WE	0.0	0.0	0.0
4	Axial MPR 3-D DESS WE	0.0	0.0	0.0
5	Coronal IW Turbo SE FS 3200 29	3.4	3.4	6.8
6	Sagittal IW Turbo SE FS 3200 30	4.7	4.7	9.4
7	Coronal T1 3-D FLASH WE	8.6	-	8.6
8	Sagittal T2 MAP 120mm field of view	10.6	-	10.6
	Total	38.4	19.2	**57.6**

A.1 Imorphics MR Image Assessments

3-D cartilage and meniscus regions in sagittal 3-D DESS MR images were semi-manually segmented by iMorphics using EndPoint software [98], [99] for the baseline and 12-month follow-up visits of 88 participants in the progression subcohort, and also have kindly been provided for public access[1]. The semi-manual segmentations of cartilage compartments in each MR image were performed by a trained segmenter, who could repeatedly segment these compartments with an intraobserver coefficient of variation of less than 3%, and reviewed by two experts. Because the same segmenter segmented all images of a subject through quality assurance of the segmentations by the experts, the effects of interobserver variation were minimized [98].

The data files that contain 3-D coordinates of the semi-manually segmented femoral cartilage, medial and lateral tibial cartilage, patellar cartilage, and medial and lateral meniscus contours were stored both as a text file format and a MATLAB variable file format. These contours of cartilage compartments have been useful in generating the

[1] These data can be requested by contacting the OAI Coordinating Center with an e-mail to the address of OAIImageHelp@psg.ucsf.edu, and mentioning that the data files of segmented cartilage and meniscus from MR images are interested in.

training models for the cartilage segmentation procedures and validating the automatic segmentation results.

In the studies presented throughout this thesis, the baseline MR images of 33 participants in the OAI data sets assessed by Imorphics were used along with their corresponding data files of semi-manually segmented cartilage. The studies explained in Chapter 4 and Chapter 6 processed all of these 33 MR images whereas the studies explained in Chapter 5 worked on a subset of them. Table A.2 reveals the demographics of 33 participants involved in either the training or testing phases of our studies.

Table A.2 Demographics of the 33 participants involved in the training and testing phases of the studies presented in this thesis.

Criterion	**Train Data (10 MR images)**					**Test Data (23 MR images)**				
Gender	Female			Male		Female			Male	
	5			5		10			13	
Race	Black			White		Black			White	
	3			7		1			22	
Knee	Right			Left		Right			Left	
	4			6		13			10	
Age	40-49	50-59		60-69	70-79	40-49	50-59		60-69	70-79
	5	3		-	2	2	5		7	9
Height (m)	<1.6	[1.6-1.7)		[1.7-1.8)	≥1.8	<1.6	[1.6-1.7)		[1.7-1.8)	≥1.8
	1	6		1	2	4	6		7	6
Weight (kg)	<70	[70-90)		[90-110)	≥110	<70	[70-90)		[90-110)	≥110
	-	5		5	-	4	4		12	3
BMI	<25	[25-30)		[30-35)	≥35	<25	[25-30)		[30-35)	≥35
	-	4		3	3	-	7		12	4
KLG	0	1	2	3	4	0	1	2	3	4
	-	-	2	8	-	-	-	2	21	-

APPENDIX B

MATHEMATICAL FORMULATIONS

B.1 Fundamentals of Quaternions

A quaternion is used to indicate a vector perpendicular to the required plane of rotation in 3-D such as x-z plane or an arbitrary plane. This vector can be the z axis, y axis, or an arbitrary axis. In particular, unit quaternions are useful in representing rotations since they lend themselves directly to the geometrical intuition of axis and angle notation [100]. A quaternion $\boldsymbol{q}$ can be defined as a complex number with three imaginary parts as in (B.1), where $ij = k,\ jk = i,\ ki = j,\ ji = -k,\ kj = -i,\ ik = -j,$ and $i^2 \equiv j^2 \equiv k^2 \equiv -1$. As in equation (B.2), a rotation about a unit vector $\boldsymbol{v} = [v_x + v_y + v_z]^T$ by θ is represented by a unit quaternion $\boldsymbol{q}$ [101].

$$\boldsymbol{q} = [q_0 + iq_x + jq_y + kq_z]^T \tag{B.1}$$

$$\boldsymbol{q} = [\cos\frac{\theta}{2} + v_x \sin\frac{\theta}{2} + v_y \sin\frac{\theta}{2} + v_z \sin\frac{\theta}{2}]^T \tag{B.2}$$

Product of two arbitrary quaternions $\boldsymbol{r}$ and $\boldsymbol{q}$ is performed according to (B.3) using the complex representations of the quaternions, or (B.4) using an orthogonal 4x4 matrix representation $\boldsymbol{R}$ of $\boldsymbol{r}$ and the vector representation of $\boldsymbol{q}$. To practically find the product of $\boldsymbol{qr}$, 3x3 lower left portion of $\boldsymbol{R}$ is transposed to obtain $\bar{\boldsymbol{R}}$, and $\bar{\boldsymbol{R}}\boldsymbol{q}$ multiplication is calculated.

$$\begin{aligned}\boldsymbol{rq} = &\left(r_0 q_0 - r_x q_x - r_y q_y - r_z q_z\right) + i\left(r_0 q_x + r_x q_0 + r_y q_z - r_z q_y\right) \\ &+ \mathrm{j}\left(r_0 q_y - r_x q_z + r_y q_0 + r_z q_x\right) \\ &+ \mathrm{k}\left(r_0 q_z + r_x q_y - r_y q_x + r_z q_0\right)\end{aligned} \tag{B.3}$$

$$\boldsymbol{rq} = \boldsymbol{Rq} = \begin{bmatrix} r_0 & -r_x & -r_y & -r_z \\ r_x & r_0 & -r_z & r_y \\ r_y & r_z & r_0 & -r_x \\ r_z & -r_y & r_x & r_0 \end{bmatrix} \boldsymbol{q} \tag{B.4}$$

Dot product of two quaternions is computed as in (B.5), and preserved so that $(\boldsymbol{q}.\boldsymbol{u})(\boldsymbol{q}.\boldsymbol{r}) = (\boldsymbol{q}.\boldsymbol{q})(\boldsymbol{u}.\boldsymbol{r})$. Dot product of a unit quaternion $\boldsymbol{q}$ is given by (B.6). The corollary that magnitude of a dot product is the product of magnitudes is formulated in (B.7).

$$\boldsymbol{r}.\boldsymbol{q} = r_0 q_0 + r_x q_x + r_y q_y + r_z q_z \tag{B.5}$$

$$\boldsymbol{q}.\boldsymbol{q} = \|\boldsymbol{q}\|^2 = 1 \tag{B.6}$$

$$(\boldsymbol{q}.\boldsymbol{r})(\boldsymbol{q}.\boldsymbol{r}) = (\boldsymbol{q}.\boldsymbol{q})(\boldsymbol{r}.\boldsymbol{r}) \tag{B.7}$$

Conjugate of an arbitrary quaternion **q** is denoted by $\boldsymbol{q}^* = q_0 - iq_x - jq_y - kq_z$. Inverse of a non-zero quaternion $\boldsymbol{q}$ can be obtained as in (B.8). $\boldsymbol{q}^*$ is associated with $\boldsymbol{Q}^T$. Since $\boldsymbol{Q}$ is orthogonal, it holds that $\boldsymbol{Q}\boldsymbol{Q}^T = \boldsymbol{Q}^T\boldsymbol{Q} = (\boldsymbol{q}.\boldsymbol{q})\boldsymbol{I}$. This formulation yields that $\boldsymbol{q}^*.\boldsymbol{q} = \boldsymbol{q}.\boldsymbol{q}$ considering (B.8) and the fact that $\boldsymbol{Q}^T = \boldsymbol{Q}^{-1}$ for orthogonal matrices. If $\boldsymbol{q}$ is a unit quaternion $\boldsymbol{q}^{-1} = \boldsymbol{q}^*$.

$$\boldsymbol{q}^{-1} = \frac{\boldsymbol{q}^*}{\boldsymbol{q}.\boldsymbol{q}} \tag{B.8}$$

An arbitrary vector can be represented as a quaternion with no real part. If $\boldsymbol{v} = [v_x, v_y, v_z]^T$, then the quaternion $\boldsymbol{v} = 0 + iv_x + jv_y + kv_z$. Because no real part is associated, the matrix $\boldsymbol{V}$ of quaternion $\boldsymbol{v}$ is skew symmetric so that $\boldsymbol{V}^T = -\boldsymbol{V}$ and $\overline{\boldsymbol{V}}^T = -\overline{\boldsymbol{V}}$. Then, rotation of pure imaginary quaternion $\boldsymbol{v}$, which represents either a 3-D point or vector, by a unit quaternion $\boldsymbol{q}$ is achieved by the composite product in (B.9), where $\boldsymbol{v}'$ is the rotated pure imaginary quaternion.

$$\boldsymbol{v}' = \boldsymbol{q}\boldsymbol{v}\boldsymbol{q}^{*} \tag{B.9}$$

B.2 Iterative Closest Point Algorithm

Given a reference shape and a target shape denoted by the point sets of $\boldsymbol{P}_r$ and $\boldsymbol{P}_t$, respectively, iterative closest point algorithm iteratively estimates the optimal translation, scaling, and rotation to align $\boldsymbol{P}_t$ to $\boldsymbol{P}_r$ by minimizing the Euclidean distance between the two shapes. The following subsections explain how the point correspondences between $\boldsymbol{P}_t$ and $\boldsymbol{P}_r$ are found, and the parameters of alignment are estimated in this algorithm.

B.2.1 Finding Point Correspondences

Closest point correspondence is assumed to determine the point correspondences. However, convergence is usually possible with this assumption if coordinates of reference shape points are close enough to the coordinates of target shape points. For every point $\boldsymbol{p}_t^j$ in $\boldsymbol{P}_t$ the closest point $\boldsymbol{p}_r^k$ in $\boldsymbol{P}_r$ is determined according to (B.10). These closest points among the reference shape points $\boldsymbol{p}_r^k$ are denoted by $\boldsymbol{p}_y^j$ as the correspondents of $\boldsymbol{p}_t^j$, where $j = 1,2,\dots,N_t$, and N_t is the number of points in $\boldsymbol{P}_t$. The set of correspondent points $\boldsymbol{p}_y^j$ is represented by $\boldsymbol{P}_y$.

$$\underset{k}{\boldsymbol{argmin}} \left\| \boldsymbol{p}_t^j - \boldsymbol{p}_r^k \right\| \tag{B.10}$$

When the set of correspondent points $(\boldsymbol{P}_t, \boldsymbol{P}_y)$ is established, the optimal parameters of translation $\boldsymbol{t}$, scale $\boldsymbol{s}$, and rotation $\boldsymbol{R}$ are estimated such that $\boldsymbol{P}_y = s\boldsymbol{R}(\boldsymbol{P}_t) + \boldsymbol{t}$ is satisfied with a minimal residual error that can be computed as in (B.11).

$$\boldsymbol{E} = \sum_{j=1}^{N_t} \left\| \boldsymbol{e}_j \right\|^2 = \sum_{j=1}^{N_t} \left\| \boldsymbol{p}_y^j - s\boldsymbol{R}\left(\boldsymbol{p}_t^j\right) - \boldsymbol{t} \right\|^2 \tag{B.11}$$

B.2.2 Translation Estimation

Centred zero-mean points are computed for all points in $\boldsymbol{P}_t$ according to (B.12), where $\boldsymbol{\mu}_t$ is computed as in (6.1). The same centring step is also performed for the point set $\boldsymbol{P}_y$. Then, the total error equation can be rearranged as in (B.13), where $\boldsymbol{t}'$ is defined according to (B.14).

$$\boldsymbol{p'}_t^j = \boldsymbol{p}_t^j - \boldsymbol{\mu}_t \tag{B.12}$$

$$\begin{aligned}\boldsymbol{E} &= \sum_{j=1}^{N_t} \left\| \boldsymbol{p'}_y^j - s\boldsymbol{R}\left(\boldsymbol{p'}_t^j\right) - \boldsymbol{t'} \right\|^2 \\ &= \sum_{j=1}^{N_t} \left[\left\| \boldsymbol{p'}_y^j - s\boldsymbol{R}\left(\boldsymbol{p'}_t^j\right) \right\|^2 - 2\boldsymbol{t'} \left\| \boldsymbol{p'}_y^j - s\boldsymbol{R}\left(\boldsymbol{p'}_t^j\right) \right\| + \|\boldsymbol{t'}\|^2 \right] \\ &= \sum_{j=1}^{N_t} \left\| \boldsymbol{p'}_y^j - s\boldsymbol{R}\left(\boldsymbol{p'}_t^j\right) \right\|^2 - 2\boldsymbol{t'} \sum_{j=1}^{N_t} \left\| \boldsymbol{p'}_y^j - s\boldsymbol{R}\left(\boldsymbol{p'}_t^j\right) \right\| + N_t \|\boldsymbol{t'}\|^2\end{aligned} \tag{B.13}$$

The term in the middle of the final expansion in (B.13) is accepted as zero, since the point sets are centred to be zero-mean, and scaling or rotation do not affect the mean. The first term does not depend on $\boldsymbol{t'}$, but the third term is useful to estimate translation. Because the third term cannot be negative, $\boldsymbol{t'}$ should be 0 to minimize the total error. Then, the optimal translation is derived as in (B.14).

$$\begin{aligned}\boldsymbol{t'} = \boldsymbol{t} - \boldsymbol{\mu}_y + s\boldsymbol{R}(\boldsymbol{\mu}_t) = 0 \\ \Rightarrow \boldsymbol{t} = \boldsymbol{\mu}_y - s\boldsymbol{R}(\boldsymbol{\mu}_t)\end{aligned} \tag{B.14}$$

B.2.3 Scale Estimation

With removal of the second and third terms of the total error equation in (B.13), only the first term remains. This term is further expanded in (B.15). Because rotation preserves the length of the points, the expression of $\left\|\boldsymbol{R}\left(\boldsymbol{p'}_t^j\right)\right\|$ can be replaced with $\left\|\boldsymbol{p'}_t^j\right\|$. Accordingly, the terms denoted by $\boldsymbol{S_y}$ and $\boldsymbol{S_p}$ are the sums of the squared lengths of the centred points in $\boldsymbol{P}_y$ and $\boldsymbol{P}_t$, whereas the term represented by $\boldsymbol{D}$ is the sum of the dot products of the rotated target shape points in $\boldsymbol{P}_t$ with their corresponding reference shape points in $\boldsymbol{P}_y$.

$$\begin{aligned}\boldsymbol{E} &= \sum_{j=1}^{N_t} \left\| p'^j_y - sR\left(p'^j_t\right) \right\|^2 \\ &= \sum_{j=1}^{N_t} \left\| \boldsymbol{p'}_y^j \right\|^2 - 2s \sum_{j=1}^{N_t} \boldsymbol{p'}_y^j \boldsymbol{R}\left(\boldsymbol{p'}_t^j\right) + s^2 \sum_{j=1}^{N_t} \left\| \boldsymbol{R}\left(\boldsymbol{p'}_t^j\right) \right\|^2\end{aligned} \tag{B.15}$$

$$= \underbrace{\sum_{j=1}^{N_t} \left\| \boldsymbol{p'}_y^{\,j} \right\|^2}_{\boldsymbol{S_y}} - 2s \underbrace{\sum_{j=1}^{N_t} \boldsymbol{p'}_y^{\,j} \boldsymbol{R}\left(\boldsymbol{p'}_t^{\,j}\right)}_{\boldsymbol{D}} + s^2 \underbrace{\sum_{j=1}^{N_t} \left\| \boldsymbol{p'}_t^{\,j} \right\|^2}_{\boldsymbol{S_p}}$$

Then, the total error can be rewritten as in (B.16) such that only the first term depends on s. Similarly, with the first term equalized to zero to minimize $\boldsymbol{E}$, the estimate of optimal scale is found according to (B.17).

$$\begin{aligned} \boldsymbol{E} &= \boldsymbol{S_y} - 2s\,\boldsymbol{D} + s^2 \boldsymbol{S_p} \\ &= \left(s\sqrt{\boldsymbol{S_p}} - \frac{\boldsymbol{D}}{\sqrt{\boldsymbol{S_p}}} \right)^2 + \frac{\boldsymbol{S_y S_p} - \boldsymbol{D^2}}{\boldsymbol{S_p}} \end{aligned} \tag{B.16}$$

$$\begin{aligned} &\left(s\sqrt{\boldsymbol{S_p}} - \frac{\boldsymbol{D}}{\sqrt{\boldsymbol{S_p}}} \right)^2 = 0 \\ &\Rightarrow s = \frac{\boldsymbol{D}}{\boldsymbol{S_p}} = \frac{\sum_{j=1}^{N_t} \boldsymbol{p'}_y^{\,j} \boldsymbol{R}\left(\boldsymbol{p'}_t^{\,j}\right)}{\sum_{j=1}^{N_t} \left\| \boldsymbol{p'}_t^{\,j} \right\|^2} \end{aligned} \tag{B.17}$$

B.2.4 Rotation Estimation

To minimize $\boldsymbol{E}$ with respect to the remaining second term that includes rotation $\boldsymbol{R}$ in (B.15), this term is set to zero too. $\boldsymbol{S_y}$, $\boldsymbol{S_p}$, and $\boldsymbol{S_y S_p}$ are greater than or equal to zero, and do not depend on $\boldsymbol{R}$. $\boldsymbol{D^2}$ is also greater than or equal to zero, but depends on $\boldsymbol{R}$. Therefore, the nominator of the term $\boldsymbol{S_y S_p} - \boldsymbol{D^2}$ is minimized by maximizing $\boldsymbol{D}$. Maximization of $\boldsymbol{D}$ can be geometrically interpreted as in (B.18), where θ is the angle between the reference shape points and rotated target shape points. The point sets are aligned so that θ gets 0 for an optimal rotation. When θ is 0, $\cos\theta$ is 1 and the maximum value of the expression $\boldsymbol{D}$ is obtained. Therefore, angle θ should be minimized to maximize $\boldsymbol{D}$**.** If optimal rotation $\boldsymbol{R}$ is represented by the unit quaternion $\boldsymbol{q}$, $\boldsymbol{D}$ can be rearranged as in (B.19) based on (B.9) and (B.8).

$$\boldsymbol{D} = \sum_{j=1}^{N_t} \left\| \boldsymbol{p'}_y^{\,j} \right\| \left\| \boldsymbol{R}\left(\boldsymbol{p'}_t^{\,j}\right) \right\| \cos\theta \tag{B.18}$$

$$\boldsymbol{D} = \sum_{j=1}^{N_t} \boldsymbol{p'}_y^{\,j} \left(\boldsymbol{q} \boldsymbol{p'}_t^{\,j} \boldsymbol{q}^* \right) = \sum_{j=1}^{N_t} \left(\boldsymbol{q} \boldsymbol{p'}_t^{\,j} \boldsymbol{q}^* \right) \boldsymbol{p'}_y^{\,j} = \sum_{j=1}^{N_t} \left(\boldsymbol{q} \boldsymbol{p'}_t^{\,j} \right) \left(\boldsymbol{p'}_y^{\,j} \boldsymbol{q} \right) \tag{B.19}$$

The multiplications of $\boldsymbol{q}\boldsymbol{p'}_t^j$ and $\boldsymbol{p'}_y^j\boldsymbol{q}$ can be realized with skew-symmetric matrices of $\overline{\boldsymbol{P'}}_t^j$ and $\boldsymbol{P'}_y^j$, which are based on pure imaginary quaternions $\boldsymbol{p'}_t^j$and $\boldsymbol{p'}_y^j$, respectively. According to the rule of skew-symmetric matrices mentioned in Subsection B.1, the equation of $\boldsymbol{D}$ is reformulated as in (B.20) to obtain a compact form of known and unknown variables. The matrix $\boldsymbol{M}$ in (B.20) can be defined as in (B.21), where $\boldsymbol{S}_{xx} = \sum_{j=1}^{N_t} p'^{j_x}_t p'^{j_x}_y$, $\boldsymbol{S}_{xy} = \sum_{j=1}^{N_t} p'^{j_x}_t p'^{j_y}_y$, etc.

$$\begin{aligned}\boldsymbol{D} &= \sum_{j=1}^{N_t}\left(\overline{\boldsymbol{P'}}_t^j\boldsymbol{q}\right)\left(\boldsymbol{P'}_y^j\boldsymbol{q}\right) = \sum_{j=1}^{N_t}\left(\overline{\boldsymbol{P'}}_t^j\boldsymbol{q}\right)^{\boldsymbol{T}}\left(\boldsymbol{P'}_y^j\boldsymbol{q}\right)\\ &= \boldsymbol{q}^{\boldsymbol{T}}\underbrace{\left(\sum_{\boldsymbol{j=1}}^{\boldsymbol{N_t}}\underbrace{\overline{\boldsymbol{P'}}_{\boldsymbol{t}}^{\boldsymbol{j}\boldsymbol{T}}\boldsymbol{P'}_{\boldsymbol{y}}^{\boldsymbol{j}}}_{\boldsymbol{M_j}}\right)}_{\boldsymbol{M}}\boldsymbol{q} = \boldsymbol{q}^{\boldsymbol{T}}\boldsymbol{M}\boldsymbol{q}\end{aligned} \tag{B.20}$$

$$\boldsymbol{M} = \begin{bmatrix} \boldsymbol{S}_{xx}+\boldsymbol{S}_{yy}+\boldsymbol{S}_{zz} & \boldsymbol{S}_{yz}-\boldsymbol{S}_{zy} & \boldsymbol{S}_{zx}-\boldsymbol{S}_{xz} & \boldsymbol{S}_{xy}-\boldsymbol{S}_{yx} \\ \boldsymbol{S}_{yz}-\boldsymbol{S}_{zy} & \boldsymbol{S}_{xx}-\boldsymbol{S}_{yy}-\boldsymbol{S}_{zz} & \boldsymbol{S}_{xy}+\boldsymbol{S}_{yx} & \boldsymbol{S}_{xz}+\boldsymbol{S}_{zx} \\ \boldsymbol{S}_{zx}-\boldsymbol{S}_{xz} & \boldsymbol{S}_{yx}+\boldsymbol{S}_{xy} & \boldsymbol{S}_{yy}-\boldsymbol{S}_{xx}-\boldsymbol{S}_{zz} & \boldsymbol{S}_{yz}+\boldsymbol{S}_{zy} \\ \boldsymbol{S}_{xy}-\boldsymbol{S}_{yx} & \boldsymbol{S}_{zx}+\boldsymbol{S}_{xz} & \boldsymbol{S}_{zy}+\boldsymbol{S}_{yz} & \boldsymbol{S}_{zz}-\boldsymbol{S}_{xx}-\boldsymbol{S}_{yy} \end{bmatrix} \tag{B.21}$$

A quaternion that maximizes $\boldsymbol{q}^{\boldsymbol{T}}\boldsymbol{M}\boldsymbol{q}$ is the eigenvector that corresponds to the most positive eigenvalue of the matrix $\boldsymbol{M}$. Then, optimal rotation $\boldsymbol{R}$ is determined as $3x3$ lower left corner of the matrix given in (B.22), which can be alternatively computed as in (B.23).

$$\begin{aligned}\boldsymbol{R} &\rightarrow \overline{\boldsymbol{Q}}^{\boldsymbol{T}}\boldsymbol{Q}\\ &= \left[\begin{array}{c|ccc} q_0^2+q_x^2+q_y^2+q_z^2 & 0 & 0 & 0 \\ \hline 0 & q_0^2+q_x^2-q_y^2-q_z^2 & 2q_xq_y-2q_0q_z & 2q_xq_z+2q_0q_y \\ 0 & 2q_0q_z+2q_xq_y & q_0^2-q_x^2+q_y^2-q_z^2 & 2q_yq_z-2q_0q_x \\ 0 & 2q_xq_z+2q_0q_y & 2q_yq_z+2q_0q_x & q_0^2-q_x^2-q_y^2+q_z^2 \end{array}\right]\end{aligned} \tag{B.22}$$

$$\boldsymbol{R} = \begin{bmatrix} q_x \\ q_y \\ q_z \end{bmatrix}\begin{bmatrix} q_x & q_y & q_z \end{bmatrix} + \begin{bmatrix} q_0 & -q_z & q_y \\ q_z & q_0 & -q_x \\ -q_y & q_x & q_0 \end{bmatrix}\begin{bmatrix} q_0 & -q_z & q_y \\ q_z & q_0 & -q_x \\ -q_y & q_x & q_0 \end{bmatrix} \tag{B.23}$$

CURRICULUM VITAE

PERSONAL INFORMATION

Name Surname : Ceyda Nur ÖZTÜRK

Date of Birth and Place : 17.11.1987, BURSA

Foreign Languages : English

E-mail : ceyda.nur.ozturk@std.yildiz.edu.tr

EDUCATION

Degree	Department	School/University	Date of Graduation
Master of Science	Computer Engineering	Fatih University	2012
Bachelor of Science	Computer Engineering.	Fatih University	2010
High School	Quantitative	Open High School	2004

PUBLISHMENTS

Papers

1. Öztürk, C. N., and Albayrak, S., (2016). “Automatic Segmentation of Cartilage in High-Field Magnetic Resonance Images of the Knee Joint With an Improved Voxel-Classification-Driven Region-Growing Algorithm Using Vicinity-Correlated Subsampling”, Computers in Biology and Medicine, 72: 90-107.

2. Altuntaş, N., İmal, E., Emanet, N., and Öztürk, C.N., (2016). "Reinforcement Learning Based Mobile Robot Navigation", Turkish Journal Of Electrical Engineering & Computer Sciences, 24: 1747-1767.

Conference Papers

1. Orhan, Z., Öztürk, C. N., and Altuntaş, N., (2008). "SınavYazar: A Tool for Generating Automatic Exams and Solutions for Primary Education", Electric-Electronic-Computer Engineering Symposium, November 2008, Bursa.

2. Altuntaş, N., İmal, E., Emanet, N., and Öztürk, C.N., (2013). "Reinforcement Learning Based Mobile Robot Navigation", 3rd International Symposium on Computing and Science in Engineering, October 2013, Aydın, 284-289.

3. Öztürk, C. N., and Bilgin, G., (2015). “A Comparative Study on Manifold Learning of Hyperspectral Data for Land Cover Classification”, SPIE 6th International Conference on Graphic and Image Processing, March 2014, Beijing, 94431L-94431L.

4. Öztürk, C. N., and Albayrak, S., (2015). “Edge Detection on MR Images with Marr-Hildreth Method Extended to Third Dimension”, IEEE 23th Signal Processing and Communications Applications Conference, 16-19 May 2015, Malatya, 763-766.

5. Öztürk, C. N., and Albayrak, S., (2015). “Efficient Cartilage Segmentation in High-Field Knee MR Images with Voxel-Classification-Driven Region-Growing Algorithm”, IEEE 19th National Biomedical Engineering Meeting, 5-6 November 2015, Istanbul, 1-4.

Projects

1. Mobile Robot Navigation with Monocular SLAM, Fatih University Scientific Research Project, P50061202_B, 20,000, April 2012-April 2013.